

UNCLASSIFIED

AD 410242

DEFENSE DOCUMENTATION CENTER

FOR

SCIENTIFIC AND TECHNICAL INFORMATION

CAMERON STATION, ALEXANDRIA, VIRGINIA



UNCLASSIFIED

NOTICE: When government or other drawings, specifications or other data are used for any purpose other than in connection with a definitely related government procurement operation, the U. S. Government thereby incurs no responsibility, nor any obligation whatsoever; and the fact that the Government may have formulated, furnished, or in any way supplied the said drawings, specifications, or other data is not to be regarded by implication or otherwise as in any manner licensing the holder or any other person or corporation, or conveying any rights or permission to manufacture, use or sell any patented invention that may in any way be related thereto.

N-63-4-3

CATALOGED BY DDC

AS AD No. 410242

RADC-TDR-63-152

STUDY OF FAILURE MECHANISMS
AT SURFACES AND INTERFACES

FINAL REPORT

TECHNICAL DOCUMENTARY REPORT NO. RADC-TDR-63-152

MARCH 1963

ROME AIR DEVELOPMENT CENTER
RESEARCH AND TECHNOLOGY DIVISION
AIR FORCE SYSTEMS COMMAND
UNITED STATES AIR FORCE
GRIFFISS AIR FORCE BASE

NEW YORK

PROJECT NO. 5519, TASK NO. 551906

410242

(Prepared under Contract No. AF 30(602)-2593 by
Motorola Inc., Solid State Systems Division, Phoenix, Arizona)

NOTICES

Qualified requesters may obtain copies from ASTIA. Orders will be expedited if placed through the librarian or other person designated to request documents from ASTIA. All others should apply to the U. S. Department of Commerce, Office of Technical Services, Washington 25, D. C.

When US Government drawings, specifications, or other data are used for any purpose other than a definitely related government procurement operation, the government thereby incurs no responsibility nor any obligation whatsoever; and the fact that the government may have formulated, furnished, or in any way supplied the said drawings, specifications, or other data is not to be regarded by implication or otherwise, as in any manner licensing the holder or any other person or corporation, or conveying any rights or permission to manufacture, use, or sell any patented invention that may in any way be related thereto.

Do not return this copy. Retain or destroy.

RADC-TDR-63-152

**STUDY OF FAILURE MECHANISMS
AT SURFACES AND INTERFACES**

FINAL REPORT

TECHNICAL DOCUMENTARY REPORT NO. RADC-TDR-63-152

MARCH 1963

**ROME AIR DEVELOPMENT CENTER
RESEARCH AND TECHNOLOGY DIVISION
AIR FORCE SYSTEMS COMMAND
UNITED STATES AIR FORCE
GRIFFISS AIR FORCE BASE**

NEW YORK

PROJECT NO. 5519, TASK NO. 551906

**Prepared by: Dr. Kenneth Greenough
Frank Reed
Neva Johnson**

**(Prepared under Contract No. AF 30(602)-2593 by
Motorola Inc., Solid State Systems Division, Phoenix, Arizona)**

FOREWORD

Acknowledgement is made of the assistance of Frank Reed in preparing the section on the metal-dielectric interface and of Neva Johnson in preparing the section on radioactive diffusion studies. Acknowledgement is also made of the technical contributions of David Glenn (optical microscopy), Perry Merrill (electrical measurements), David Peterson (preparation and evaluation of glass dielectrics), Charles Russell (preparation and strain measurements of silicon monoxide dielectrics), Robert Mattox (preparation and evaluation of tin oxide resistors), Lewis Derting (electrical measurements), Jacqueline Moss (mathematical analysis), Michael Lowenstein (infrared analysis), and Dr. John McNamara of the Semiconductor Products Division for assistance in radioactive diffusion measurements.

PUBLICATION REVIEW

This report has been reviewed and is approved.

Approved: *David F. Barber*
DAVID F. BARBER
Chief, Applied Research Laboratory
Directorate of Engineering

Approved: *William F. Betheke*
WILLIAM F. BETHEKE
Director of Engineering

FOR THE COMMANDER:

Irving J. Gabelman
IRVING J. GABELMAN
Director of Advanced Studies

ABSTRACT

The investigation of the interface between a metal film and a thin-film dielectric, e.g., tantalum-tantalum oxide, aluminum-aluminosilicate glass, incorporated in thin-film capacitors has been most successful in providing the fundamental information necessary to identify and quantitatively define the characteristic failure mechanisms at these interfaces. The frequency dispersion of capacitance and dissipation factor for the tantalum-tantalum oxide system fits a curve predicted by a mathematical model of the interface based on an exponentially varying resistivity across the interface. The slopes of the capacitance and dissipation factor versus frequency curves which exhibit an inverse relationship to dielectric thickness and changes in the shapes of these curves brought about by thermal and humidity stressing, can also be correlated with the interface model involving a variation in resistivity with position relative to the interface.

Preliminary investigations of the characteristics of leakage current versus applied voltage curves for various metal-glass dielectric interfaces indicate that the observed trap-limited, space-charge limited currents are a function of the nature of the metal electrode interface and applied thermal stress. The applied voltage-leakage current studies will be valuable in evaluating failure mechanisms originating at the metal-dielectric interface.

Radioactive diffusion studies have revealed that irreversible changes in stoichiometry occur across the interface of thermally, thermal-electrically stressed, tantalum-tantalum oxide interfaces. No correlation between changes in electrical properties and the observed irreversible diffusion of tantalum across the stressed interface, have been made to date because of insufficient data. However, the utility of radioactive isotopes analysis for studying diffusion enhanced failure mechanisms at interfaces has been demonstrated.

Selective beveling and etching techniques for revealing interfacial properties have been developed and their feasibility has been demonstrated in the evaluation of the tantalum-tantalum oxide interfaces.

Results of the investigations on the various semiconducting tin oxide film-substrate model systems have been revealing in terms of the qualitative nature of possible failure modes associated with the nature of the substrate interface. Observations of changes in the basic conduction mechanism as a function of applied thermal and electrical stress are accomplished by measurement of changes in the Hall mobility and its temperature dependence, and the Hall constant. Stressed-induced changes in the conduction mechanism of the electronically degenerate film are qualitatively described in terms of high resistivity crystallite grain boundary regions of the polycrystalline film.

TABLE OF CONTENTS

<u>Section</u>	<u>Page</u>
1. INTRODUCTION	1-1
2. CONCLUSIONS	2-1
3. RECOMMENDATIONS	3-1
4. DISCUSSION	4-1
4.1 Metal Electrode-Dielectric Interface	4-1
4.1.1 Summary of Past Work	4-1
4.1.2 Electrical Measurements	4-2
4.2 Diffusion Studies on the Tantalum-Tantalum Oxide System	4-32
4.2.1 Background	4-32
4.2.2 Experimental Procedure	4-32
4.2.3 Mathematical Treatment of Data	4-34
4.2.4 Interpretation of Data	4-38
4.2.5 Conclusion	4-49
4.3 Optical Microscopy - Tantalum-Tantalum Oxide Interface	4-50
4.3.1 Experimental Technique	4-50
4.3.2 Tantalum-Tantalum Oxide Interface Determination	4-50
4.4 Tin Oxide - Substrate Interface Model System	4-52
4.4.1 Summary of Efforts to Date	4-52
4.4.2 Experimental Work in Fourth Quarter	4-54
4.5 Conclusions	4-85
4.6 Other Effort	4-86
LIST OF REFERENCES	4-87

LIST OF TABLES

<u>Table</u>	<u>Page</u>
I. Curve Fit Coefficients for Thin-Film Tantalum Capacitors	4-13
II. Typical Characteristics of Silicon Monoxide Thin-Film Capacitors	4-18
III. Typical Characteristics of Silicon Dioxide Thin-Film Capacitors	4-20
IV. Radioactive Tantalum-Tantalum Oxide Units, Stress Conditions	4-33
V. Radioactive Tantalum-Tantalum Oxide Units Capacitance and Dissipation Factor Measurements	4-38
VI. Concentration of Tantalum in the Constant Region of the Activity of Profile of Tantalum Oxide. Distance from Tantalum-Tantalum Oxide Interface to Region of Constant Tantalum Concentration	4-43
VII. Diffusion Constants for Stressed and Unstressed Tantalum-Tantalum Oxide Units	4-49
VIII. Substrate Properties	4-54
IX. Tabulated Data Group 15 Thermal-Electrical Stress	4-55
X. Tabulated Data Group 16 Thermal Stress	4-56
XI. Tabulated Data-Charge Carrier Concentration: Group 15	4-57
XII. Tabulated Data-Charge Carrier Concentration, Group 16	4-58

LIST OF ILLUSTRATIONS

<u>Figure</u>		<u>Page</u>
1.	Capacitance versus Frequency for Thin Film Tantalum Capacitors . . .	4-6
2.	Dissipation Factors versus Frequency for Thin Film Tantalum Capacitors	4-7
3.	Reciprocal Capacitance Variation ($C_{1\text{kc}}/D-1$) versus Frequency for Thin Film Tantalum Capacitance	4-8
4.	Model of Dielectric-Metal System, its Equivalent Circuit, and Plot of Resistivity versus Position	4-10
5.	Normalized Capacitance versus Frequency for a Thin Film Tantalum Capacitor. The Various Curves are from Measurements taken at Room Temperature Following the Indicated Environments	4-11
6.	Dissipation Factor versus Frequency for a Thin Film Tantalum Capacitor. These Curves Correspond to the Capacitance Curve in Figure 4.	4-12
7.	Reciprocal Capacitance Variation ($C_{\text{init. } 1\text{kc}}/C-1$) versus Temperature and Frequency for a Thin Film Capacitor Anodized to 25 volts. (Note vertical coordinate reversal.)	4-14
8.	Reciprocal Capacitance Variation versus Temperature and Frequency for a Thin Film Tantalum Capacitor Anodized to 100 volts. (Note vertical coordinate reversal)	4-15
9.	$C/C_{1\text{kc}}$, D.F. vs Frequency for SiO_2 Test Units with Al, Cr, Cu, Au, Ag Electrodes	4-17
10.	$C/C_{1\text{kc}}$ vs Frequency for Stressed SiO_2 Test Units	4-19
11.	$C/C_{1\text{kc}}$ and DF vs Frequency for $\text{Al}_2\text{O}_3 \cdot \text{SiO}_2$ Test Units	4-22
12.	C and DF vs Frequency of Improved $\text{Al}_2\text{O}_3 \cdot \text{SiO}_2$ Test Units	4-24
13.	Temperature Coefficient of Capacitance and Dissipation Factor vs Frequency for Improved $\text{SiO}_2 \cdot \text{Al}_2\text{O}_3$ Test Units	4-25
14.	Temperature Coefficient of Capacitance vs Film Thickness for Improved $\text{Al}_2\text{O}_3 \cdot \text{SiO}_2$ Test Unit	4-26
15.	Gold Electroded Aluminosilicate Test Unit	4-27
16.	Aluminum Electroded Aluminosilicate Test Unit	4-28
17.	Aluminum Electroded Aluminosilicate Test Unit	4-29
18.	Aluminum Electroded Aluminosilicate Test Unit	4-30
19.	Etch Rate of Tantalum Oxide Film (Sample No. 10)	4-36
20.	Etch Rate of Tantalum Oxide Film (Sample No. 5)	4-37
21.	Activity Profile of Radioactive Tantalum Oxide Test Unit	4-39
22.	Concentration Profile of Radioactive Tantalum-Tantalum Oxide Test Unit	4-40
23.	Photomicrograph of Radioactive Tantalum Oxide Film	4-41
24.	Concentration Profiles of Radioactive Tantalum-Tantalum Oxide Test Units.	4-42
25.	Schematic Diagram of Tantalum Concentration in Radioactive Tantalum-Tantalum Oxide Test Units.	4-43

LIST OF ILLUSTRATIONS (cont)

<u>Figure</u>		<u>Page</u>
26.	Normalized Curves of the Relative Tantalum Concentration Gradient in Stressed Units vs Oxide Thickness	4-45
27.	Normalized Curves of the Relative Tantalum Concentration Gradient in Stressed Units vs Oxide Thickness. (Samples No. 2, 10 and 7)	4-46
28.	Diffusion Constants for Radioactive Tantalum-Tantalum Oxide Test Units. (All points between arrows averaged to give D values in Table IV.)	4-48
29.	Bevel Cross Section After Etch - Taper Ratio 10,300:1	4-51
30.	Interferometric Profile of Beveled Interface	4-53
31.	Corning 7059 Glass Test Unit, Group 15, Thermal-Electrical Stress .	4-59
32.	Fused Quartz Test Unit, Group 15, Thermal-Electrical Stress	4-60
33.	Sapphire Test Unit, Group 15, Thermal-Electrical Stress	4-61
34.	Fotoceram Test Unit, Group 15, Thermal-Electrical Stress.	4-62
35.	Glazed Alumina, Group 15, Not Stressed	4-63
36.	Unglazed Alumina, Group 15, Thermal-Electrical Stress	4-64
37A.	Microscope Slide Test Unit, Group 15, Thermal-Electrical Stress . .	4-65
37B.	Microscope Slide Test Unit, Group 15, Thermal-Electrical Stress . .	4-66
38.	Corning 7059 Test Unit, Group 16, Thermal Stress	4-67
39.	Fused Quartz Test Unit, Group 16, Thermal Stress	4-68
40.	Sapphire Test Unit, Group 16, Thermal Stress	4-69
41.	Fotoceram Test Unit, Group 16, Thermal Stress.	4-70
42.	Glazed Alumina Test Unit, Group 16, Thermal Stress	4-71
43.	Unglazed Alumina, Group 15, Thermal Stress	4-72
44.	Microscope Slide Test Unit, Group 16, Thermal Stress	4-73
45.	Electron Micrographs of Tin Oxide Test Units	4-75
46.	Electron Micrographs of Tin Oxide Test Units	4-76
47.	Electron Micrographs of Tin Oxide Test Units	4-77
48.	Schematic Structure of Polycrystalline Tin Oxide Film.	4-80
49.	Energy Level Diagram at Grain Boundary.	4-82

SECTION 1

1. INTRODUCTION

Under RADC contract AF 30(602)-2593, Motorola initiated an investigation program on the primary modes of failure in solid state devices and components directed toward a study of chemical and physical phenomena occurring at an interface formed by two dissimilar materials in intimate molecular contact. The experimental approach has been based on the concept of building and evaluating thin-film model systems representing basic material interfaces found in solid state device technology.

Selection of a specific material interface to represent the metal film-dielectric film model system was based on the following general considerations:

1. applicability to current and anticipated state-of-the-art solid state device technology,
2. are prepared by a process technology in which all process parameters affecting the characteristics of the interface can be identified and controlled, and
3. are amenable to investigation by microscopic analytical techniques and electrical measurement.

Based on these considerations, models representing these interfaces were constructed from gas-plated and vacuum evaporated thin films of silicon oxide and modified silicon oxide glasses on vacuum-evaporated metal film electrodes, thin films of n-type semiconducting tin oxide deposited on a variety of substrate materials, and anodized tantalum films.

The experimental approach incorporated these interfaces in thin-film capacitors and resistors which were placed under electrical, thermal, and chemical environmental stresses. Electrical parameters were then measured as a function of stress and the observed modes of failure of particular models empirically correlated with specific model parameters unique to each material interface. These correlations provide the basis for subsequent experimental verification of specific failure modes by applicable analytical techniques.

The work on this contract has demonstrated the feasibility of using thin-film model systems to define material interfaces important in the study of primary modes of failure. The model systems chosen have been amenable to a large variety of electrical and physical measurements which are sensitive to changes in interface properties -- changes that reveal modes of failure.

Extensive data has been gathered on the electrical characteristics of stressed metal-dielectric interfaces and then analyzed by an electronic computer to obtain pertinent constants that define the frequency response of the capacitance and dissipation factors of the dielectric-model systems. This information can then be related to theoretical models of the metal-dielectric interface which in turn can be used to gain a basic understanding of the possible mechanism of failure. Simultaneously, analytical techniques, such as optical microscopy, radioactive diffusion studies, and mechanical strain measurements, have been developed to study surfaces and interfaces to further define and correlate specific modes of failure associated with devices under stress.

In a similar manner, extensive data on the resistivity and its temperature dependence, and the Hall effect as a function of temperature, was acquired on model systems representing interfaces between semiconducting tin oxide resistance films and various substrate surfaces. These model systems were subjected to thermal, electrical, and thermal-electrical stress, and the changes in the above properties observed and interpreted in terms of substrate properties. Optical and electron microscopic techniques were evaluated as possible analytical tools for further definition of failure modes.

SECTION 2

2. CONCLUSIONS

Certain general conclusions have been derived from this contract work. The investigation on the metal film-dielectric model systems has been most successful in providing the fundamental information necessary to identify and quantitatively define the characteristic mechanisms at these interfaces. The experimental data derived, i.e., frequency dispersion of capacitance and dissipation factors, is directly amenable to the derivation of mathematical models which define electrical characteristics in terms of the structure, composition, and geometry of the material across the interface. These electrical properties, i.e., dielectric constant, resistivity, distribution of relaxation time of polarizing dipoles, etc., are expected to vary with chemical composition of the interface, and, obviously with those stress levels which alter chemical composition and/or physical characteristics of the interface. Thus, mechanisms of failure, as indicated by changes in electrical characteristics that are quantitatively defined by mathematical models, can be related to changes in material properties. These changes in material properties can in turn be quantitatively defined in terms of "equations of state", such as solid state diffusion equations. Independent analytical measurements, such as diffusion studies using radioactive isotopes, provide the necessary correlation for defining failure modes.

Results of the investigations on the various semiconducting tin oxide film-substrate model systems have been revealing in terms of the qualitative nature of possible failure modes associated with the nature of the substrate interface. However, observation of changes in the basic conduction mechanism by measurement of the changes in the Hall effect as a function of thermal and electrical stress has not produced data descriptive enough to rigorously define the physical and chemical characteristics of the various substrate film interfaces. The difficulty does not lie with the experimental approach per se, but rather with the intrinsic nature of the semiconducting tin oxide film. That is, films deposited by a variety of techniques and with various doping levels were invariably electronically degenerate. Even though the initial resistivities of the as-deposited films were highly sensitive to the nature of the substrate interface, and subsequent thermal and electrical stressing, the degenerate character of the films limits the interpretation of the Hall data defining the changes in the conduction mechanism as a function of applied stress, nature of the substrate, and the chemical and physical structure of the film.

It was concluded that further investigations of these specific tin oxide model systems would not yield the information necessary to provide an adequate theoretical understanding of possible failure mechanisms in those systems. However, Hall-effect measurements, coupled with appropriate analytical techniques, should be valuable in understanding failure modes in those systems where the conduction mechanism is a sensitive function of film structure, impurities, and chemical composition. Such model systems could include films of the elemental semiconductors, silicon and germanium, and indium antimonide-type Group III-V compounds.

Specific conclusions derived from this work are summarized in detail in Section 4.

SECTION 3

3. RECOMMENDATIONS

Past efforts on this program have identified the interface between a metal film electrode and a thin-film dielectric as the one model system most representative of the type of material interfaces found in solid state active devices and integrated electronic thin-film circuitry. Future efforts should be directed toward model systems fabricated using thin-film dielectrics of glass and anodized tantalum films. There is a need to continue the previously initiated measurement program on the frequency dispersion of capacitance and dissipation factor of thin-film capacitors utilizing the model system interfaces. The time rate of change of these electrical characteristics with electrical and thermal stress, and the relationship of material parameters of the interface to these characteristics, will be correlated and interpreted by electronic computer programming techniques.

New series of electrical measurements should be initiated to fill in gaps in the experimental data and to provide a broader base of knowledge to identify failure modes. These measurements should include careful evaluation of the effect of bias voltage on capacitance, the temperature coefficient of capacitance and dissipation factor as a function of frequency, leakage current-applied voltage relationships, and power dissipation density levels.

Studies of material diffusion processes occurring in the dielectric and across the material interface as functions of thermal and electrical stressing should be carried out using radioactive isotope tracer techniques. Previously initiated studies on the tantalum-tantalum oxide systems should be expanded and new diffusion studies initiated on the glass-dielectric model systems.

Optical microscopic techniques, developed during the initial contract period to expose and delineate material interfaces, should be applied to the model systems. Thermal microscopy and electron microscopy should be used to extend the analytical investigation of the structural properties of the interface and dielectric.

From the above studies, it should be possible to define mechanisms of failure in terms of mathematical models which describe the time rate of changes of electrical, chemical and physical properties of material interfaces in terms of intrinsic material parameters and extrinsic electrical characteristics.

SECTION 4

4. DISCUSSION

The following discussion summarizes the first three quarter's effort on the contract and details the effort during the final quarter.

4.1 METAL ELECTRODE-DIELECTRIC INTERFACE

4.1.1 Summary of Past Work

4.1.1.1 Glass Dielectric-Metal Electrode Interface

Investigation of the glass dielectric-metal interface has indicated that modes of failure are associated with structural defects in the dielectric, chemical reaction and mechanical interaction at the interface, and certain fabrication process parameters.

Pinhole defects in evaporated silicon monoxide dielectrics and the extent of intrinsic porosity and microscopic defects in gas plated silicon oxide glass dielectrics have been revealed by silver diffusion studies. Large leakage currents and low breakdown voltages have been correlated with these dielectric defects. Catastrophic failures have been associated with devitrification of glass dielectrics under thermal-electrical stress. Migration of the electrode material into the dielectric may catalyze the observed crystallization by acting as nucleating sites.

Failure due to chemical reaction at the electrode-dielectric interface has been observed directly at the interface of aluminum electroded silicon dioxide dielectrics and has been associated with discoloration brought about by chemical reduction of the oxide dielectric by the aluminum. The frequency dispersion of capacitance and dissipation factor curves indicate the presence of resistivity gradients in the dielectric and interfacial polarization brought about by chemical reaction at the interface. The enhancement of the effect in samples with thinner dielectric layers seems to confirm the postulated interface reaction. In a similar manner, the variation of the temperature coefficient of capacitance with thickness is correlated with interfacial reactions and electrode diffusion phenomena.

Failure due to mechanical incompatibility of the dielectric and electrode has been demonstrated by the crazing of thermally stressed aluminosilicate dielectrics deposited on silver electrodes. Surface diffusion of the silver apparently sets up stresses in the dielectric resulting in crack and blister formation.

A fabrication process parameter affecting the properties of the glass dielectric-metal electrode interface is the time interval and the nature of the ambient between successive depositions of electrode-dielectric-electrode film. Surface adsorption of water and active gases at the interface can initiate chemical reactions at the completed interface.

4.1.1.2 Tantalum-Tantalum Oxide Interface

Similar observations have been made on the failures originating at the tantalum-tantalum oxide interface. Microscopically observed dielectric defects such as blistering and pinholes have been related to catastrophic failures. Poor substrate adhesion of the tantalum film and

impurities in the film create the defects. Voltage induced crystallization of the dielectric has also been revealed by optical microscopy.

The dielectric thickness dependence of the frequency dispersion curves of capacitance and dissipation factor and the temperature coefficient of capacitance curves indicate the relationship of the interface to electrical characteristics. Diffusion of tantalum across a stressed interface into the dielectric producing a possible resistivity gradient has been observed using radioactive isotopic tracer techniques. The concept of a resistivity gradient suggests a mathematical model which very nearly approximates the capacity and dissipation factor curves.

Anodization processing parameters such as current density, anodizing bath temperature, and back-etching will affect the oxide dielectric film structure and subsequent electrical behavior.

4.1.2 Electrical Measurements

The utilization of very thin dielectric films provides an opportunity to observe the manifestation of the interface in the electrical properties of the capacitor, since the interfacial region, which may extend to a depth of only a few angstroms into the dielectric, can provide a measurable contribution to the over-all properties of the capacitor. This is in contrast to the case of comparatively thick dielectric films, as exist in conventional capacitors for electronic use.

The ultimate objectives of this program are to determine the chemical, physical, and electrical properties of dielectric-metal interfaces in thin-film capacitors. It is hoped that this will generate a better understanding of the behavior of the interface as related to useful capacitor properties, and particularly the reliability of such capacitors. Attempts are being made to interpret the measurement data obtained on a unit in terms of the chemical structure of the interface.

It is expected that the transition from a metal electrode to a dielectric material does not consist of an abrupt surface separating pure metal from pure dielectric, but of a region in which the chemical composition varies more or less continuously from the metal to the dielectric. Further, the characteristics of this region of variation may be expected to be affected by the environmental stresses to which the unit is subjected, such as high temperature, electrical stress, and humidity. The measurement data being obtained do indeed indicate that such environmental stresses affect the subsequent electrical characteristics of the devices, although the interpretations of the data are tentative at this point.

4.1.2.1 Measurement Techniques

To provide a firm basis for comparison and interpretation, a "standard" series of environmental stresses and measurements was adopted. After fabrication, a series of measurements is taken on each unit. These measurements include an initial measurement of leakage current at room temperature, which is primarily used to cull out capacitors which have abnormally high leakages. Following this, the capacitance and dissipation factor are carefully measured over a frequency range of 30 cps to 300 kc at room temperature.

Each unit is then subjected to a series of environmental stresses, with capacitance and dissipation factor versus frequency measurements being made after each environmental period. The environmental stresses are as follows:

1. 24 hours at 80 C
2. 24 hours at 95-per cent relative humidity
3. 168 hours at 125 C
4. 24 hours at 95-per cent relative humidity

All measurements of capacitance and dissipation factor are being made with the General Radio type 716-C capacitance bridge. The accuracy of this instrument is ± 0.1 per cent ± 1 pf of capacitance, and ± 0.0005 or ± 2 per cent of dial reading, whichever is larger, for the dissipation factor. Measurements of capacitance and dissipation factor at temperatures other than room ambient are made with the help of the General Radio type 716-P4 guard circuit. The guard circuit consists essentially of a Wagner ground configuration, which permits the remote measurement of capacitors to an accuracy equivalent to that which would be obtained were the capacitor connected directly to the bridge terminals. The Wagner ground configuration effectively cancels out the capacitance of loads and cables connecting the capacitor under measurement to the capacitance bridge.

The consistency of the measurement data indicates that the accuracy of measurement of small changes in capacitance is probably considerably better than the published accuracy of the bridge. For example, the published accuracy figures for the bridge predict that a measurement of a 500-picofarad capacitor should be accurate to within ± 0.5 picofarads. Measurements that have been taken at Motorola, however, indicate that a measurement of the difference in the capacitance measured at, say, 100 cps and 100 kc is probably accurate to better than 0.2 picofarads.

All measurements are taken with 1 volt RMS ac applied to the capacitor.

The 95-per cent relative humidity environment was produced by placing the capacitors in a desiccator jar containing sodium sulphate crystals in equilibrium with water.

4.1.2.2 Data Analysis

Early in the program, it became obvious that some method of mechanized data processing of the measurement information would be essential to conveniently handle the information being gathered. Plots of one of the initial data of capacitance and dissipation factor versus frequency indicated that for a great many of the units under test, a plot of capacitance versus the logarithm of frequency is a nearly straight line. This was particularly true of tantalum capacitors. Consequently, it was decided to apply least squares curve fitting techniques to the analysis of the measurement data, in such a way as to produce the coefficients of a power series of the capacitance in terms of the logarithm of the frequency.

It was further decided that plots of normalized reciprocal capacitance would be much more useful in the following analyses.

A program for the General Electric 225 computer was adapted to accomplish the desired data analysis tasks. The program operates basically on a least squares curve fitting

technique, except that it permits the fitting of one or more dependent variables to arbitrary functions of a number of independent variables, rather than being restricted to a simple power series polynomial curve fit. The techniques are basically the same as those used for a polynomial fit. The program accepts the data from a series of measurements on a capacitor over a range of frequencies, and then computes the coefficients, on a least squares error criterion, for a curve of the following form:

$$\frac{C_{1 \text{ kc}}}{C(f)} = a_0 + a_1 \ln f + a_2 (\ln f)^2 + a_3 f \quad (1a)$$

$$D = b_0 + b_1 \ln f + b_2 (\ln f)^2 + b_3 f \quad (1b)$$

where

$C_{1 \text{ kc}}$ = capacitance measured at 1 kc,

$C(f)$ = capacitance as a function of frequency,

f = frequency,

D = dissipation factor.

Equation (1a) fits the fractional change in reciprocal capacitance to a polynomial of logarithms, plus a term proportional to f . The dissipation factor is fitted to a similar curve. The frequency term is included in the equations to allow for the upswing of the dissipation factors at high frequency. This upswing results from a series resistance of the electrodes and wires of the capacitor, which becomes significant at higher frequencies as the reactance of the capacitor becomes comparable to the resistance. The equivalent series electrode resistance can be computed from the values of the capacitor and the term b_3 by the following relation:

$$R = \frac{b_3}{2C} \quad (2)$$

The program was designed with maximum flexibility to accommodate future needs in processing of data. All input and output information is being stored on magnetic tape so as to be quickly accessible should further analysis be desired. The computer facilities being used do not include off line card-to-tape equipment. Consequently, the comparatively time-consuming process of reading punched cards into the machine is fairly expensive where large amounts of data are being used. Storage of all data on tape will permit re-use of this data in the future, without requiring that it be repeatedly read into the computer from punched cards.

4.1.2.3 Interpretations of Results

The behavior capacitance and dissipation factor as functions of frequency are of particular interest since they are dependent on the relaxation time of the dielectric polarization mechanism and upon the variation in stoichiometry of the dielectric film at the interfaces (assuming such a variation exists). The anodized tantalum oxide capacitor, for example, exhibits an almost linear decrease in capacitance with the logarithm of frequency over frequency ranges of several decades. The dissipation factor showed a slight decrease with

increasing frequencies until a frequency is reached where the series electrode resistance of the capacitor becomes comparable to the capacitor reactance (see Figure 2). Figure 1 depicts the same data with capacitance plotted in normalized reciprocal form. The quantity plotted on the ordinate is:

$$\frac{C_{1kc}}{C(f)} - 1$$

There are two basic mechanisms which could cause effects such as these shown here. One such mechanism involves the intrinsic properties to the dielectric whereas the other depends upon the characteristics of the dielectric-metal electrode interface.

If a dielectric medium is predominated by polarizing dipoles with a relaxation time, τ , the dielectric constant will exhibit a decrease as the angular frequency increases through $\frac{1}{\tau}$, while the dissipation factor shows the maximum in the vicinity $\frac{1}{\tau}$. However, if a dielectric has polarizing dipoles with the proper distribution of relaxation times, behavior similar to that shown on the curves in Figures 1, 2 and 3 could result.*

This type of behavior will also result if the stoichiometry of the dielectric film varies in the direction normal to the interfaces in such a way that the dielectric resistivity varies exponentially with position in the direction normal to the interface. The capacitance will then decrease in a linear manner with the logarithm of frequencies.

Since the dipole polarization and interfacial polarization can give the same effects on the capacitance versus frequency curves, a determination of relative importance of the two mechanisms in any particular case cannot be made from these electrical measurements alone, but must be implied from other measurements, such as the behavior of capacitors of different dielectric thicknesses, etc. Measurements such as those depicted here have shown that for tantalum capacitors of various thicknesses, the slope of the reciprocal capacitance versus logarithm frequency curve is dependent upon the dielectric thickness, and does in fact, vary inversely with the thickness of the dielectric. This would seem to indicate that effects at the interface are the important mechanism producing the decrease in capacitance with increase in frequency, since the results of several workers with tantalum films has indicated that the intrinsic properties of tantalum oxide films are basically independent of the film thickness so long as the films are formed under the same conditions.

Tentatively assuming that the variation of capacitance and dissipation factor with frequency are predominantly caused by interfacial effects, and that these effects are manifest primarily in a variation of resistivity with position, the frequency behavior was computed for a simple mathematical model of the interface.

The assumption was made that the resistivity of the material in the region of the interface varied exponentially with position:

$$\rho(x) = \rho_0 \exp\left(-\frac{x}{x_0}\right) \quad (3)$$

*L. Young (Reference 5) discusses a possible mathematical model which defines a "proper" distribution of dipole relaxation times.

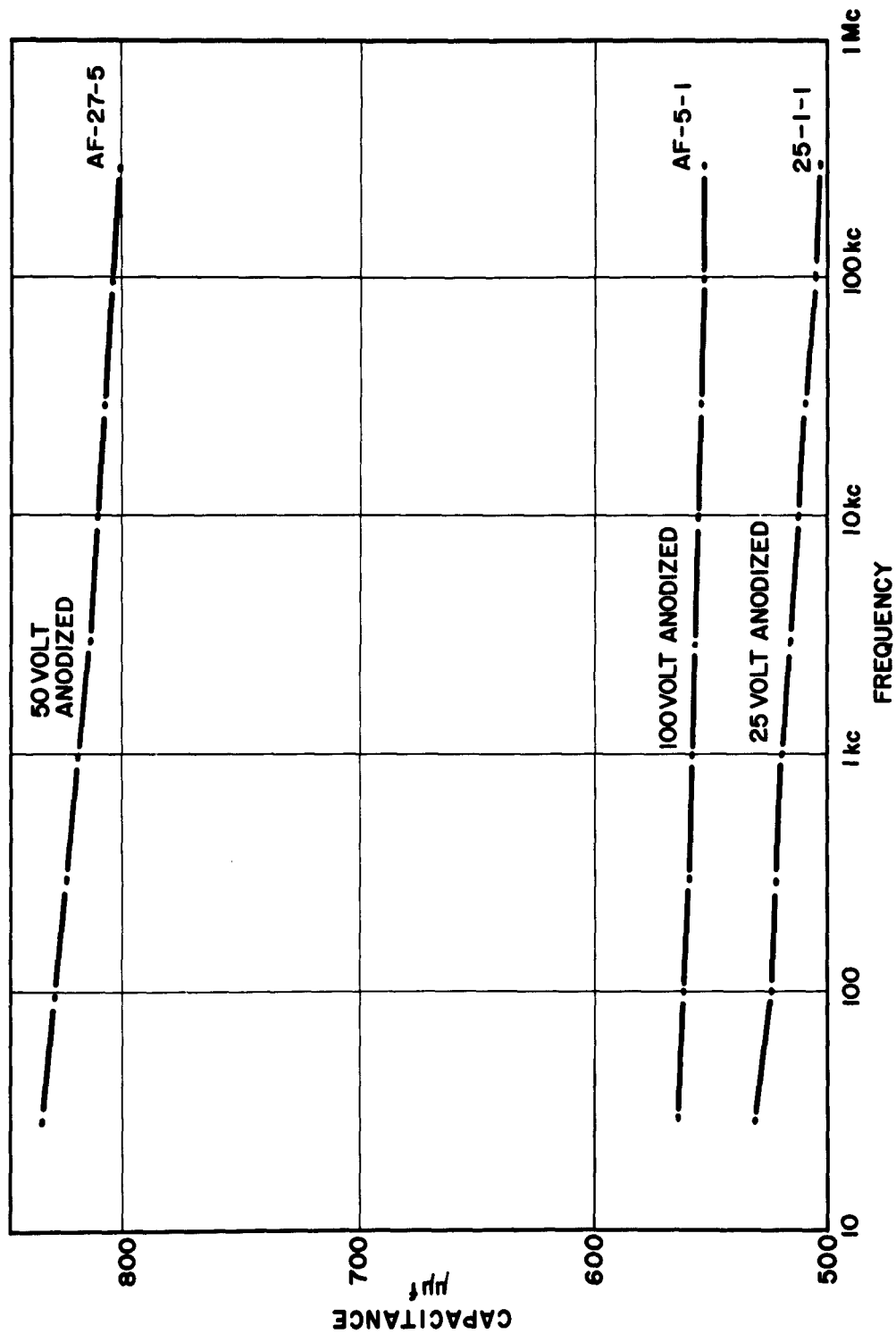


Figure 1. Capacitance Versus Frequency for Thin Film Tantalum Capacitors

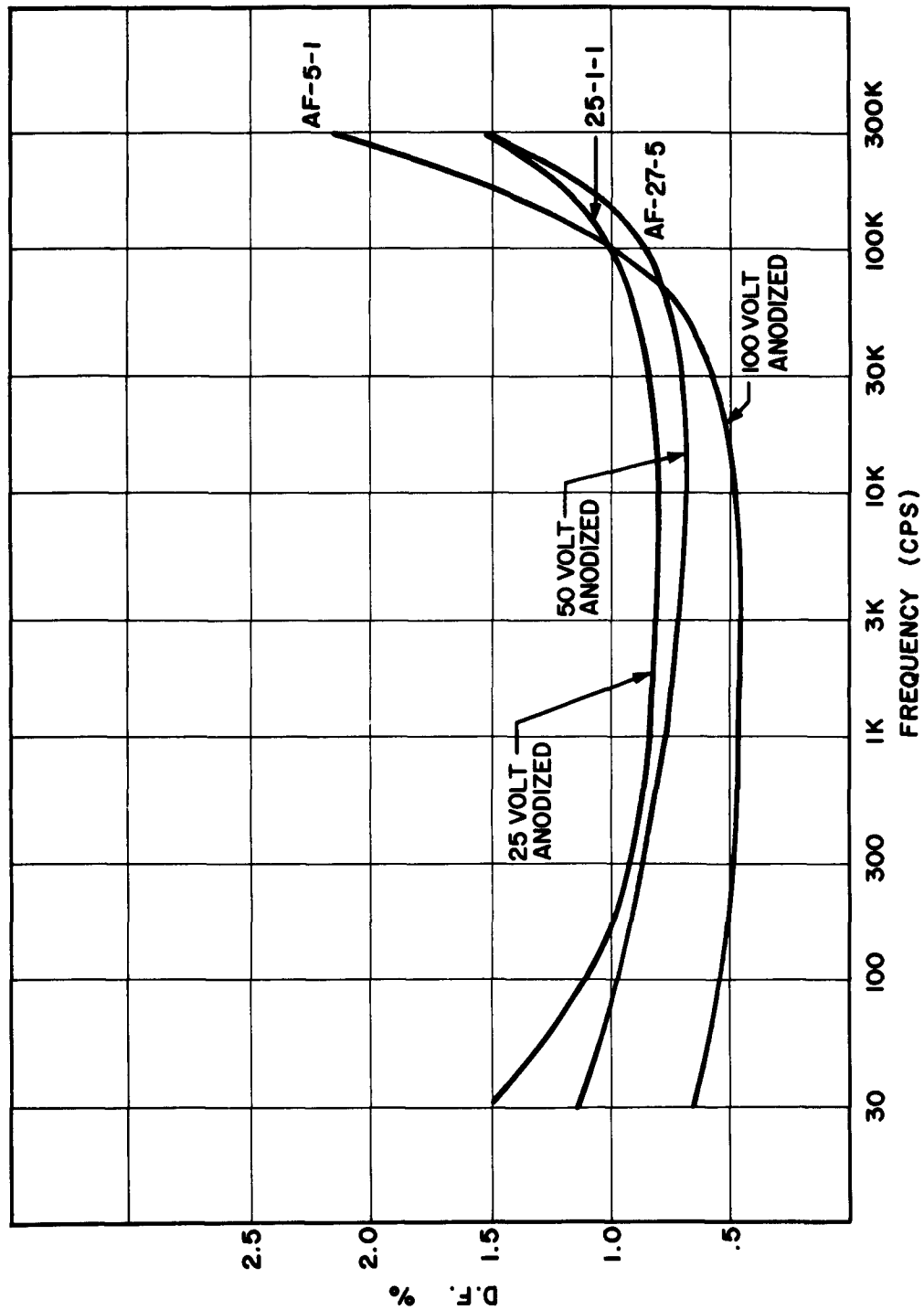


Figure 2. Dissipation Factor Versus Frequency for Thin Film Tantalum Capacitors

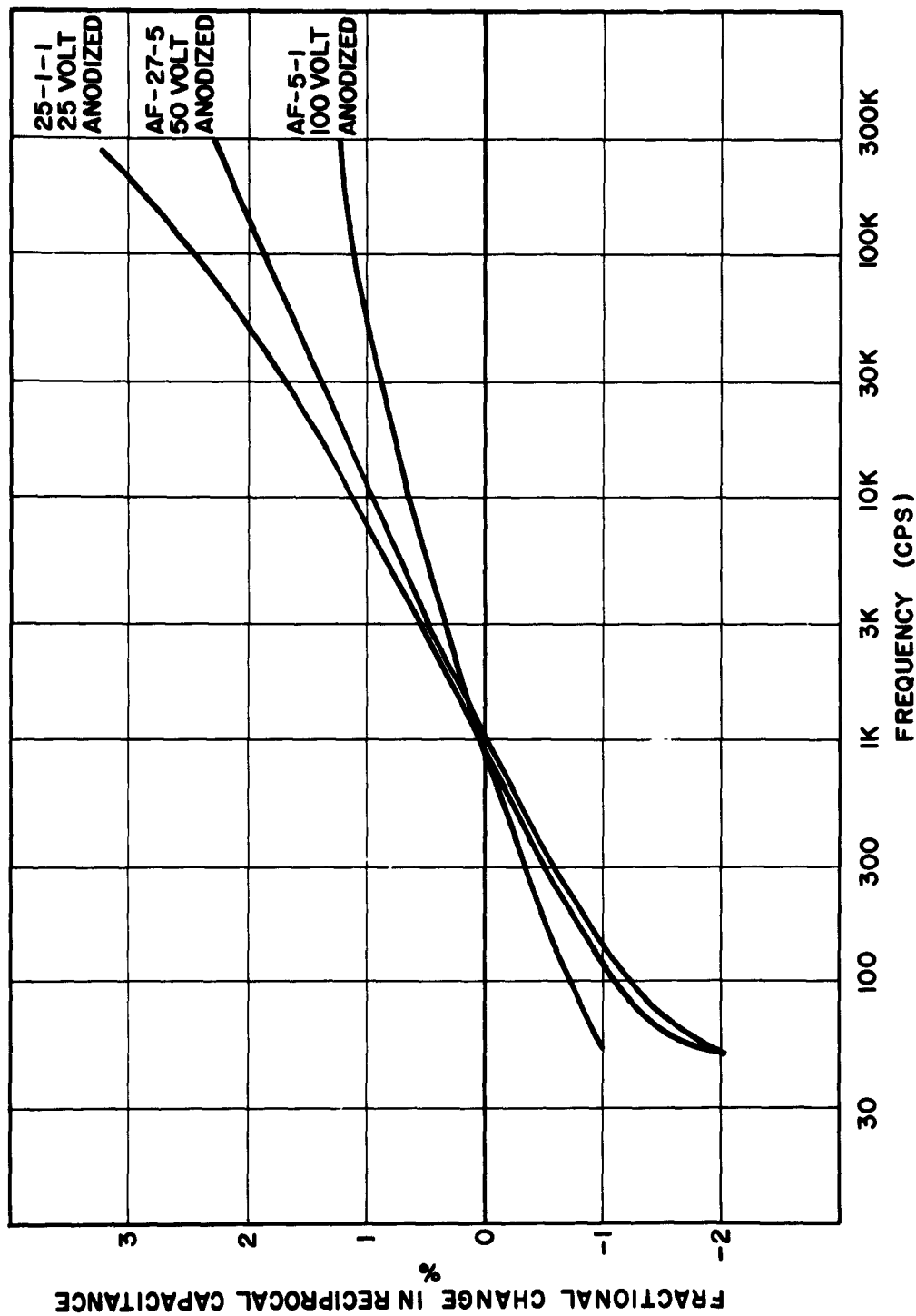


Figure 3. Reciprocal Capacitance Variation ($C_{1kc}/D-1$) Versus Frequency for Thin Film Tantalum Capacitors

where

$\rho(x)$ = resistivity,

ρ_0, x_0 = constants,

x = position normal to interface.

The capacitance and dissipation factor were then computed from an equivalent circuit such as that shown in Figure 4, giving a frequency behavior as follows:

$$\begin{aligned} \frac{C_{1 \text{ kc}}}{C(f)} - 1 &= \frac{x_0}{t} \ln \frac{f}{1 \text{ kc}} \\ D &= \frac{\pi}{2} \frac{x_0}{t} - \frac{\pi}{2} \left(\frac{x_0}{t} \right)^2 \ln \frac{f}{1 \text{ kc}} \end{aligned} \quad (4)$$

where

t = dielectric thickness.

From the measurement data on tantalum capacitors, the constant x_0 in the above equations turns out to be of the order of 4 angstroms. Although the slope of the dissipation factor curve is not that predicted by Equation (4), the value of dissipation factor at 1 kc is in reasonable agreement with that predicted by Equations (4).

It is to be emphasized that although the measurement results are in fairly close agreement to the predictions of Equations (4), this does not mean that the assumptions made were the correct ones. Indeed, as mentioned earlier, it is possible to hypothesize a layer of dipoles at the dielectric-metal interface with a distribution of relaxation times. With the proper distribution, properties similar for those derived above can be obtained without the assumption of a varying resistivity of the material. Moreover, this model will exhibit the observed variation of these properties with thickness of the dielectric.

4.1.2.4 Typical Experimental Results . . .

4.1.2.4.1 Tantalum Oxide Dielectrics - Some typical results are given here for tantalum capacitors. The capacitors were fabricated on glazed ceramic substrates with a film of tantalum evaporated to a thickness of approximately 2500 angstroms at a vacuum of approximately 2×10^{-5} Torr. A film of aluminum (thickness approximately 2500 angstroms) was evaporated onto the substrate prior to the tantalum evaporation to produce a satisfactorily low resistance of the lower electrodes to permit good measurements at higher frequencies. The tantalum films were anodized to 25, 50 and 100 volts in a 5-per cent solution of phosphate at room temperature, with an initial current of 1 ma per square centimeter of film area. Top electrodes of pure gold were evaporated onto the tantalum following anodization.

Figures 5 and 6 show curves of capacitance and dissipation factor of one of these units after various environmental stresses. High temperature and aging tend to reduce both the 1 kc value of the capacitance, and the slope of the capacitance versus frequency curves, whereas aging at high relative humidity tends to have the reverse effect. These effects, however, apparently are not completely reversible, since it will be seen that the

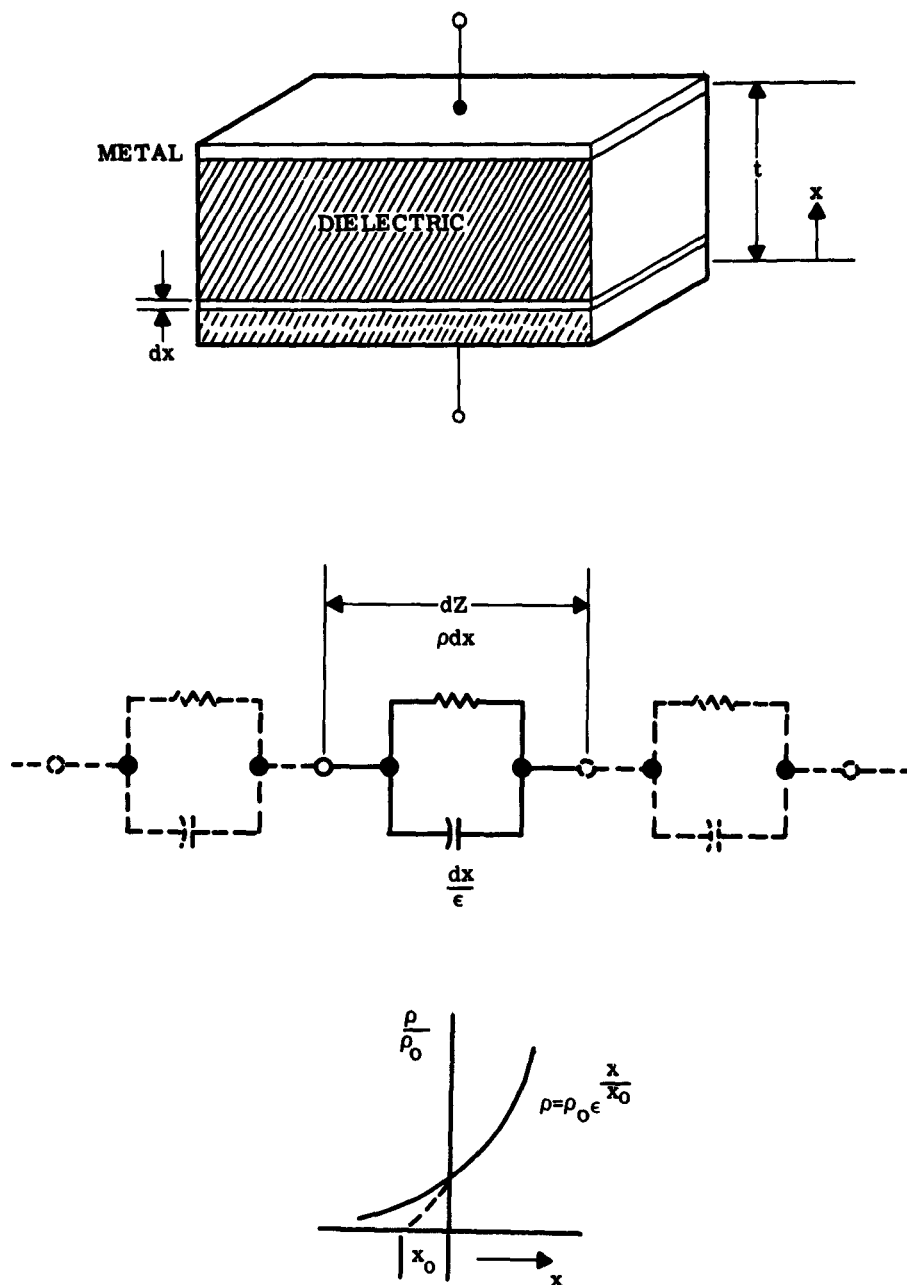


Figure 4. Model of Dielectric-Metal System, its Equivalent Circuit, and Plot of Resistivity Versus Position

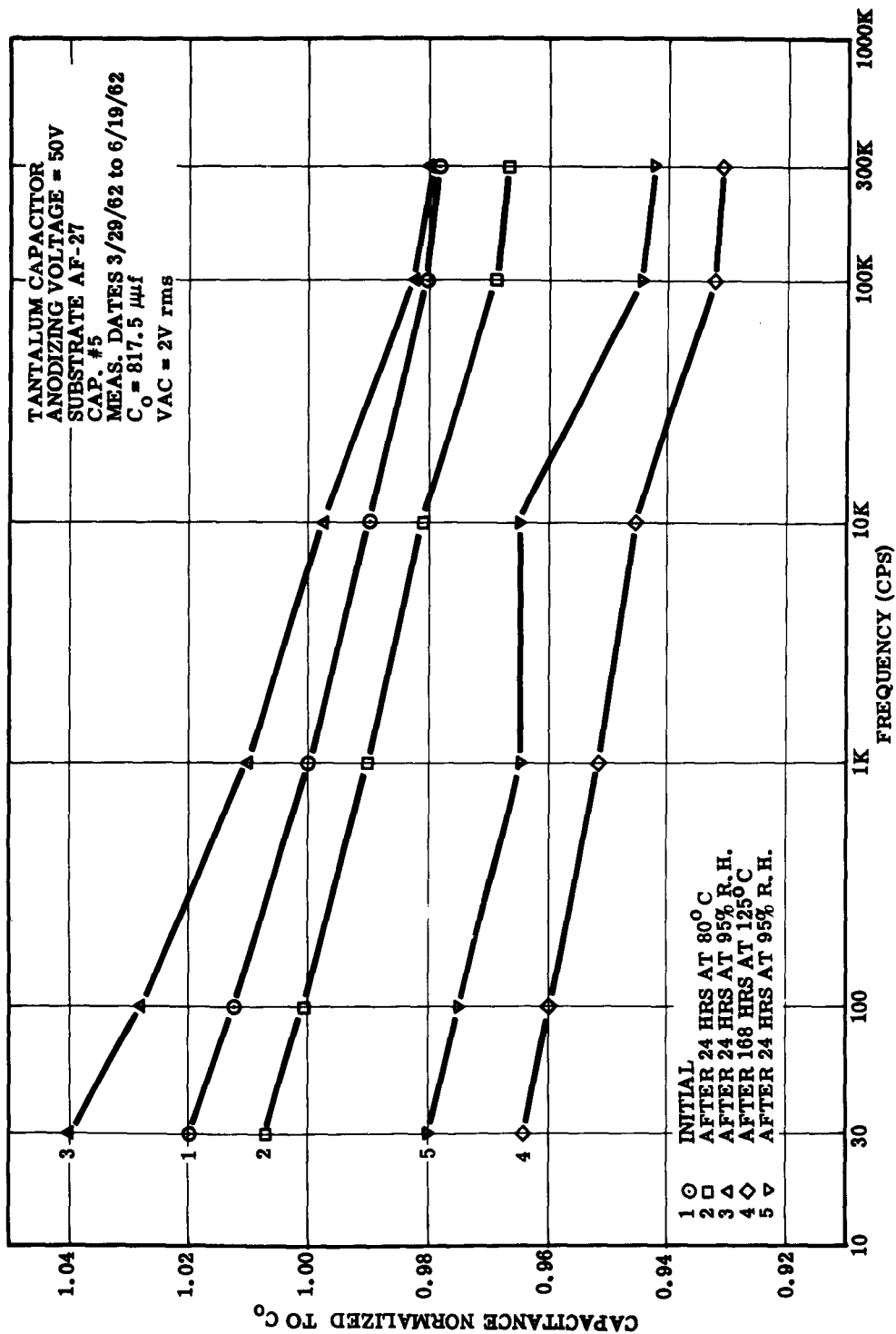


Figure 5. Normalized Capacitance Versus Frequency for a Thin Film Tantalum Capacitor. The Various Curves are from Measurements taken at Room Temperature following the Indicated Environments.

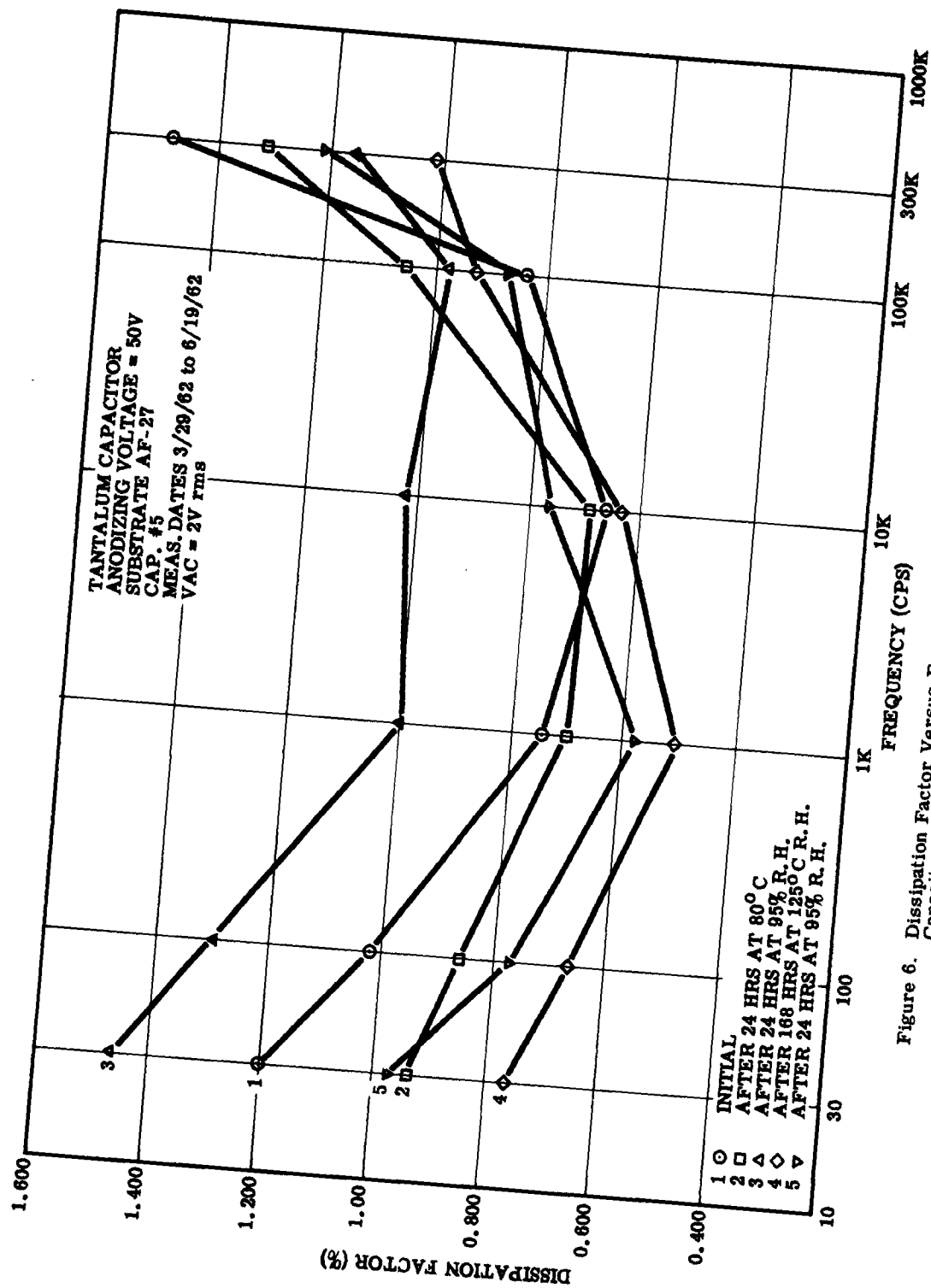


Figure 6. Dissipation Factor Versus Frequency for a Thin Film Tantalum Capacitor. These Curves Correspond to the Capacitance Curves in Figure 4.

increase in capacitance after the high relative humidity environment following 160 hours at 125 C is considerably less than that following 24 hours at 80 C (curves 5 and 6 compared with curves 2 and 3).

The coefficients of the curve fits for the data plotted in Figures 5 and 6 are shown in Table I, along with data from two other capacitors of different dielectric thicknesses. Only the coefficients a_0 , a_1 , b_0 , b_1 are shown, although the fits were made to Equations (1). Data for all three fits on each capacitor were normalized to the first 1 kc reading on each unit, to facilitate the comparison of data, i.e., " $C_{1\text{kc}}$ " in Equations (1) is identical for all curve fits for a capacitor in Table I.

It will be seen from Table I that the reciprocal capacitance shows a general increase (a_0) after high temperature environment, and a decrease after a high humidity environment. The slope (a_1) of the reciprocal capacitance curve generally shows a decrease after high temperature environment, and a comparatively large increase after high humidity. Moreover, these changes are of greatest magnitude with thin dielectric films.

TABLE I. CURVE FIT COEFFICIENTS FOR THIN-FILM TANTALUM CAPACITORS						
$\frac{C_{\text{init. 1kc}}}{C(f)} - 1 = a_0 + a_1 \ln f + a_2 (\ln f)^2 + a_3 f$ $D = b_0 + b_1 \ln f + b_2 (\ln f)^2 + b_3 f$						
Unit	Anod. Vltg.	a_0 Per Cent	a_1 Per Cent	$\frac{\pi}{2} a_1$ Per Cent	b_0 Per Cent	b_1 Per Cent
<u>Initial Readings</u>						
25-1-1	25	-.02	.507	.797	.785	-7.25
AF27-5	50	-.36	.483	.758	.760	-8.71
AF-5-1	100	+.05	.261	.410	.409	-4.74
<u>After 24 hours at 80 C</u>						
25-1-1	25	-.207	.455	.715	.648	-6.70
AF27-5	50	+.88	.486	.763	.686	-2.11
AF-5-1	100	+.22	.217	.341	.314	-3.32
<u>After 72 hours at 95 per cent relative humidity, 28 C</u>						
25-1-1	25	-3.71	.914	1.43	1.39	-20.5
AF27-5	50	-1.18	.686	1.06	1.055	-7.50
AF-5-1	100	-0.78	.357	.561	.535	-3.89

Values of $\frac{\pi}{2} a_1$ are also tabulated in Table I for comparison with 1 kc values of the dissipation factor (b_0). Equations (4) predict that $\frac{\pi}{2} a_1$ will be equal to b_0 , and Table I shows this to be very nearly the case.

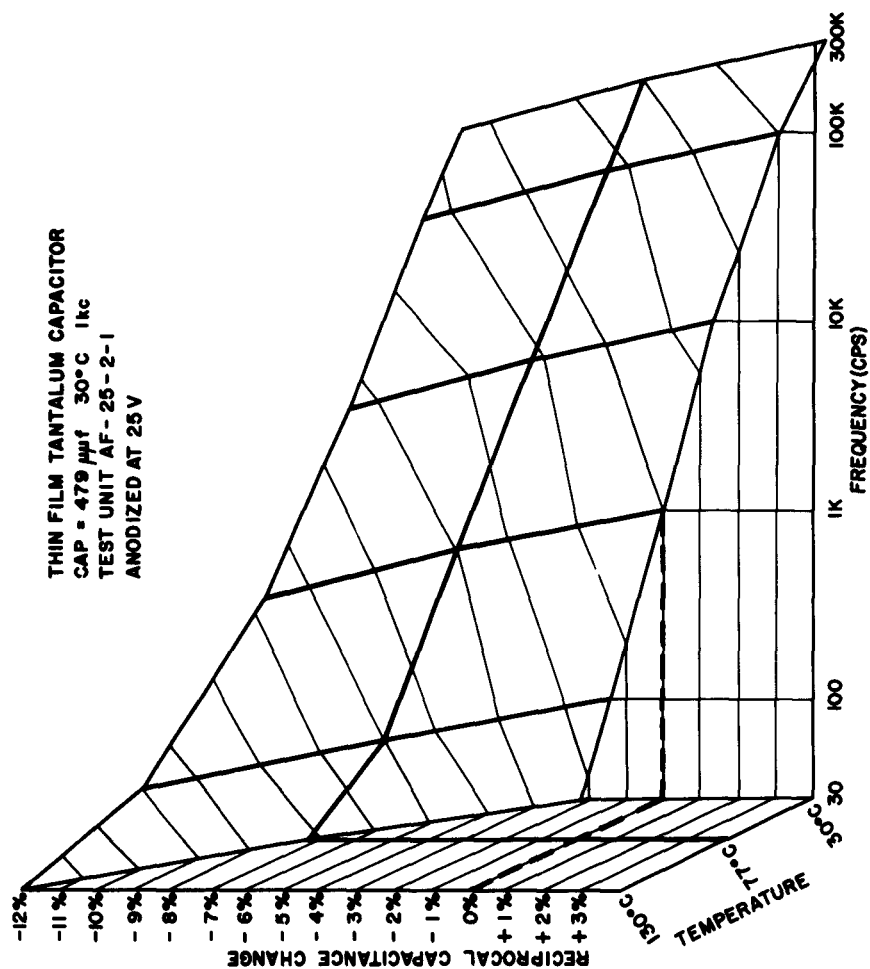


Figure 7. Reciprocal Capacitance Variation (C_{init} , 1 kc/C-1) Versus Temperature and Frequency for a Thin Film Capacitor Anodized to 25 volts. (Note vertical coordinate reversal.)

THIN FILM TANTALUM CAPACITOR
 CAP = 161 μ pf 30°C 1kc
 TEST UNIT AF-24-1
 ANODIZED AT 100V

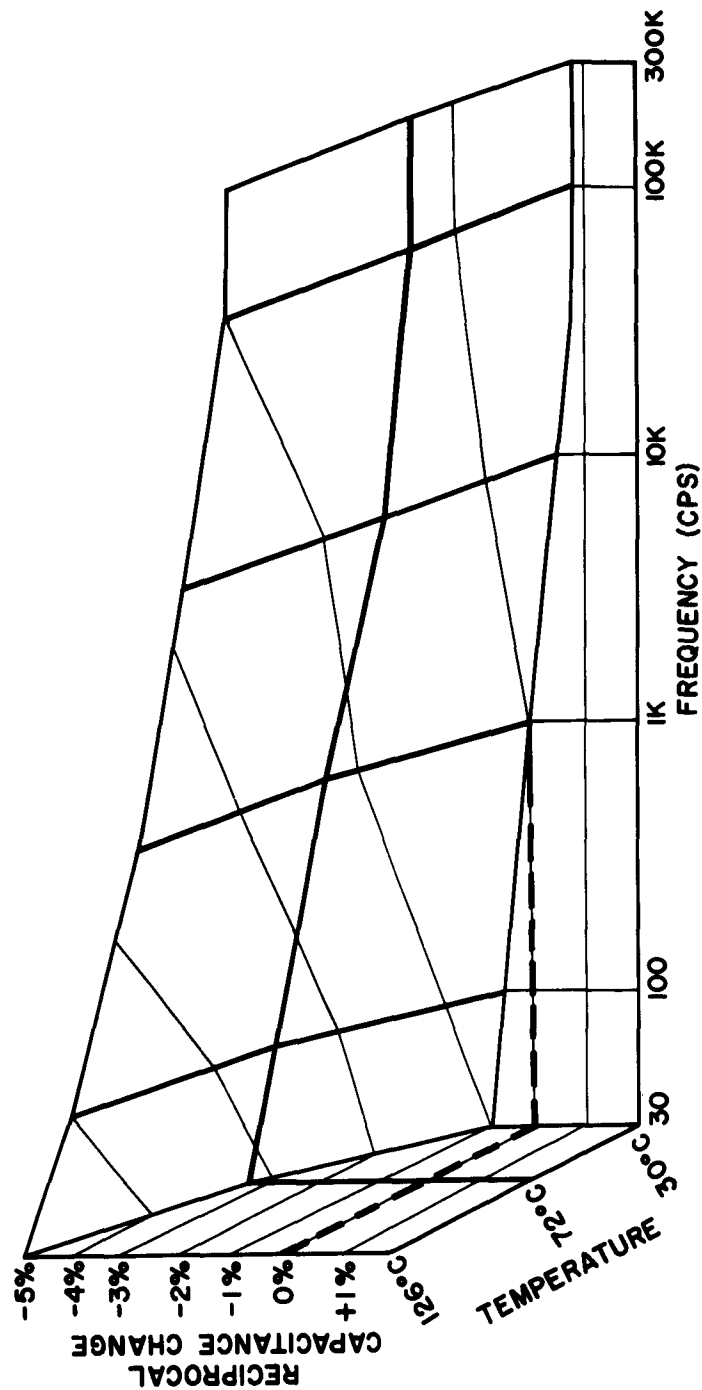


Figure 8. Reciprocal Capacitance Variation Versus Temperature and Frequency for a Thin Film Tantalum Capacitor Anodized to 100 volts. (Note vertical coordinate reversal)

Measurements of capacitance versus frequency and temperature yield surfaces such as those depicted in Figures 7 and 8. It will be noted from the curves that the variation of capacitance versus frequency is much stronger at higher temperatures than at low temperatures; that is, the temperature coefficient versus capacitance is considerably higher for low frequencies than it is for high frequencies. These characteristics can be correlated with the interface model previously described (involving a variation in resistivity with position) insofar as the resistance of the material in the interface may be expected to decrease as the temperature rises, producing easier conduction in the interface region, and decreasing the effective thickness of the dielectric.

4.1.2.4.2 Silicon Monoxide Dielectrics - Tests similar to those made on tantalum capacitors were performed on a series of capacitors utilizing SiO dielectrics. The capacitors had evaporated chromium electrodes, with an evaporated silicon monoxide dielectric of approximately 3 micron thickness. Measurements of capacitance and dissipation factor over a range of frequencies were made on these units after various environmental stresses. A set of measurements was taken immediately after capacitor fabrication (see Figure 9) after 24 hours aging at approximately 80 C, after 24 hours at 95-per cent relative humidity at room temperature, after one week at 125 C, and finally, after 24 hours at 95-per cent relative humidity at room temperature. Excerpts of the measurement data from the three typical units are shown in Table II. The capacitance figures in Table II show the percentage variations in capacitance relative to the value at 1 kc after one week aging at approximately 125 C. These values vary from +12 per cent in the initial measurement at 100 cps, to -3.9 per cent in the final measurement of the unit at 100 kc.

The general trend of these figures is somewhat different from that resulting from measurements on tantalum capacitors. One of the more noticeable factors in this trend is the fact that the units suffer little or no effect from aging in a high humidity environment. Aging at elevated temperatures, however, results in a general decrease in the capacitance of the unit, a slight leveling of the capacitance versus frequency curve, and a slight decrease in the dissipation factors. It would appear that these effects are not due to a simple dehydration of the dielectric film or interface, since exposure to high relative humidity does not appreciably reverse the effect. The effects are probably due to one of three processes:

- (a) a change in the morphous structure of the film,
- (b) a change in the degree of oxidation of the silicon monoxide, or
- (c) a change in the structure of the dielectric-metal interface, probably due to migration of the chromium metal and into the dielectric.

Unfortunately, insufficient data is available for dielectrics of thicknesses other than those listed here to draw any valid conclusions on the effect of dielectric thickness on the process, which would probably indicate whether the effects were primarily due to phenomena at the dielectric-metal interface, or due to phenomena in the entire dielectric film. Several units were fabricated with metals other than chromium as electrode materials, but most of these failed during early stages of the test program, so that meaningful data is not available in these cases.

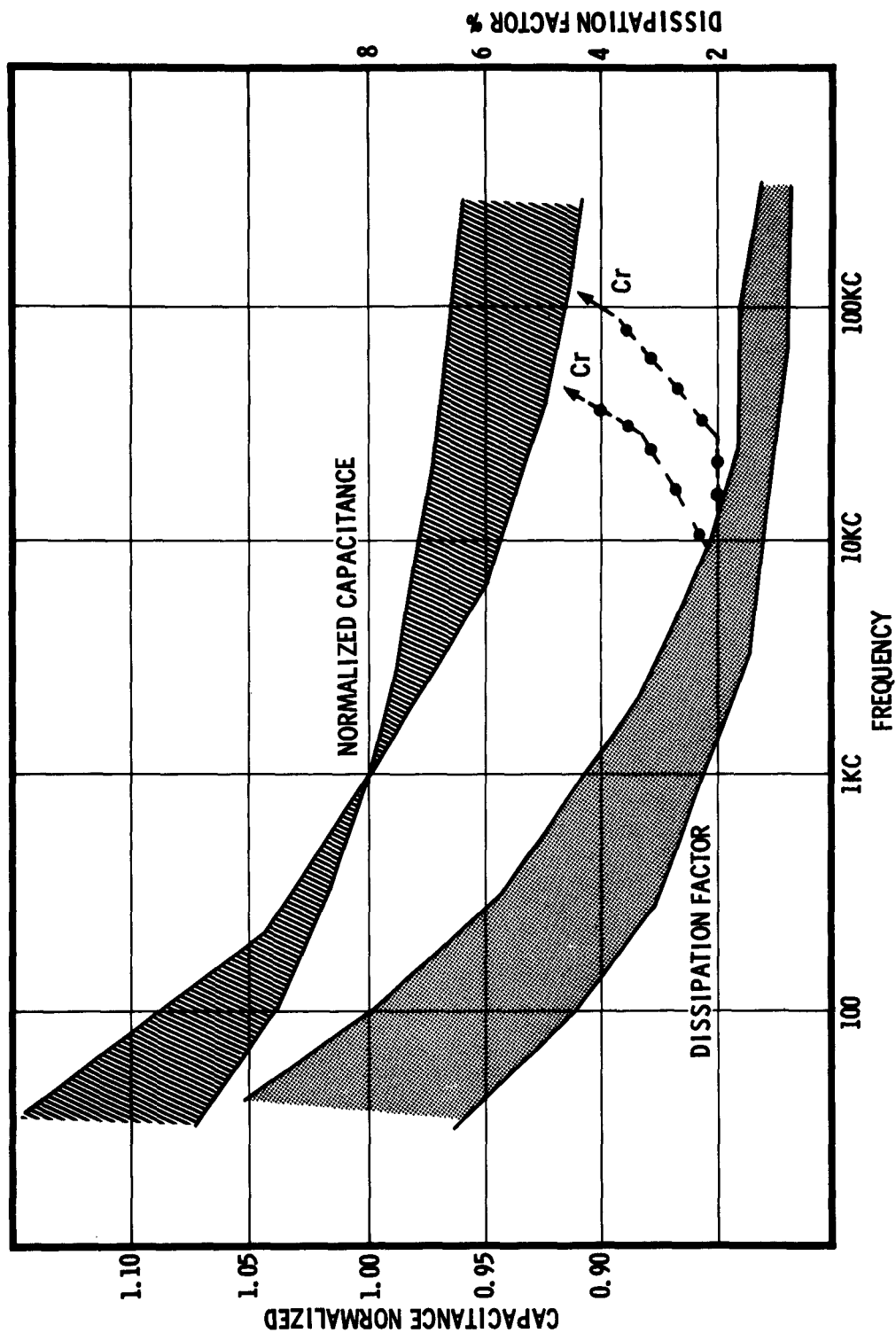


Figure 9. C/C_{1kc} , D.F. vs Frequency for SiO Test Units with Al, Cr, Cu, Au, Ag Electrodes

TABLE II. TYPICAL CHARACTERISTICS OF SILICON MONOXIDE THIN-FILM CAPACITORS							
Cr Electrodes, 3 Micron Dielectric Thickness							
Unit No.	Environmental Stress			Reciprocal Capacitance - Percentage Difference from value at 1 kc after 125 C Environment			Dissipation Factor at 1 kc Per Cent
	Relative Humidity %	Temp. oC	Duration Hours	freq=100 cps Per Cent	1 kc Per Cent	100 kc Per Cent	
D3-2				+7.14	+1.90	-2.77	2.65
D3-16				+12.05	+3.39	-1.36	3.38
D3-19				+6.63	+1.30	-3.08	2.70
24 hours at 80 C							
D3-2		77	24	+5.41	+0.97	-3.22	2.38
D3-16		77	24	+6.11	+0.99	-3.28	2.62
D3-19		77	24	+5.68	+0.72	-3.38	2.58
95 per cent relative humidity							
D3-2	95		18	+5.60	+0.90	-3.25	2.38
D3-16	95		20	+6.67	+1.17	-3.28	2.8
D3-19	95		22	+5.84	+0.81	-3.36	2.67
125 C							
D3-2		125	168	+3.80	0.0	-3.76	2.13
D3-16		125	168	+4.35	0.0	-3.95	2.31
D3-19		125	168	+4.29	0.0	-3.66	2.33
95 per cent relative humidity							
D3-2	95		24	+3.70	-0.06	-3.76	2.09
D3-16	95		24	+4.45	+0.03	-3.92	2.35
D3-19	95		24	+4.29	-0.05	-3.75	2.34

4.1.2.4.3 Silicon Dioxide Dielectrics - Several capacitors utilizing thin films of vapor-plated silicon dioxide as a dielectric were fabricated and tested. The dielectric thickness was approximately 3000 angstroms. Tests were completed on units having chromium as electrode material, and gold as electrode material.

The tests on these units were basically the same as those run on the silicon monoxide dielectric capacitors, and these are summarized for typical units in Table III and illustrated in Figure 10. The changes in capacitance and dissipation factors for these units were much greater than for either the SiO₂ or Ta₂O₅ dielectric film. Indeed, capacitance changes of nearly 200 per cent were observed in some units. Contrary to the case of the

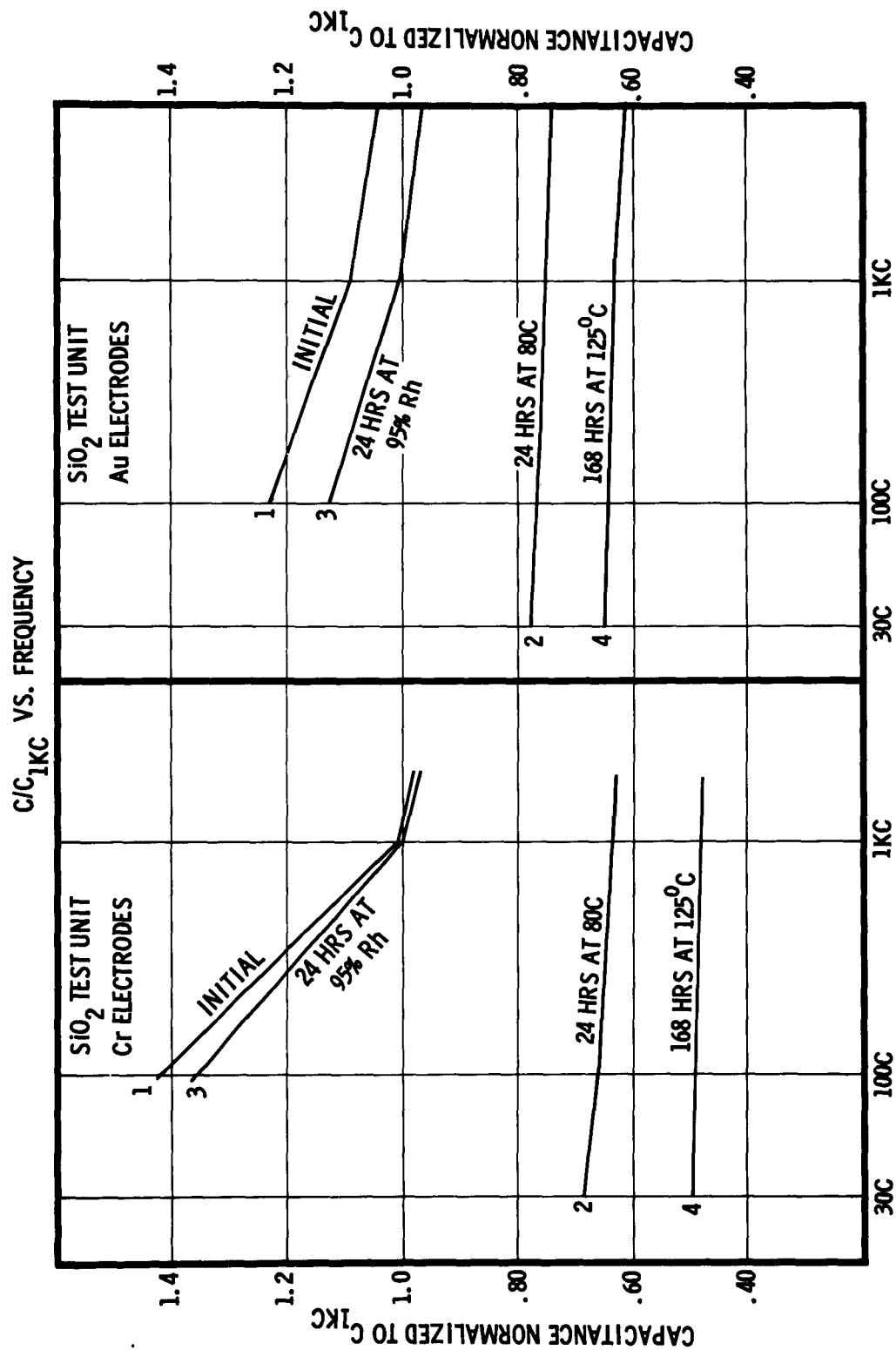


Figure 10. C/C_{1kc} vs Frequency for Stressed SiO₂ Test Units

silicon monoxide films, aging at high relative humidity has a very marked effect on the characteristics of these capacitors. It can be seen from the data (Table III), that high temperature aging decreases the capacitance and tends to level the capacitance versus frequency curves, whereas aging at high humidity produces opposite effects. In addition, the dissipation factor decreases after high temperature aging, and increases after aging at high humidity. Moreover, the effects are more severe on capacitors with chromium electrodes than with gold electrodes, although this conclusion is based on a relatively small sampling of data. The data indicates very strongly that moisture absorption into the dielectric film is probably the most important mechanism of producing relatively large changes in the characteristics of the capacitors.

TABLE III. TYPICAL CHARACTERISTICS OF SILICON DIOXIDE THIN-FILM CAPACITORS								
Dielectric Thickness \approx 3000 Å								
Unit No.	Environmental Stress			Reciprocal Capacitance - Percentage Difference from value at 1 kc after 125 C Environment			Dissipation Factor at 1 kc Per Cent	Electrodes
	Relative Humidity %	Temp. °C	Duration Hours	freq = 100 cps Per Cent	1 kc Per Cent	100 kc Per Cent		
Initial								
4-12				+85.3	+63.8	+49.1	5.83	Au
5-11				+190.3	+102.2	+71.1	+12.4	Cr
5-12				+191.4	+103.8	+75.3	11.8	Cr
24 hours at 80 C								
4-12		80	24	+25.3	+22.0	+16.0	1.83	
5-11		80	24	+49.8	+41.2	+28.1	4.0	
5-12		80	24	+58.6	+48.3	+34.4	4.2	
95 per cent relative humidity								
4-12	95		24	+102.6	+77.6	+59.7	6.29	
5-11	95		24	+184.9	+103.5	+70.7	12.5	
5-12	95		24	+178.9	+104.7	+75.2	11.19	
125 C								
4-12		125	24	+ 1.7	0	-2.45	0.94	
5-11		125	48	+ 2.9	0	-4.6	1.85	
5-12		125	48	+ 3.7	0		2.0	
95 per cent relative humidity								
4-12								
5-11	95		24	+106.7	+76.9	+56.0	7.4	
5-12	95		24	+107.9	+79.3	+59.2	7.3	

4.1.2.4.4 Aluminosilicate Test Units. During previous report periods, vapor-deposited aluminosilicate glass-dielectric test units with aluminum, gold, chromium and copper electrodes were prepared and put under test. The units range in thickness from 3000 to 6000 angstroms and have 200 to 1000 $\mu\mu\text{f}$ capacitance values at 1 kc. Dissipation factors of aluminum, chromium and gold units are less than 1 per cent at 1 kc while the copper units are close to 2 per cent. The highest dc leakage currents are associated with the gold units. Figure 11 is a typical plot of the capacitance and dissipation factor as a function of frequency for typical test units. The chromium units exhibit the expected high dissipation factor at higher frequency due to their high series resistance. In the case illustrated, the effect is exaggerated by unusually thin chromium electrodes. The relatively large positive slope for the copper units is the result of an observed reaction between the copper electrode and the dielectric during the deposition of the dielectric. Meager data on the electrical properties of these units under stress was obtained; however, the investigation was terminated in light of the following work.

Recently, the vapor deposition techniques have been improved and aluminosilicate dielectric capacitors have been fabricated which show dissipation factors of less than 1 per cent over the frequency range of 100 cps to 300 kc, a capacitance of more than 1000 $\mu\mu\text{f}/\text{min}^2$, and a time constant of open circuit voltage decay in excess of 1000 seconds. Breakdown voltages in excess of 150 volts for a capacitance of 100 picofarads per mm^2 have been measured. An effective dielectric constant of 6-7, dielectric strengths from 6×10^6 to 4×10^7 volts/cm, and volume resistivity of 10^{16} ohm cm have been measured.

Accelerated aging of these capacitors are currently in process. A group of 21 units have been aged at 125 C and under a 22V dc load for an accumulated time of 31,500 hours, giving a mean time to failure of 10,500 hours. The over-all change in capacitance with aging is -2 per cent average, with a minimum of -1.2 per cent and a maximum of 3.4 per cent at the end of 1500 hours.

Exploratory work on these latter systems was initiated during the last quarter. Two types of electrode interfaces were evaluated in the following manner. Substrates of glazed alumina were covered with freshly evaporated films of aluminum and gold.

Since the expansion of the evaporated films are constrained by that of the substrate, and the internal stresses of the films are presumably constant for a given set of deposition parameters, the maximum film thickness obtainable before rupture of the deposit occurs should be an indication of the forces of adhesion to the two types of substrate surface. It was found that under identical conditions of deposition, the aluminosilicate film thickness was limited to approximately 6000 angstroms on the gold electroded substrate while thicknesses of greater than 20,000 angstroms were successfully deposited upon the aluminum electroded substrate with no evidence of crazing or spalling in the deposited film.

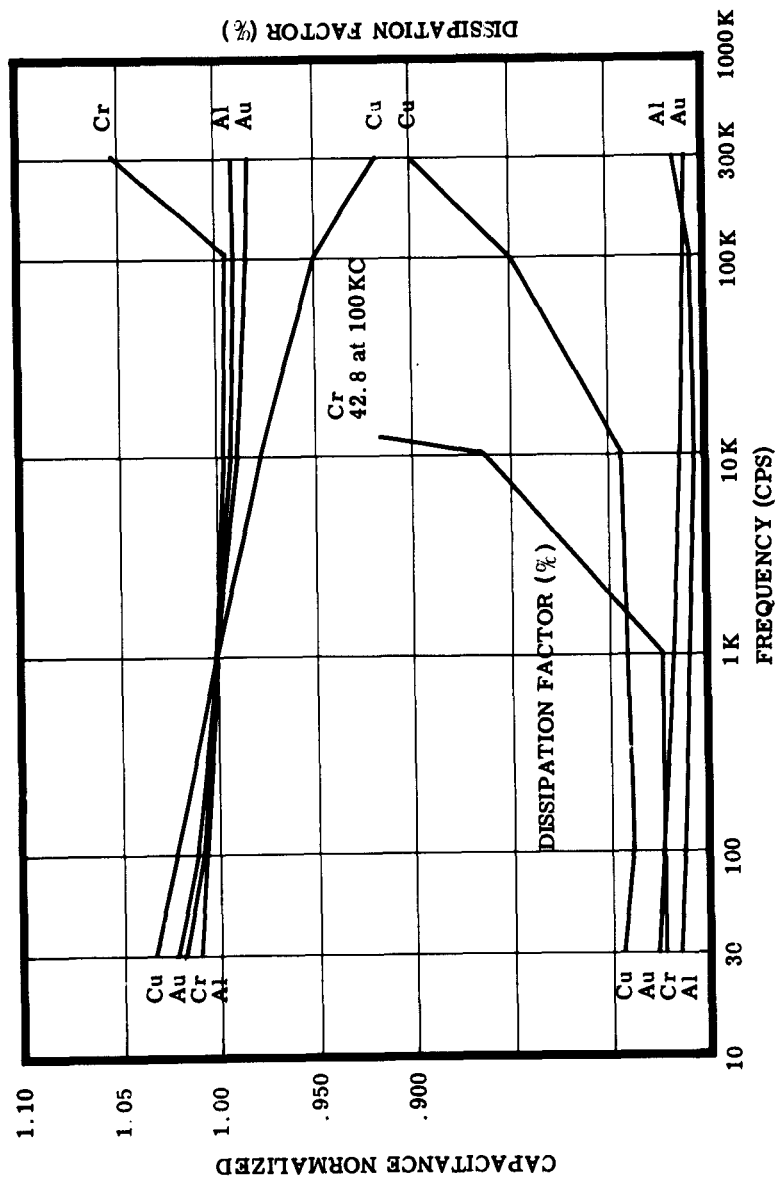


Figure 11. C/C_{1kc} and DF vs Frequency for $\text{Al}_2\text{O}_3 \cdot \text{SiO}_2$ Test Units

This phenomena is attributed to the formation of chemical bonding between the vapor-plated aluminosilicate film and the highly adherent oxide normally present on the aluminum surface. The inert nature of gold largely precludes the formation of true chemical bonding of the deposited film to this metal. Adhesion would then be dependent largely upon Van der Waals' or electrostatic forces which, of course, are considerably weaker. That type of substrate surface largely determines the adhesion of the deposited film. This is shown by an experiment using substrates which have different expansion rates but which have an oxide surface layer.

The frequency dispersion of the capacitance and dissipation factor of electroded units is illustrated in Figure 12 for a typical unit. As with other thin-film capacitors, the decrease in capacitance and dissipation factor at low frequencies, i.e., below 100 cps, is indicative of possible interfacial polarization mechanisms. However, the effect is much less pronounced in these units than in other glass-like dielectric units.

Further evidence of the effect of interfacial properties on the electrical properties of the capacitors is indicated by the frequency and thickness dependency of the temperature coefficient of capacitance (TCC). Measurements of TCC were obtained by use of the General Radio Capacitance bridge, General Radio guard circuit, and a suitable controlled heating arrangement. Measurements were made at 30 cps, 100 cps, 1 kc, 10 kc, 100 kc and 300 kc in the temperature range 25 C to 150 C. Figure 13 gives the frequency dependence of the temperature coefficient of capacitance and dissipation factor. It is seen that both temperature range and frequency must be specified for the term TCC to be fully defined. Again the increased frequency dependence is noted in the lower frequency range. It was further found that there was a correlation between the thickness of the dielectric film and the temperature coefficient of capacitance. Figure 14 is a plot of TCC at 1 kc in the range 25 to 150 C versus dielectric thickness. It seems likely that the increasing contribution of interfacial effects to the capacitance of the thinner films may be responsible for the large increase in TCC in thinner dielectrics.

Preliminary investigations were undertaken to determine whether leakage current-applied voltage measurements would be of value in the failure mechanism study. The leakage current characteristics of several aluminum and gold electroded aluminosilicate capacitors were measured in a dry argon atmosphere over a voltage range of 1 to 100 volts. Measurements were taken at steady state conditions to negate the contribution from the charging current. Figures 15 through 18 illustrate typical curves recorded. The curves are plotted on log-log axis and semilog axis to reveal functionality characteristics.

Figure 15 illustrates the characteristics of gold electroded units after 24-hour storage in dry argon. Approximate ohmic behavior, $I \propto V^{1.2}$, is observed below 10 volts on the log-log plot and exponential behavior $I \propto e^{0.03V}$, above 10 volts on the semilog plot. Figure 16 is a comparable plot for an aluminum electroded unit after 24-hour storage in argon. An exponential relationship ($I \propto e^{0.008V}$) is observed above about 40 volts and a nearly ohmic behavior ($I \propto V^{1.3}$) below 40 volts. Figure 17 is a plot for an aluminum electroded unit stored for 96 hours in argon prior to measurement. This unit exhibits nearly ohmic behavior ($I \propto V^{1.3}$) below about 40 volts and saturation above 40 volts.

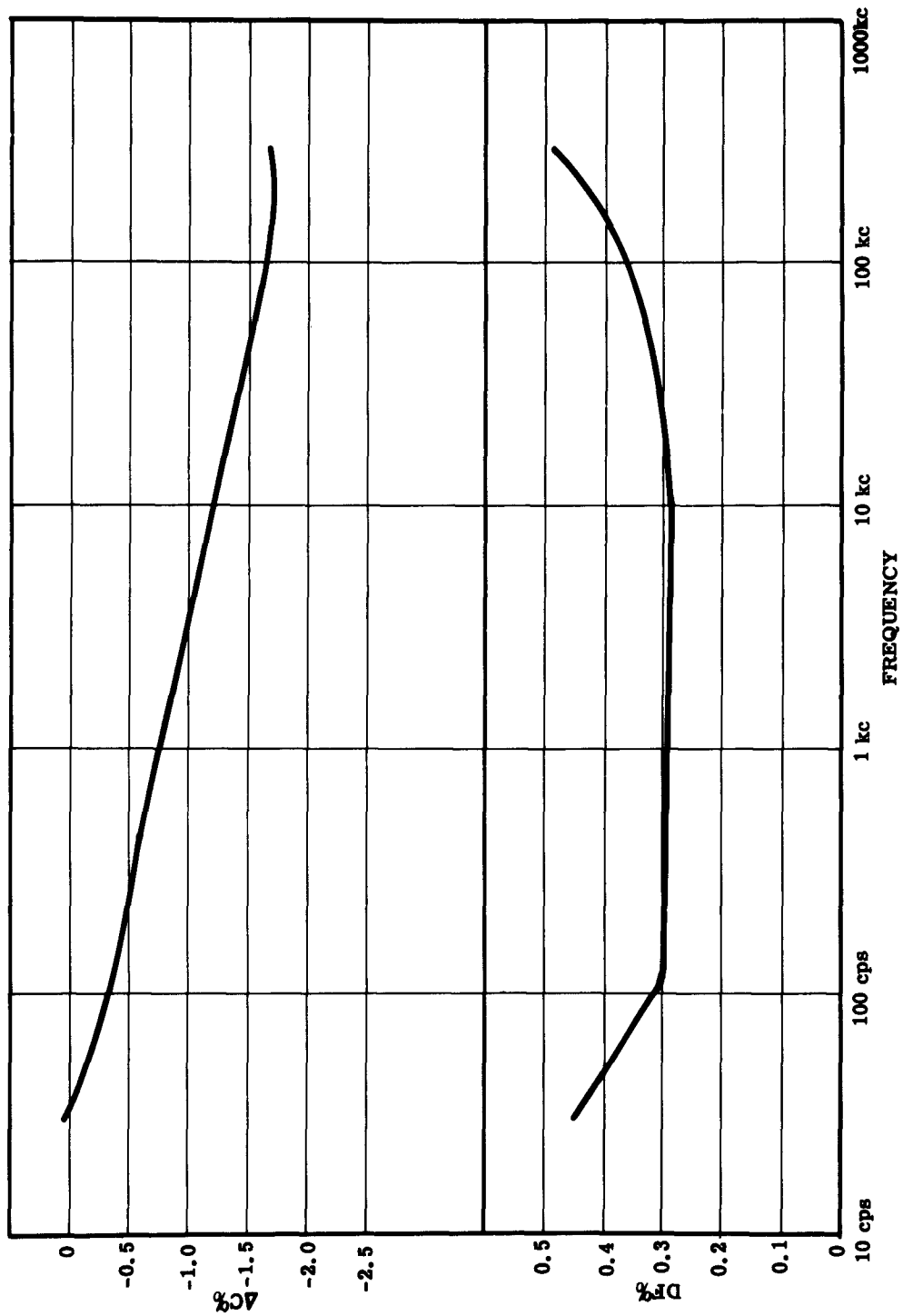


Figure 12. C and DF vs Frequency of Improved $\text{Al}_2\text{O}_3 \cdot \text{SiO}_2$ Test Units

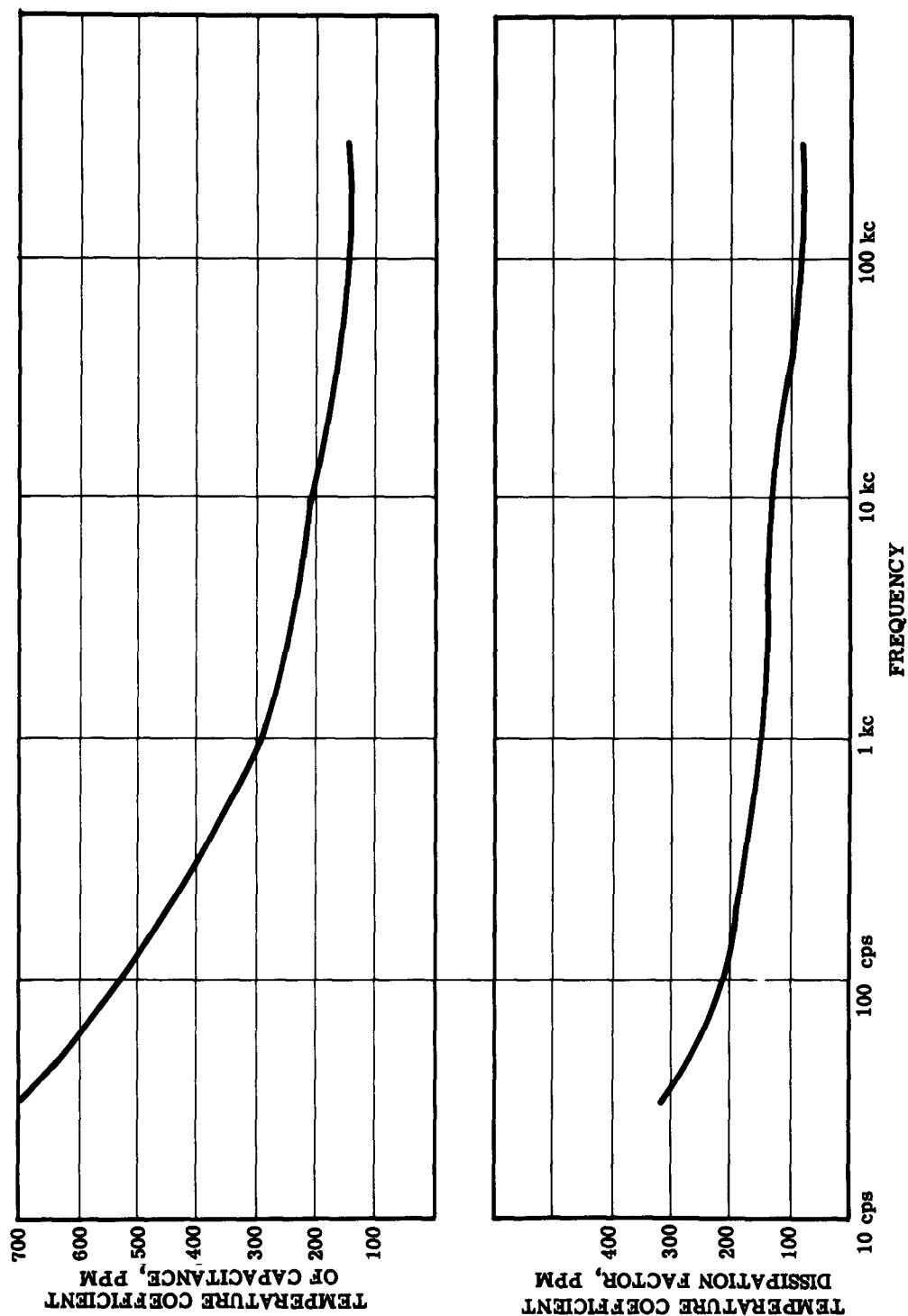


Figure 13. Temperature Coefficient of Capacitance and Dissipation Factor vs Frequency for Improved $\text{SiO}_2 \cdot \text{Al}_2\text{O}_3$ Test Units

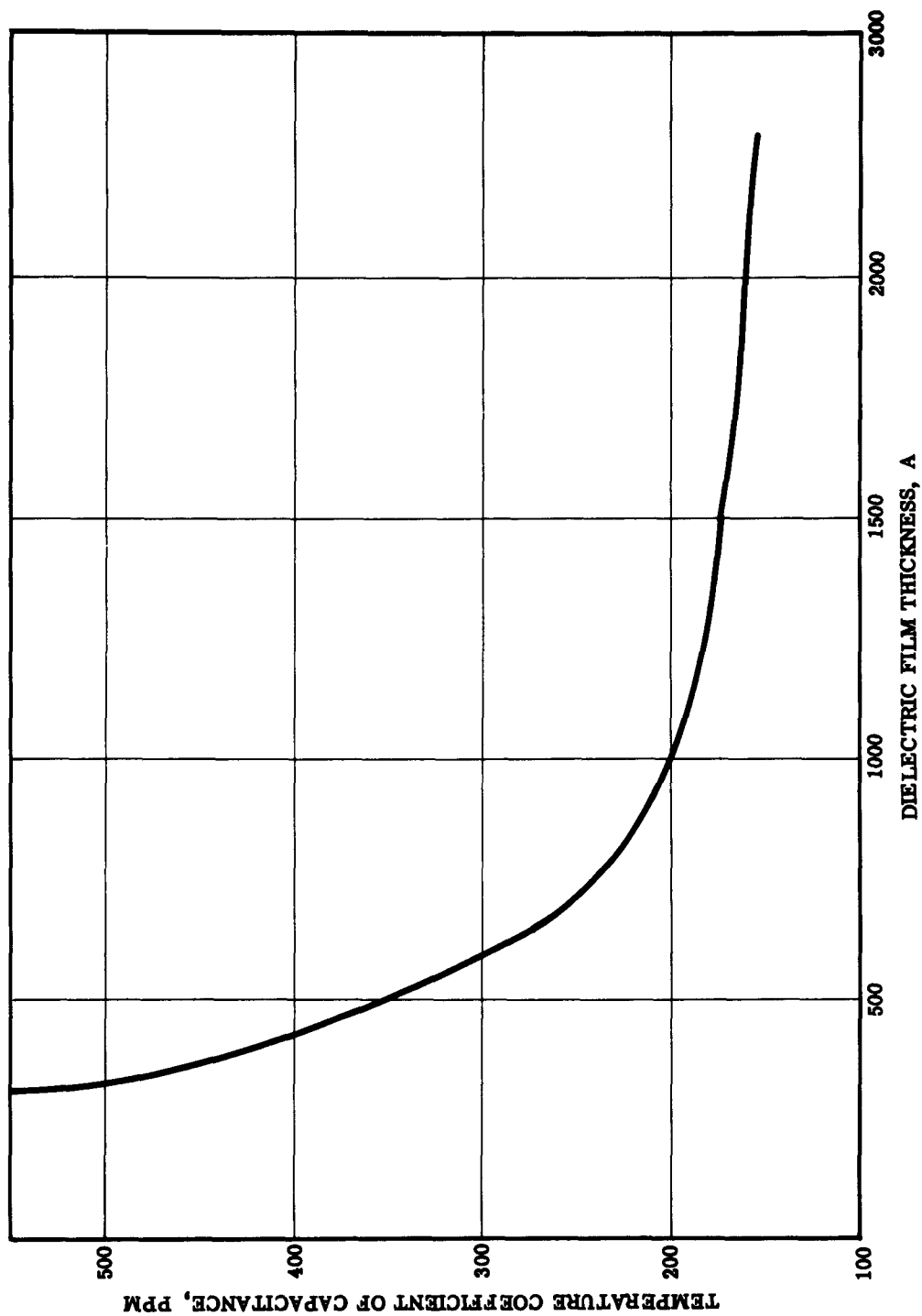


Figure 14. Temperature Coefficient of Capacitance vs Film Thickness for Improved $\text{Al}_2\text{O}_3 \cdot \text{SiO}_2$ Test Unit

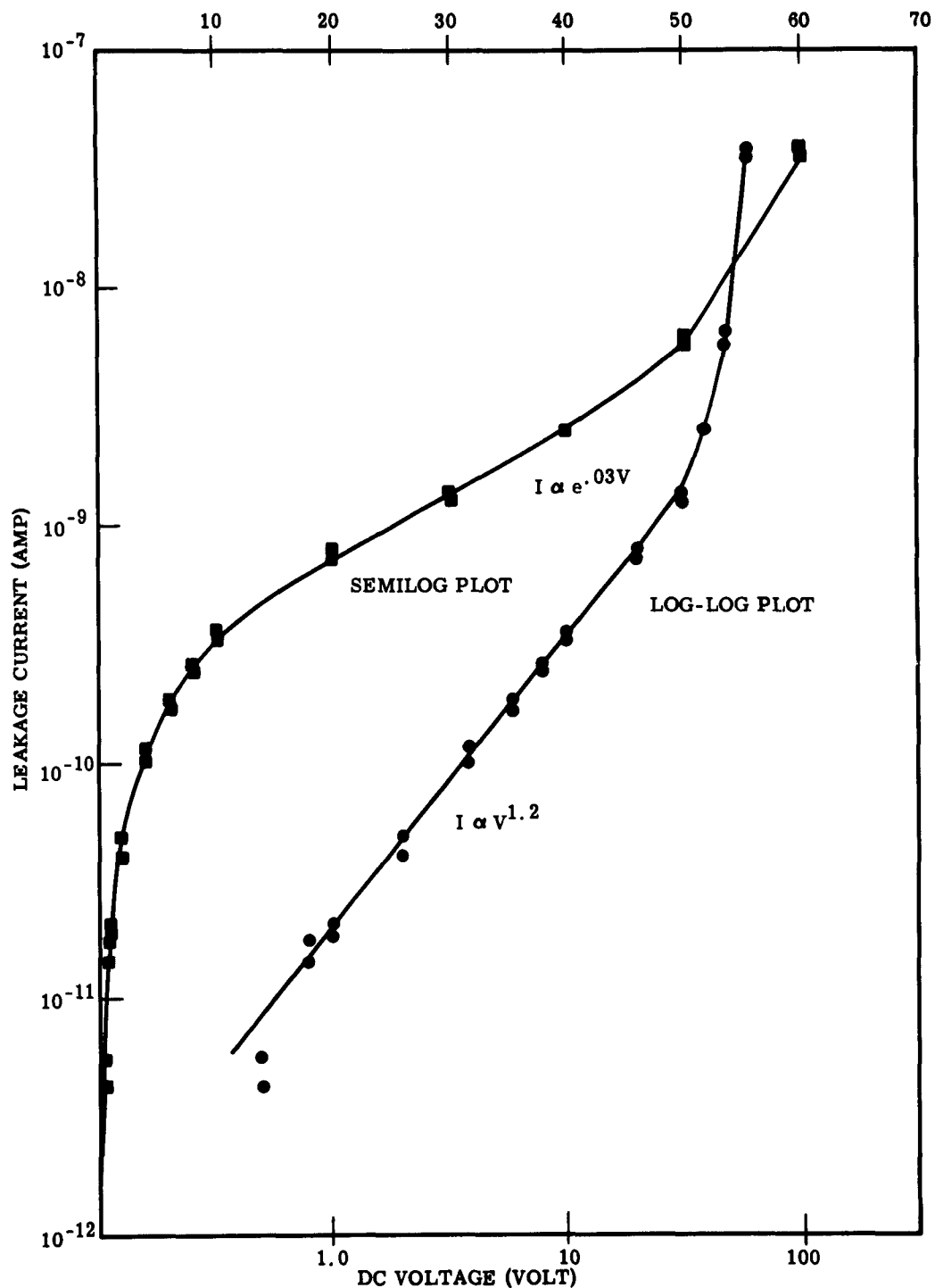


Figure 15. Gold Electroded Aluminosilicate Test Unit (24 hr storage in argon)

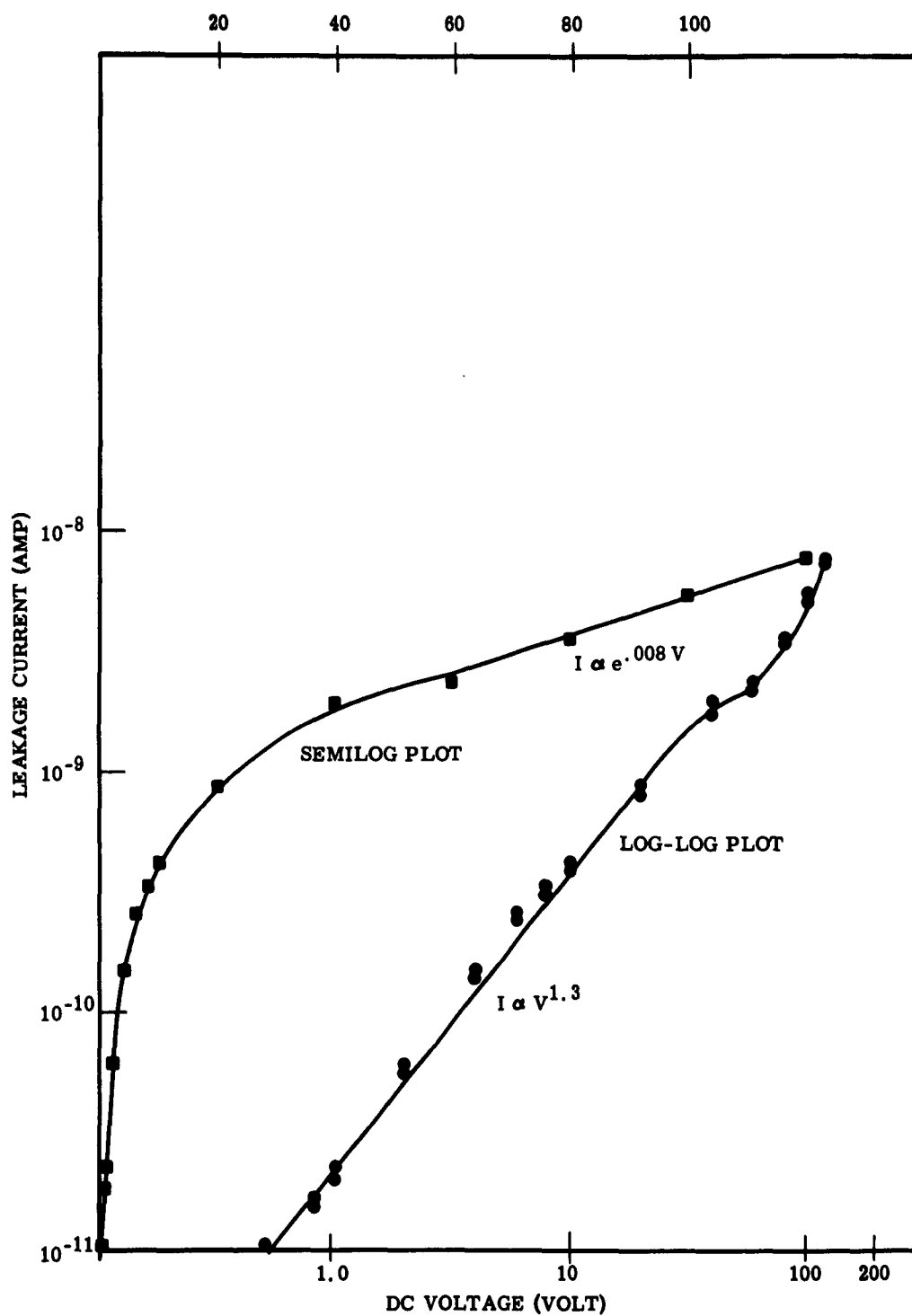


Figure 16. Aluminum Electroded Aluminosilicate Test Unit
(24 hr storage in argon)

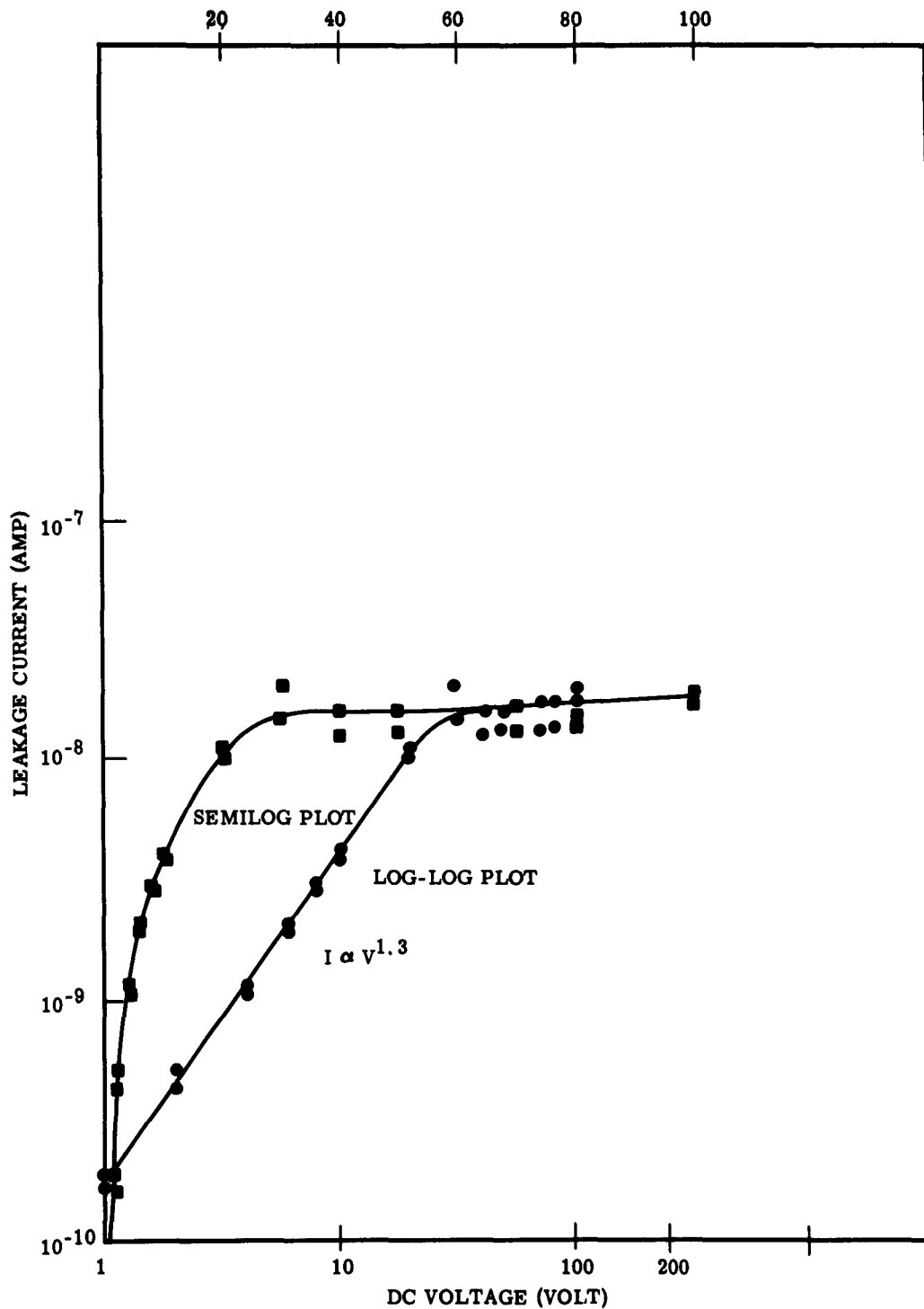


Figure 17. Aluminum Electroded Aluminosilicate Test Unit
(96 hrs storage in argon)

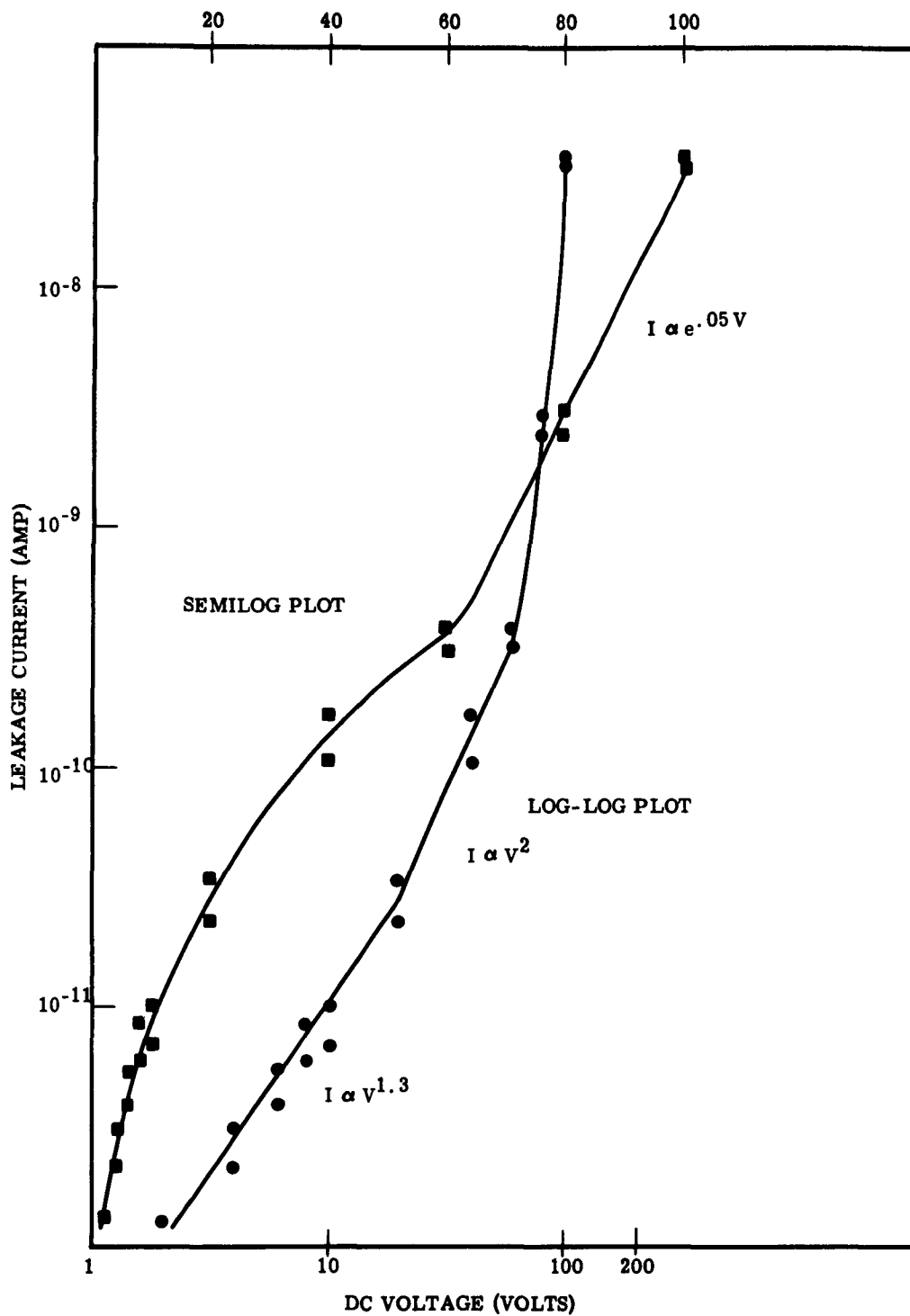


Figure 18. Aluminum Electroded Aluminosilicate Test Unit (After 125 C Bake)

Figure 18 shows the plot of an aluminum electroded unit which was baked at 125°C prior to measurement. This unit exhibits exponential dependency ($I \propto e^{0.05V}$) above 60 volts and nearly ohmic behavior ($I \propto V^{1.3}$) below about 20 volts.

Other work has indicated that the exponential dependency of I on V is indicative of space-charge-limited, distributed-trap limited currents^{1,2,3,4}. True space charge limited current would show a square law voltage dependency.

No specific conclusions are drawn from the data at this time but two general conclusions are evident:

- (1) trap-limited, space-charge limited currents are observed in aluminosilicate films, and
- (2) thermal stress and the nature of the electrode material alter the V - I characteristics of the aluminosilicate films.

This type of measurement may serve as an analytical tool in understanding the electrical properties of dielectrics. The importance of the space-charge forces in the study of the electrical properties of the dielectric-metal film interface are summarized as follows:

1. Insulators normally have a relatively low density of free carriers; consequently, charge unbalance is easily produced by electrical fields.
2. Very large effects can be produced through the use of ohmic contacts which facilitate the direct injection of excess charge into the insulator.
3. The character and magnitude of these effects is due largely to the presence of localized states which can trap and store charge in an equilibrium with the free mobile charge.
4. The study of SCL currents can yield such information as the mobility of free charge carriers, and the density, location-in-energy, and capture cross sections of the trapping sites.

The mathematical formulation of steady state SCL currents reported by Rose¹ and Lampert² along with the mathematical formulation of the transient SCL currents reported by Mark and Helfrich³ make possible qualitative and quantitative analysis of the electrical properties of thin insulating materials.

Since it is possible to mathematically formulate the relationships between current and voltage as a function of various trapping distributions, and since the energy distribution of traps determines the form and magnitude of the SCL current voltage curves, it is reasonable to assume that one could work backwards from an experimentally determined current-voltage curve to obtain the mobility of the free charge carriers, and the density, location-in-energy, and capture cross section of the trapping sites. Examples of this form of analysis are given in the literature⁴.

¹Superscripts refer to similarly numbered entries in the List of References.

4.1.2.5 Conclusions

The results of the efforts directed toward the understanding of the dielectric metal interface are quite encouraging thus far. Data are being obtained which are quite reproducible and consistent, although interpretation thereof is by no means an easy one.

A number of models can be hypothesized to explain the behavior of the frequency dispersion curves but it is impossible to state conclusively at this time which of these models is correct. It is believed that the most important product of this program will be a body of information which can be used with other experimental data in arriving at a true picture of the dielectric-metal interface.

4.2 DIFFUSION STUDIES ON THE TANTALUM-TANTALUM OXIDE SYSTEM

4.2.1 Background

Diffusion across a material interface has generally been accepted as a primary failure mechanism of solid state devices. The thin-film tantalum capacitor formed by electrolytic anodization of a tantalum film exhibits a diffusion controlled gradient of tantalum atoms across the metal interface and through the oxide layer. It is reasonable to suppose that this gradient could be altered by the subsequent application of thermal and/or electrical stress to these units. Radioactive isotopes provide a sensitive and accurate method for studying this type of diffusion phenomena. Such a technique was used to determine whether irreversible migration of tantalum atoms might occur when a tantalum-tantalum oxide thin-film capacitor is stressed under certain conditions. By fabricating the capacitor units from anodized radioactive tantalum and subsequently etching off the tantalum oxide in small incremental thicknesses and measuring the radioactivity at each step, an activity profile of the unit may be obtained. By comparing the profile of a stressed unit with that of an unstressed unit, any differences resulting from the migration of tantalum atoms across the interface or through the oxide may be correlated with stress conditions and electrical measurements.

4.2.2 Experimental Procedure

4.2.2.1 Fabrication of Models

The fabrication of the test units, including a diagram of a completed test unit, can be found in the Third Quarterly Report. Ten tantalum films, each 2000 Å thick, evaporated onto individual 0.375 x 0.250-inch fused-quartz substrates, were sent to the Atomic Energy Commission's Oak Ridge National Laboratories for neutron irradiation. The films were then anodized at a forming voltage of 82 volts, yielding tantalum oxide films approximately 1600 Å thick. Chrome-gold solder tabs and gold electrodes were evaporated onto eight of these films to complete the test units. The other two films were used as standards.

4.2.2.2 Stressing Conditions

Of the eight complete units, four were shorted (see Third Quarterly Report for dc leakage measurements). The four good units were put under thermal and electrical stress, two of the shorted units were placed under thermal stress only, and the remaining two units were unstressed. Table IV shows the stressing conditions.

TABLE IV. RADIOACTIVE TANTALUM-TANTALUM OXIDE UNITS, STRESS CONDITIONS	
SAMPLE NO.	
1	None-control (no top electrode)
6	None-control (no top electrode)
2	None-control (with electrode)
8	None-control (with electrode)
4	125 C, 22-1/2 V dc, 2 hrs
5	125 C, 22-1/2 V dc, 2 hrs, plus 70 C, 45 V dc, 1 wk
3	125 C, 2 wks
9	125 C, 22-1/2 V dc, 2 wks
10	125 C, 2 wks, plus 70 C, 4 wks
7	125 C, 22-1/2 V dc, 2 wks plus 70 C, 22-1/2 V dc, 4 wks

The stress conditions used in this preliminary investigation are similar to the environmental stress levels currently being used in the evaluation of tantalum-tantalum oxide capacitors. The multiplicity of stress conditions for some samples arose because of the necessity for covering as wide a range of conditions as possible with the limited number of samples available.

4.2.2.3 Electrical Measurements

Capacitance and dissipation factor measurements at 1 kc of the four good units were made before and after stressing.

4.2.2.4 Thickness Measurements

To obtain a usable activity profile, the tantalum oxide thickness must be determined accurately and nondestructively after each etching. The oxide thickness was determined from the wavelength of minimum reflectivity measured by means of a specially constructed reflectance attachment made to fit a Beckman Model B spectrophotometer (see Second Quarterly Report). For a non-absorbing oxide, the following relationship applies:

$$(D+X) = \left(\frac{2r-1}{2}\right) \left(\frac{\lambda}{2n \cos \theta_1}\right) \quad (5)$$

where

- D = thickness
- X = constant which allows for reflection phase changes
- r = 1, 2, 3, etc. denoting orders of interference
- λ = wavelength of minimum reflection
- n = refractive index of oxide at wavelength λ
- θ_1 = angle of refraction

$$(\sin \theta_1 = \frac{\sin \theta_0}{n} \text{ where } \theta_0 = \text{angle of incidence})$$

The refractive index is calculated at various wavelengths using the formula derived by Young⁵:

$$n = 2.14 + 0.292/(\lambda/10^3 \text{ A} - 2.305)^{1.2} \quad (6)$$

Interference occurs between the light reflected from the nonabsorbing oxide with a phase change of 180 degrees and light which is reflected from the metal with an unknown phase change. This gives rise to the constant X in Equation (5). The difference between the two phase changes results in calculated thickness which is greater than the actual oxide thickness. The error is of the order of 100 to 200 A. The error in thickness could be calculated from a knowledge of the optical constants of the metal if they were accurately known. However, this information is not available for thin films of the metal, so the constant is best found by experimental methods.

The experimental method used to find the constant X involves the measurement of the tantalum oxide thickness by means of multiple-beam interferometry on a separate, though comparable, sample. This work is described elsewhere in the Final Report on Failure Mechanisms. Spectral reflectance measurements on the sample gave an oxide thickness of 1903 A. The interferometry measurements yielded an oxide thickness of 1747 A. Therefore, the value of X is 156 A.

4.2.2.5 Etching and Counting

The gold electrodes were dissolved in a 20-per cent potassium cyanide solution (which does not affect the tantalum oxide) and the solution was counted to show that no radioactive tantalum had diffused into the gold. The tantalum oxide was etched using an 80-per cent solution of concentrated hydrofluoric acid. After each etching, the remaining radioactivity of the sample was counted and the remaining oxide thickness measured. Details of this procedure may be found in the Third Quarterly Report.

4.2.3 Mathematical Treatment of Data

4.2.3.1 Correction of Radioactivity Measurements for Instrument Drift and Natural Decay

To accurately compare results from different samples, all radioactivity measurements must be corrected for any instrumentation drift. The drift was evident by changes in activity levels with time which could not be accounted for by natural decay. Accordingly, the standard, sample #1, was counted just prior to each radioactive count on the other samples and the appropriate correction factor applied.

Artificial radioisotopes obey the natural decay law:

$$I = I_0 e^{-\lambda t} \quad (7)$$

where:

- I = intensity of radioactivity
- I_0 = initial value at 0 time
- t = any time
- $\lambda = 0.693/T$ where T = half-life
(T for Ta 182 is 112 days)

Accordingly, the cpm of the samples should vary with time according to Equation (7). Therefore, after making necessary corrections for instrument drift, the cpm values of the samples were corrected for natural decay according to Equation (7).

4.2.3.2 Determination of the Activity of the Remaining Tantalum

The high radioactivity of the remaining tantalum metal tends to mask small changes in the activity of the tantalum oxide increments. Therefore, the cpm of the tantalum metal must be subtracted from the total cpm of the sample. To calculate the cpm of the remaining metal film, two things must be determined; (1) the thickness of the tantalum metal, and (2) the cpm/atom of the metal.

When a tantalum film is anodized, the total thickness of the tantalum-tantalum oxide is less than the combined thicknesses of the original tantalum metal and the tantalum oxide. This difference must be determined indirectly. The method used was, again, multiple-beam interferometry, and details of this determination may be found in Paragraph 4.3. It was found that 992 Å of the original metal film was used in forming 1747 Å of the oxide. Assuming that this ratio is constant for small differences in oxide thickness (approximately 100 Å in this case), a simple proportion was used to calculate the remaining tantalum thickness on the radioactive samples.

The cpm/atom of tantalum was calculated by dividing the total cpm of the sample by the number of atoms in the original tantalum film. The number of atoms was determined by the relationship

$$N = \frac{V X d}{A} \times 6.02 \times 10^{23} \quad (8)$$

where

N = no. of atoms

V = volume of film in cc

d = density of Ta (in this case, the bulk density of 16.6 g/cc)

A = atomic weight of Ta

To determine the cpm due to the remaining tantalum metal film, the number of atoms in this film is also calculated using Equation (8). By dividing this number by the corresponding cpm/atom, that part of the activity due to the remaining metal may be calculated.

4.2.3.3 Determination of Etch Rates

The average etch rate of the tantalum oxide may be determined by plotting thickness versus etch time. Such a plot is shown in Figure 19. There are no thickness measurements between the region of 500-1000 Å. This region includes the colorless area between the first and second-order interference colors, where no measurements could be taken, and the blue first-order color, where the minimum reflectance dip was so broad that the accuracy was questionable.

Figure 19 is representative of the etch rate curves for all the samples except #5. The etch rate for this sample is shown in Figure 20. Etching of this sample was stopped when it was noticed that the etching was becoming very uneven over the surface of the oxide. This sample will be discussed in detail in the paragraph on interpretation of data.

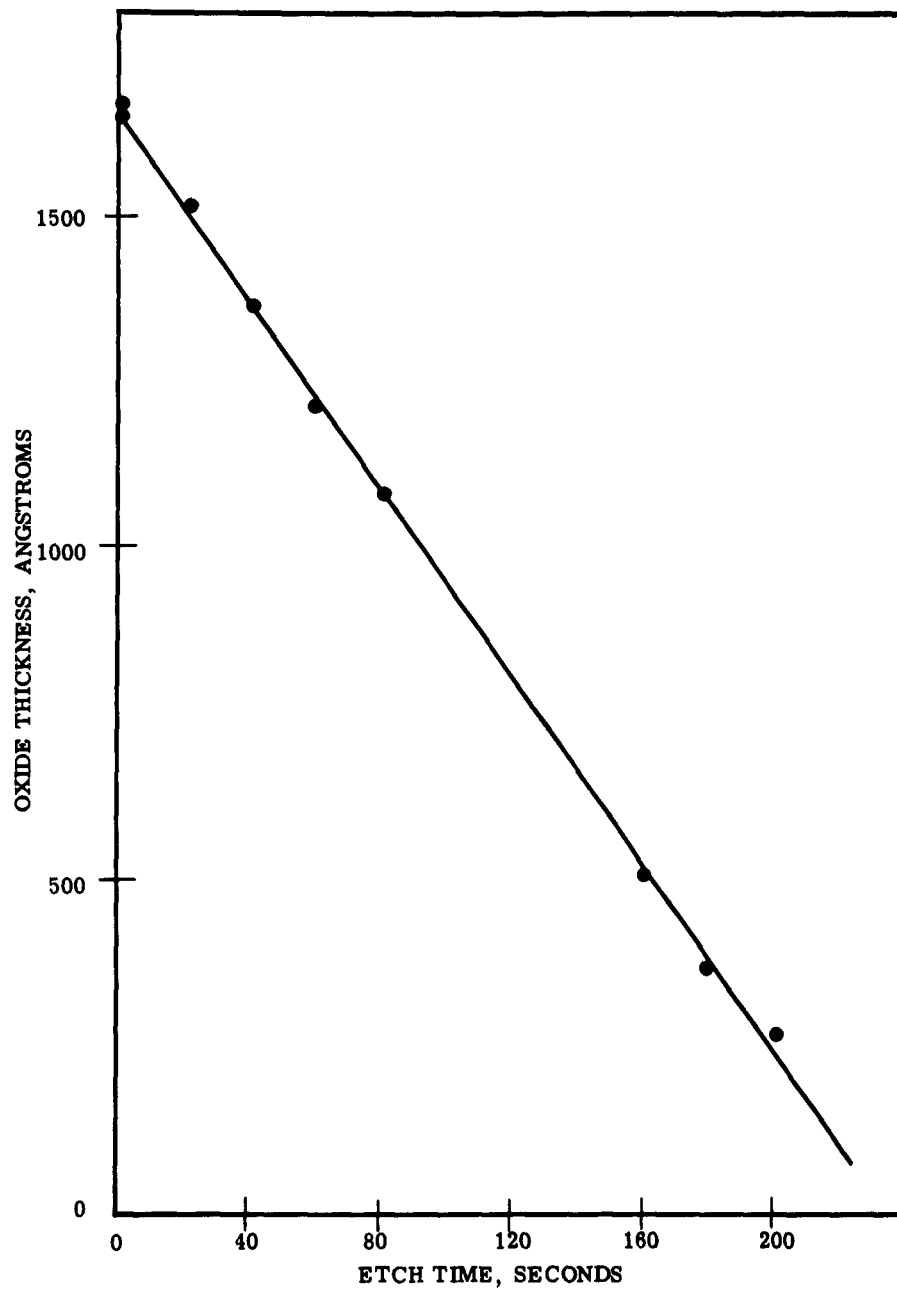


Figure 19. Etch Rate of Tantalum Oxide Film (Sample No. 10)

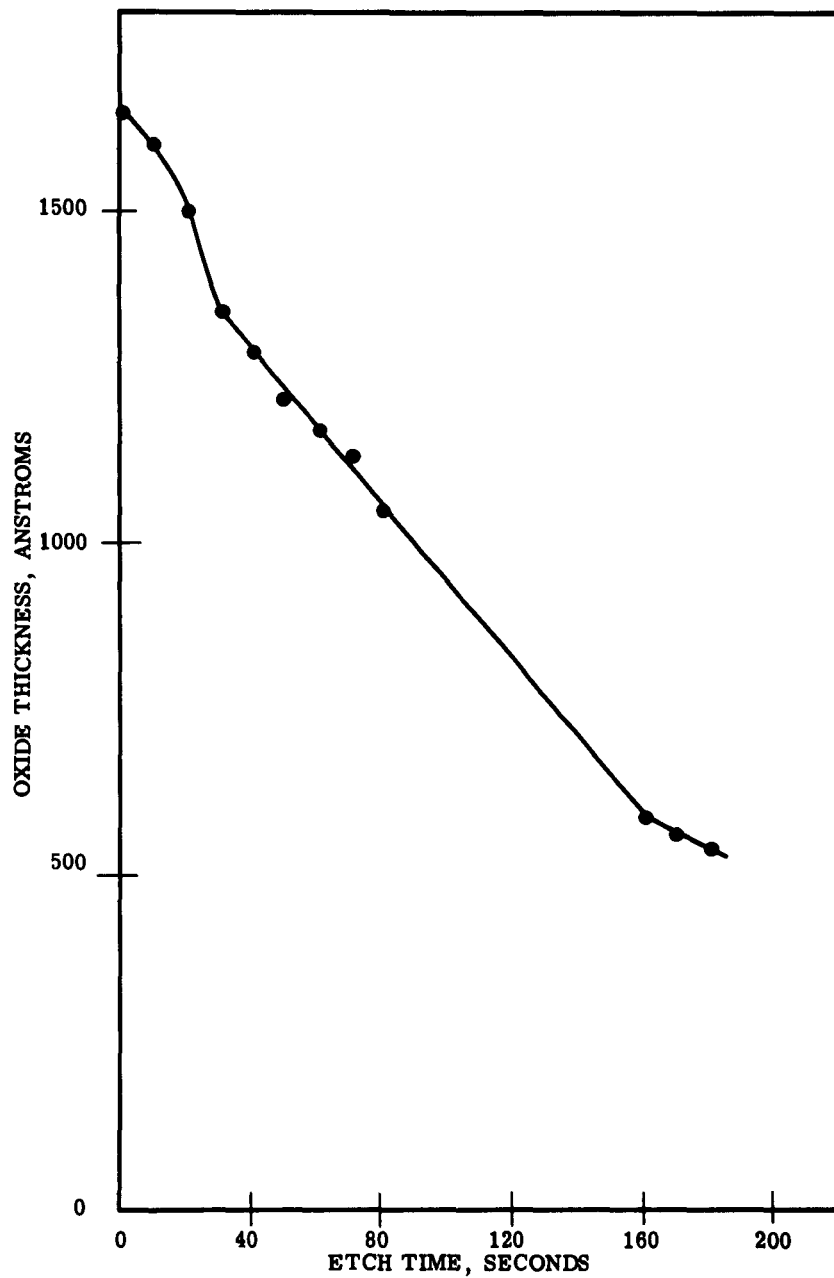


Figure 20. Etch Rate of Tantalum Oxide Film (Sample No. 5)

4.2.3.4 Correlation of cpm and Thickness

Figure 21 shows a plot of the cpm versus thickness for sample #10. Both the actual measured thicknesses and thicknesses taken from the etch rate curve are plotted. The horizontal line at 42,700 cpm denotes the radioactivity of the remaining tantalum metal. The curve crosses this base line well within the absolute accuracy of the interface determination as discussed in Paragraph 4.3. This agreement justifies the use of the assumption that the ratio of "tantalum used" to "oxide formed" is constant. It also justifies the assumption that the difference due to the phase change at the metal surface is constant for all wavelengths.

Only one curve, that of sample #4, failed to cross the base line within the range of experimental error and no reliable data can be obtained from measurements on this sample.

4.2.3.5 Determination of Concentration Profile

The concentration profiles of the samples are determined by plotting the concentration of tantalum atoms in the oxide versus the oxide thickness. The cpm of the tantalum metal remaining is subtracted from the cpm counted after each etching. The concentration of tantalum is calculated for small thickness differences throughout the oxide by Equation (9):

$$C = \frac{\Delta \text{cpm}}{\Delta t \times A \times \text{cpm/atom}} \quad (9)$$

where:

C = no. Ta atoms/cc
cpm = counts-per-minute
t = thickness
A = area

Figure 22 shows a typical concentration profile. The level portion of the curve from the top of the oxide surface to a depth of 900 A indicates that the concentration of tantalum is constant in this region. This region extended down to 600 A in some samples. The concentration of tantalum in this region varied from 2.60 atoms/cc to 2.90 atoms/cc. The profiles will be discussed in detail in Paragraph 4.2.4.

4.2.4 Interpretation of Data

The results of the electrical measurements are shown in Table V.

TABLE V. RADIOACTIVE TANTALUM-TANTALUM OXIDE UNITS CAPACITANCE AND DISSIPATION FACTOR MEASUREMENTS				
SAMPLE NO.	BEFORE STRESS		AFTER STRESS	
	C (1 KC) $\mu\mu\text{f}$	DF % (1 KC)	C (1 KC) $\mu\mu\text{f}$	DF % (1 KC)
4	33,140	6.14	32,920	5.94
5	32,935	5.75	32,860	6.80
7	33,010	4.35	33,200	4.15
9	33,100	4.30	33,190	4.42

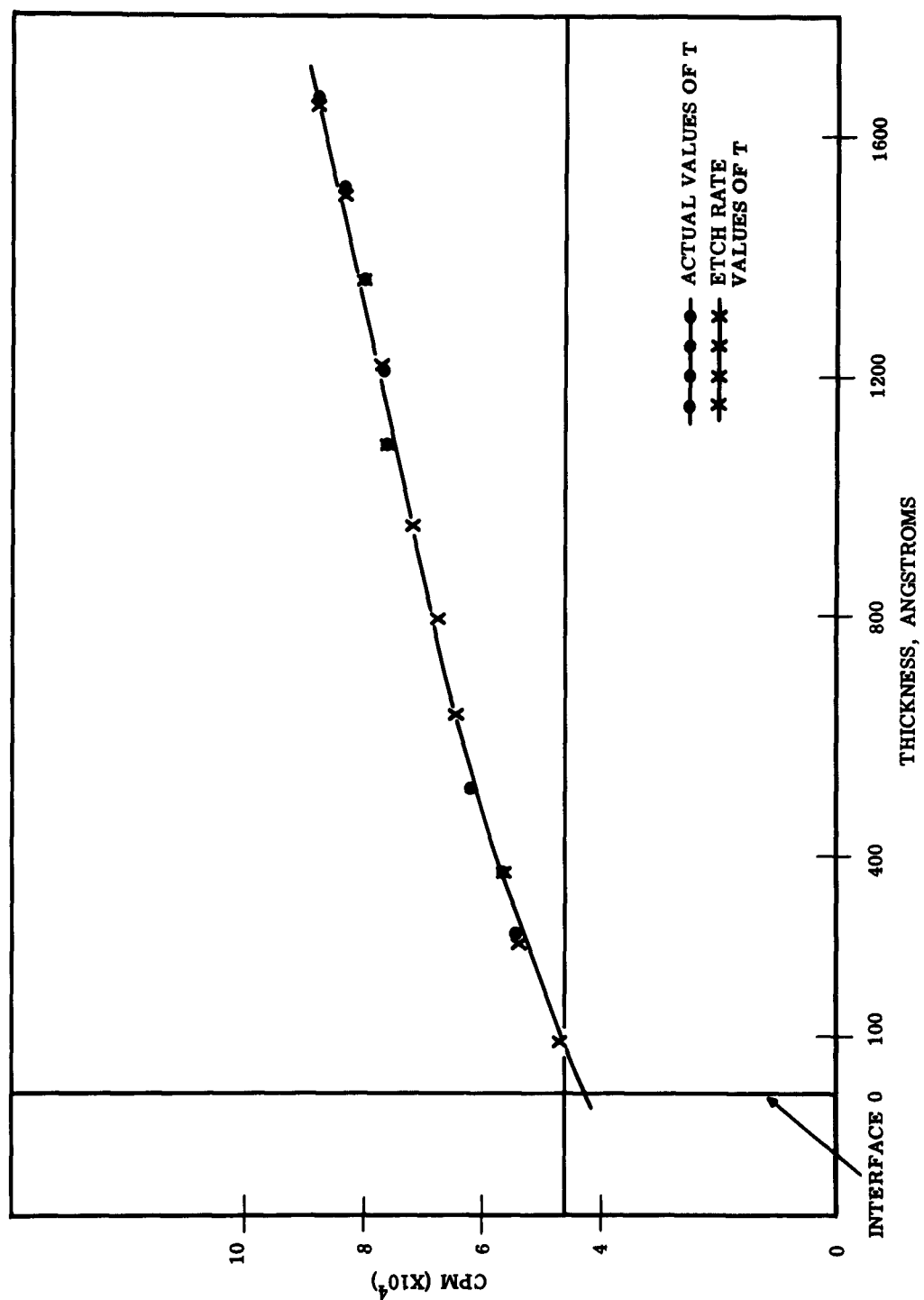


Figure 21. Activity Profile of Radioactive Tantalum Oxide Test Unit.
Counts-per-minute versus oxide thickness (Sample No. 10)

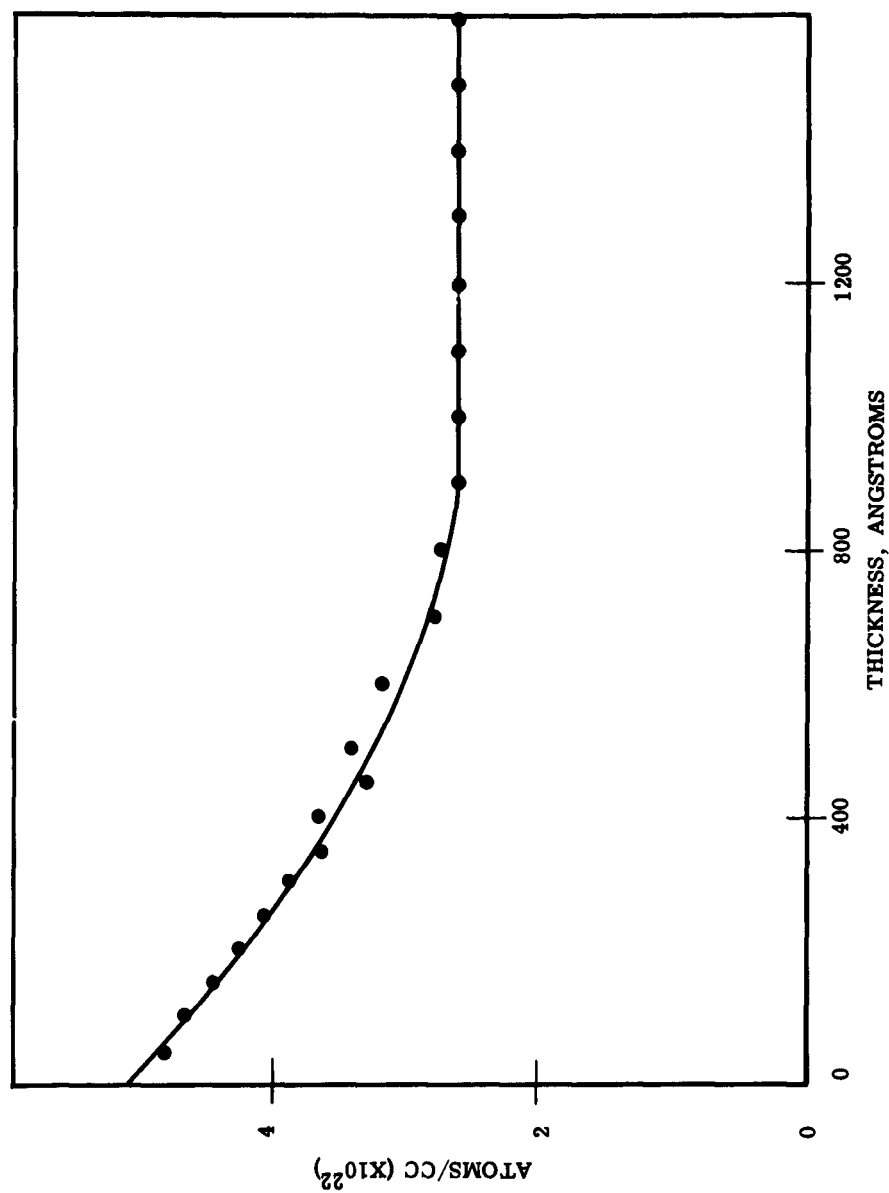


Figure 22. Concentration Profile of Radioactive Tantalum-Oxide Test Unit.
Concentration of Tantalum Atoms versus Oxide Thickness (Sample No. 2)

The only significant change with stress noted is the increase in dissipation factor for sample #5. This increase occurred after the sample had been stressed for one week at 45 V dc double the voltage at which the other units were stressed. The increase in DF appears to be related to voltage induced structural changes in the oxide.

The peculiar etching of sample #5 and the high concentration of tantalum atoms in the oxide film of this sample set it apart from the rest of the samples. Photomicrographs were taken of this sample at high power (see Figure 23). The film is characterized by many small defects which have started to crack from the center outward towards the edges.



Figure 23. Photomicrograph of Radioactive Tantalum Oxide Film (830X) (Sample #5 after etching). Taken with Crossed Nicols.

One large defect in the upper left hand part of the picture shows that part of the film has completely raised up from the surface below it. However, there is still oxide film underneath this raised portion. The configuration of these defects strongly resembles that found by Vermilyea⁶ during the crystallization of anodic tantalum oxide films in the presence of a strong electric field. This film was held at half its forming voltage for one week. Although no definite conclusions can be drawn about any actual crystal formation, there definitely seems to have been some change in the structure of the film.

The Concentration profiles (Figure 22) indicate that there is a constant tantalum concentration from the upper surface of the oxide down to approximately the middle of the oxide layer. This region of constant concentration was found in all the samples and is numerically similar for all samples except for that of sample #5 (see Table VI). The average value of the tantalum concentrations in this region is 2.77×10^{22} atoms/cc, which is somewhat higher than the concentration in bulk crystalline Ta_2O_5 , i.e. 2.38×10^{22} atoms/cc. However, the average calculated density of these tantalum oxide films is higher than the bulk

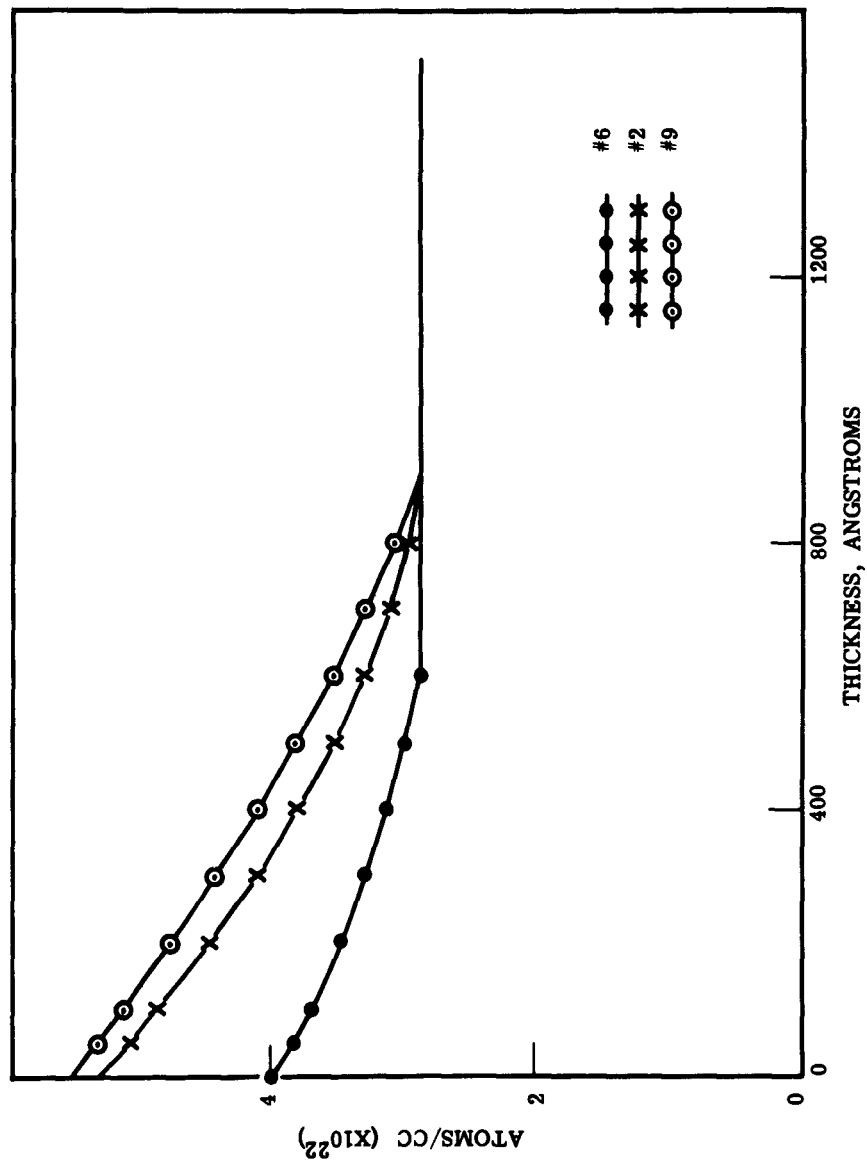


Figure 24. Concentration Profiles of Radioactive Tantalum-Tantalum Oxide Test Units. (Normalized to Equal Concentrations in Constant Portion of Oxide)

value, i.e. 9.43 g/cc, compared with that of 8.8 g/cc for bulk Ta_2O_5 . It seems improbable, therefore, that these films exhibit the Ta_2O_5 stoichiometry or structure.

TABLE VI. CONCENTRATION OF TANTALUM IN THE CONSTANT REGION OF THE ACTIVITY OF PROFILE OF TANTALUM OXIDE. DISTANCE FROM TANTALUM-TANTALUM OXIDE INTERFACE TO REGION OF CONSTANT TANTALUM CONCENTRATION		
SAMPLE NO.	CONCENTRATION OF Ta ATOMS/CC ($\times 10^{22}$)	DISTANCE A
2	2.61 ± 0.3	900
3	2.86	650
5	3.17	--
6	2.91	600
7	2.84	800
9	2.80	950
10	2.59	850

The extent, i.e., thickness, of the region of constant tantalum concentration in the activity profile varies between samples. The distance from the tantalum-tantalum oxide interface at which these regions begin is found in Table VI. It is interesting to note that even in sample #6, which is the unstressed oxide film as-anodized, there is a concentration gradient extending out from the tantalum-tantalum oxide interface to an oxide thickness of 600A. The extent of the gradient region is modified by the application of stress and by the process of evaporating gold electrodes on units which undergo no further stress (sample #2). This modification in extent of gradient is accompanied by a modification in the slope of the gradient (see Figure 24). The gradient of sample #9 is likewise modified by the application of thermal and electrical stress, which in turn modifies the extent of the region of constant tantalum concentration.

To characterize and compare the effects of applied stress on the various units, the data was normalized and the original gradient subtracted out. This process will be clarified by examining Figure 25. By assuming the gradients were caused by diffusion processes, the

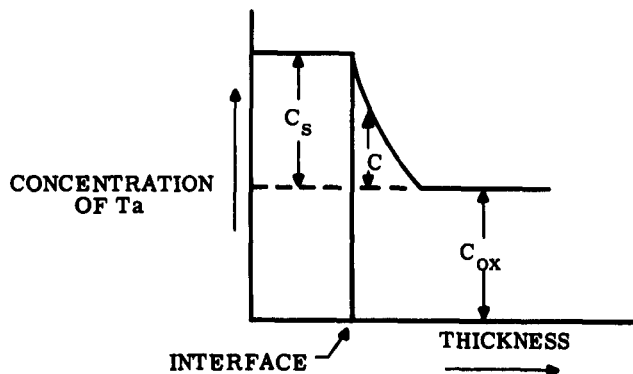


Figure 25. Schematic Diagram of Tantalum Concentration in Radioactive Tantalum-Tantalum Oxide Test Units

concentrations of interest are those of the excess concentration of tantalum in the oxide (C), and the constant source concentration (C_g). Assuming that the tantalum metal film has the same density as that of the bulk metal, the concentration of tantalum atoms in the metal film was calculated to be 5.50×10^{22} atoms/cc. C_g is then 5.50×10^{22} atoms/cc minus the number of tantalum atoms/cc in the region of constant tantalum concentration, C_{ox} .

By normalizing the data in this fashion, it was possible to arrive at a set of curves (Figures 26 and 27) depicting how applied stress altered the original diffusion gradient in the unstressed unit. The curves in Figures 26 and 27 were obtained by plotting differences between the appropriate normalized curves obtained in the following manner:

Figure 26: Curve A - Sample 3 minus Sample 2
Curve B - Sample 9 minus Sample 3
Curve C - Sample 9 minus Sample 2

Figure 27: Curve D - Sample 10 minus Sample 2
Curve E - Sample 7 minus Sample 10
Curve F - Sample 7 minus Sample 2

where the applied stresses are identified by sample number in Table IV. These graphs show (1) how the original gradient is changed by thermal diffusion, and (2) how the thermal diffusion is changed by an electrical bias across the unit. Curve A shows the effect of thermal aging for two weeks at 125 C. The relatively high concentration of tantalum near the metal-oxide interface is due to the diffusion of tantalum atoms from the metal film across the interface into the oxide. The depletion of tantalum below the level of the original concentration gradient is observed at 350 A where the curve crosses zero. As the tantalum atoms acquire energy from the thermal stressing, a diffusion process is set up all through the oxide region where there are excess tantalum atoms originally. The atoms entering a lower concentration region will diffuse more rapidly than those entering a high region of concentration, and if the diffusion rates are sufficiently different, a decrease in the concentration will occur past a certain point. Curve B shows the effect that the application of a dc bias had on the thermal diffusion. The electric field accelerated the diffusion of tantalum atoms throughout the oxide. Again, the original concentration gradient had a marked effect on the stress-induced diffusion at various distances away from the interface. The effect of the electric field completely overshadowed the effect of thermal diffusion in the lower concentration region. Under dc bias, an abundance of tantalum atoms moved into the "sink" created by thermal diffusion beyond 350 A, raising the concentration level in this region above that of the original gradient. This increase is apparent in curve C, which shows the combined effects of the thermal and electrical induced diffusion. Curve D (Figure 27) shows the effect of thermal aging at 125 C for two weeks plus an additional 4 weeks at 70 C. Again, the diffusion of tantalum atoms from the metal film across the interface into the oxide is obvious. The depletion of tantalum below the level of the original gradient beyond 350 A oxide thickness is still discernible, but the effect has been greatly reduced. Apparently the stressing at lower temperature and longer time has filled in the "sink" created by the high temperature diffusion, and the whole system is tending

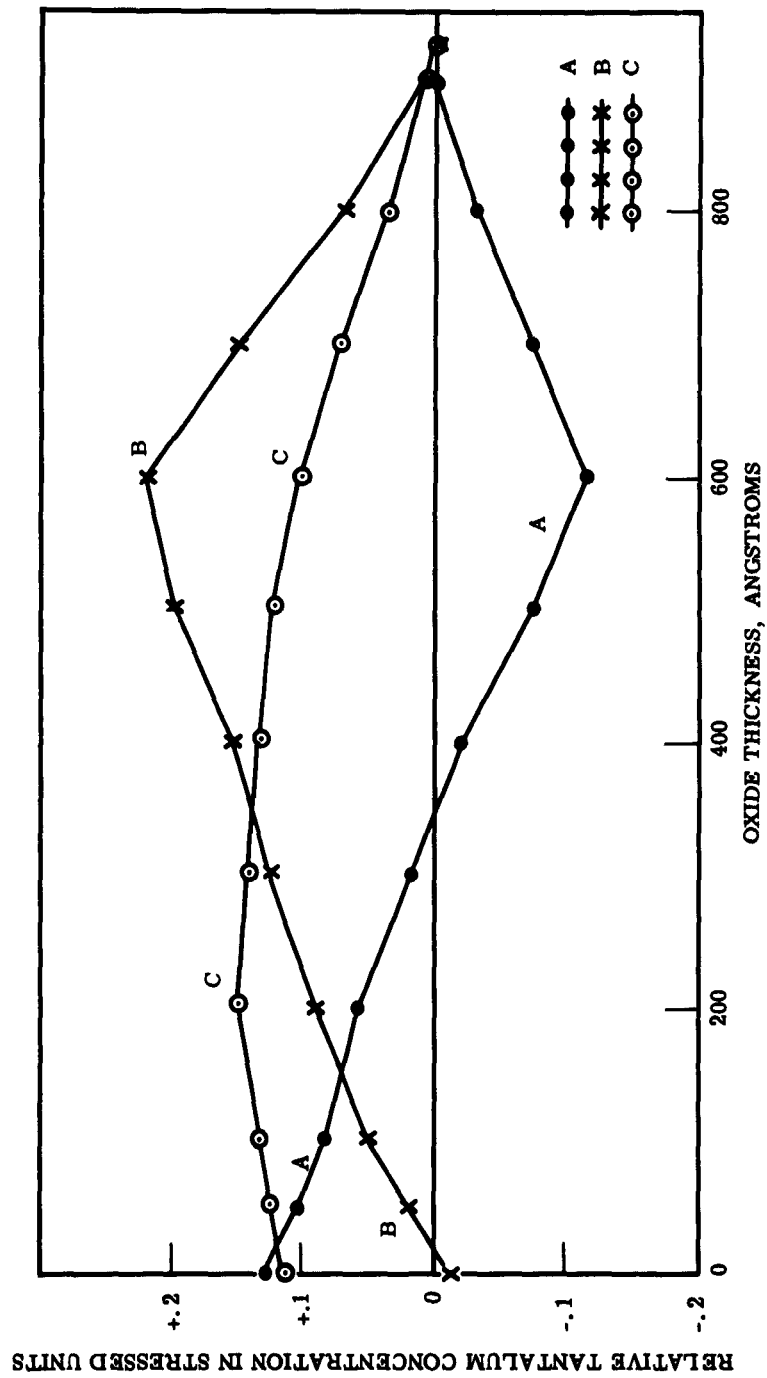


Figure 26. Normalized Curves of the Relative Tantalum Concentration Gradient in Stressed Units versus Oxide Thickness

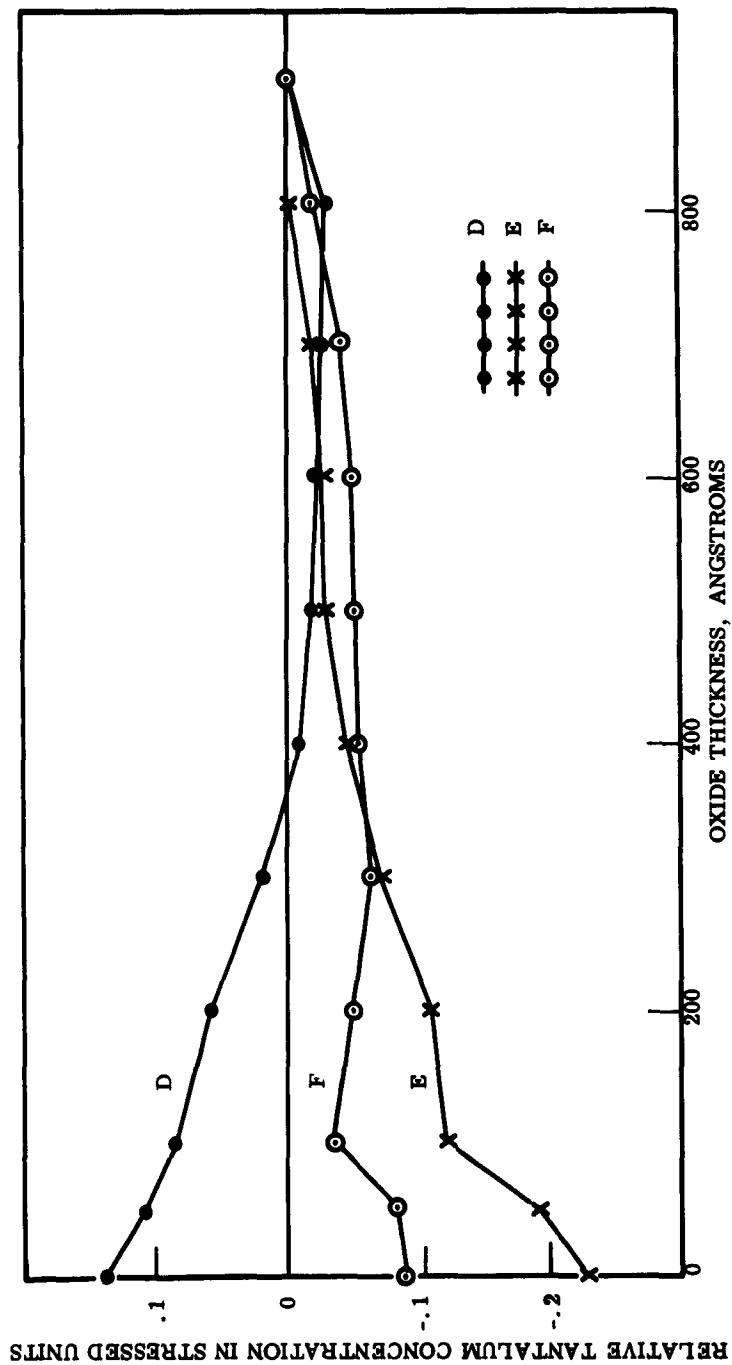


Figure 27. Normalized Curves of the Relative Tantalum Concentration Gradient in Stressed Units versus Oxide Thickness. (Samples No. 2, 10 and 7)

toward an equilibrium condition. The effect of electrical stressing upon this thermal diffusion is seen in curve E. Under these conditions, the electrical stress has completely overshadowed the thermal stress. The lowering of concentration throughout the oxide is caused by the electrical field pulling the tantalum atoms toward the oxide surface more rapidly than the thermal diffusion can supply them from the metal film. Curve F shows the effects of the combined thermal and electrical stress.

Since no obvious curve fits could be found for the graphs of concentration versus oxide thickness, diffusion constants were calculated for the various samples in an effort to find some quantitative measure of change for different stressing conditions. The accumulation of matter at a given point in a medium as a function of time in a nonstationary state of flow follows Fick's Second Law of Diffusion. By assuming that the tantalum-tantalum oxide system in this experiment is best represented by the model of a semi-infinite solid with a constant source, Fick's equation may be solved to give

$$C = C_s \left(1 - \frac{2}{\sqrt{\pi}} \int_0^{\frac{x}{2\sqrt{Dt}}} e^{-y^2} dy \right) \quad (10)$$

where

C = concentration of diffusing substance at any time, t

C_s = concentration of source

x = distance from interface

D = diffusion constant

$$y = \frac{x}{2\sqrt{Dt}} .$$

The expression $\frac{2}{\sqrt{\pi}} \int_0^{\frac{x}{2\sqrt{Dt}}} e^{-y^2} dy$ is the Gaussian error function, which may be evaluated from mathematical tables. Figure 28 plots the D values found at various oxide thicknesses. Because a slight change in the value of the concentration results in a large change in the value of D , experimental errors could result in D values which differ by a factor of two. Therefore, all D values which differed by a factor of two or less were averaged to give the values of D found in Table VII.

In Figure 28, attention is directed to the lower values of D near the interface for all the samples except sample #10. This is to be expected, as the tantalum atoms are diffusing into a region which already has a high concentration of excess tantalum atoms. The constancy of the D values for sample #10 would indicate that the long thermal diffusion undergone by this sample has tended to establish an equilibrium condition in the system.

No actual D values could be calculated for sample #6 (as anodized) because the effective time factor in the diffusion equation is unknown. The constancy of the product D times Time (t) values found for this sample lends support to the theory that the tantalum atoms are the mobile atoms during the anodization process.

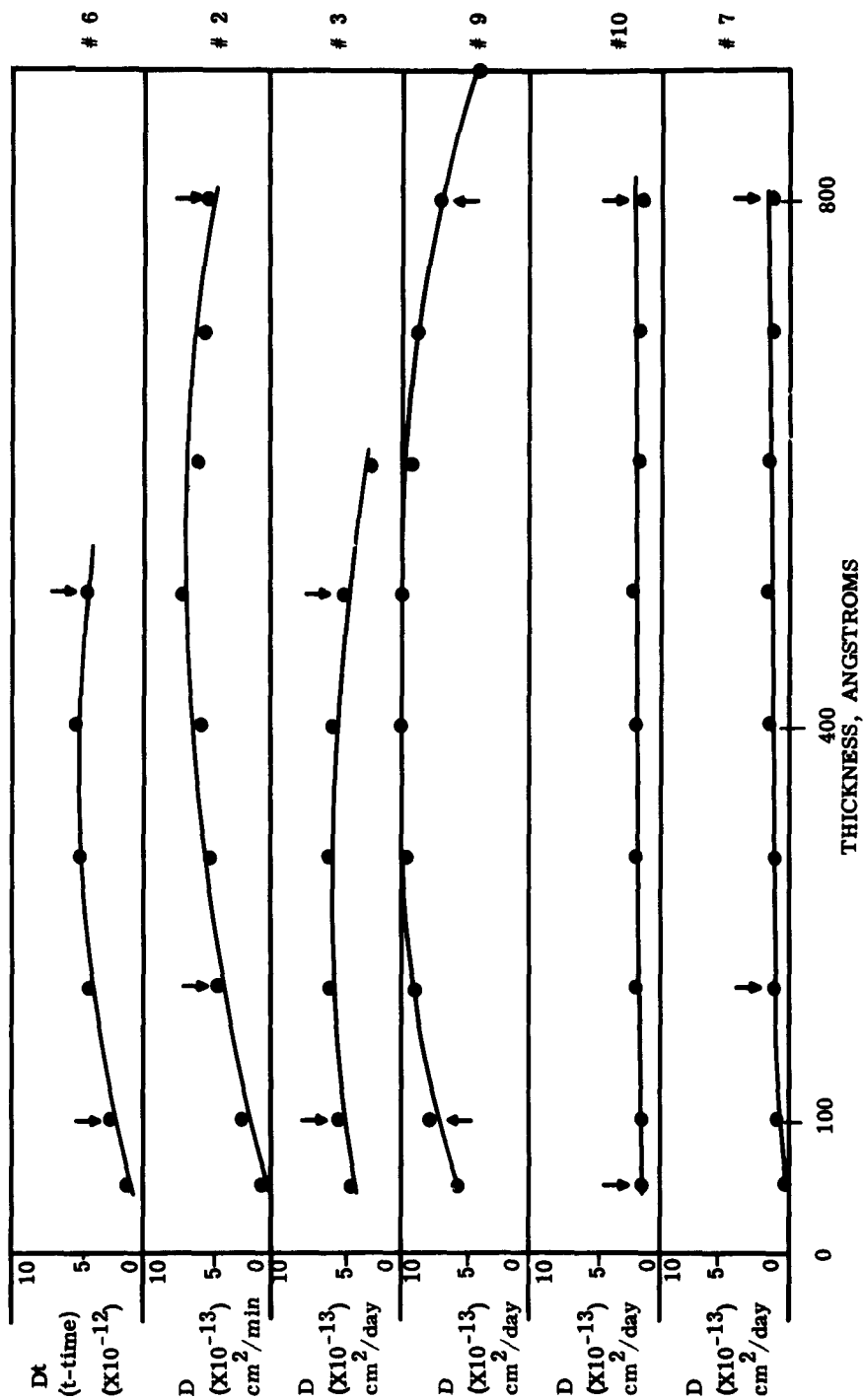


Figure 28. Diffusion Constants for Radioactive Tantalum-Tantalum Oxide Test Units.
(All points Between Arrows Averaged to Give D Values in Table VII.)

TABLE VII. DIFFUSION CONSTANTS FOR STRESSED AND UNSTRESSED TANTALUM-TANTALUM OXIDE UNITS		
SAMPLE NO.	TYPE OF STRESS	D
6	None	
2	Electrodes Only	$5.06 \times 10^{-13} \text{ cm}^2/\text{min.}$
3	Thermal	$4.93 \times 10^{-13} \text{ cm}^2/\text{day}$
9	Thermal + Electrical	$8.91 \times 10^{-13} \text{ cm}^2/\text{day}$
10	Thermal	$1.63 \times 10^{-13} \text{ cm}^2/\text{day}$
7	Thermal + Electrical	$1.32 \times 10^{-13} \text{ cm}^2/\text{day}$

In examining Table VII, attention is drawn to the high diffusion constant for sample #2 as compared with those for the other stressed samples. The electroding process itself appeared to make a much greater change in the concentration profile of the oxide than did the subsequent thermal and electrical stressing. One conclusion that might be made is that the tantalum-tantalum oxide films become much hotter during the deposition of the top electrodes than had previously been suspected giving rise to enhanced diffusion. However, since other factors need to be considered such as the effect of the vacuum on the film during deposition, no conclusion can be made at this time.

The effect of a dc bias applied to a unit held at a high temperature (125 C) can be evaluated by comparing the diffusion constants of samples #3 and #9 (Table VII). It can be seen that the applied electrical field has almost doubled the rate of diffusion due to thermal stressing alone. The diffusion constants for samples #10 and #7 are quite difficult to evaluate as these constants are actually an average of the constants obtained from stressing the same sample at two different temperatures (See Table IV). However, it is safe to say that the diffusion of tantalum atoms at a lower temperature (70 C) is much less than that at a higher temperature (125 C), which is consistent with diffusion theory.

4.2.5 Conclusion

This experiment was a preliminary study to evaluate techniques and to determine if diffusion actually occurred across the tantalum-tantalum oxide interface. It has definitely been shown that thermal and electrical stressed induced diffusion does occur across the interface and through the oxide. The diffusion process is strongly temperature dependent, even with the application of electrical stress. A great deal more work could be done along the lines followed by this experiment. Other thermal and electrical stress levels could be applied to further evaluate the diffusion processes. Additional electrical measurements such as the frequency dispersion of C and DF need to be taken on stressed and unstressed units to provide correlation with the diffusion studies.

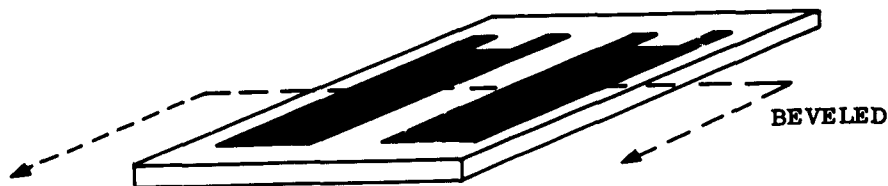
The effect of various fabrication processes such as the deposition of the counterelectrode should be investigated more completely.

4.3 OPTICAL MICROSCOPY - TANTALUM-TANTALUM OXIDE INTERFACE

Since the optical constants of the tantalum-tantalum oxide interface are unknown, the absolute thickness of the tantalum oxide layer cannot be determined by the reflection techniques described in Paragraph 4.2.2.4. Therefore, a technique for determining the absolute thickness of the oxide layer had to be developed. An optical profile of the tantalum-tantalum oxide interface was obtained by the selective etching and electroplating of a beveled cross section of the interface.

4.3.1 Experimental Technique

A quartz substrate with a deposited tantalum pattern was prepared for beveling studies. One pattern on the substrate was anodized; the other pattern was left intact (see sketch).

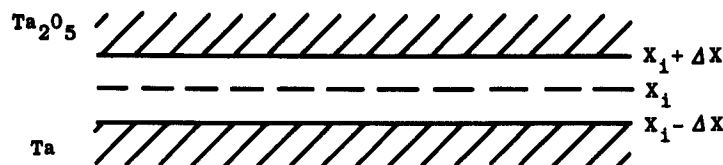


The unanodized tantalum film was used as a control and was measured to obtain the original tantalum thickness. The lower half of the substrate was beveled and processed in the following manner. The samples were mechanically beveled at an angle of $0^{\circ} 0' 20''$ using a specially designed dental drill attachment and a high-precision positioning sample fixture. The beveling head used Linde B (0.03μ) grinding compound embedded in Buehler short nap microcloth traveling at 865 surface feet per minute at an applied pressure of 0.5 psi. After beveling, the interface was cleaned and delineated by a 15-second etch in 80 per cent hydrogen fluoride-ethanol solution. After the etch, the samples were electrolytically plated for 10 seconds with copper using 1 M $\text{Cu}(\text{BF}_4)_2$ at 60 ma, and at 80 ma.

4.3.2 Tantalum-Tantalum Oxide Interface Determination

Figure 29 depicts a typical photomicrograph of a beveled interface after etching. The "etch band" delineated by lines c and b is a characteristic feature observed in all such beveled interfaces. The enhanced etching in this area suggests that there is more pronounced structure disorder here than elsewhere in the interface region. High structure disorder could result in a region where the transition from crystalline tantalum metal to amorphous tantalum oxide is most pronounced. The low level copper plating at 60 ma deposits copper uniformly up to line "d" in Figure 29. This plating is taken as a delineation of the low resistivity tantalum metal. The plating at higher current density, 80 ma, deposits copper up to line "b", the region between "d" and "b" plating in a spotty manner.

The interface between tantalum and tantalum oxide is defined as depicted in the sketch at the top of page 52.



The region between $X_1 - X$ to $X_1 + X$ represents a transition from tantalum metal to tantalum oxide and X_1 is taken as the effective interface or reference point for tantalum oxide thickness calculations. From the copper plating experiments, line "d" of Figure 29 is taken to coincide with $X_1 - X$, and line "b" with $X_1 + X$. Since line "c" of Figure 29, defining the lower limit of the pronounced "etch band" in the interface is a reproducible characteristic of the beveled and etched interfacial region, and since the limit or error in determining line "c", $\pm 100\text{\AA}$, includes the range between $X_1 + X$ and $X_1 - X$, i.e., "b" and "d" 219\text{\AA}, line "c" is identified with X_1 , the mean thickness of the oxide layer, 1754\text{\AA} (see Figure 30).

With this absolute measurement of oxide thickness, the reflectance thickness measurements described in Paragraph 4.2.2.4 could be calibrated. It was determined that the constant X in Equation (5), Paragraph 4.2.2.4, had a value of 156\text{\AA}.

The absolute thickness measurements also made it possible to determine the anodizing constant at an average value of 19.9\text{\AA} per volt.

4.4 TIN OXIDE - SUBSTRATE INTERFACE MODEL SYSTEM

4.4.1 Summary of Efforts to Date

Measurements of the effect of thermal and thermal-electrical stresses on the resistivity, temperature coefficient of resistivity, and current noise index on tin oxide films deposited on a variety of substrate surfaces (see Table VIII) were investigated to gain an understanding of modes of failure originating at the film substrate interface. A large body of experimental data was obtained which allowed the following empirical correlations to be made.

The films deposited on the substrates with the highest thermal conductivities exhibited the highest resistivities, and when comparing substrates of comparable thermal conductivities, differences in resistivities could be explained by varying degrees of ionic contamination from the substrate. It was also shown that films deposited on substrate surfaces exhibiting large surface asperities exhibited anomalously high resistivities.

Increases in resistance and temperature sensitivity of the conduction process in films under high thermal-electrical stress have been directly related to the thermal conductivity of the substrate with films on substrates of higher thermal conductivity exhibiting greatest stability with stress. Lower-level thermal-electrical stress levels usually brought about stabilizing changes in resistance value for these films on substrates whose expansion properties, crystal order or chemical composition do not alter the film structure or composition. Decreases in resistance values with thermal cycling were initially related to structural changes in the films which are related to a mismatch in expansion properties and the surface structures of the substrate. Current noise measurements showed no obvious empirical correlations with any particular substrate property or resistor characteristics.

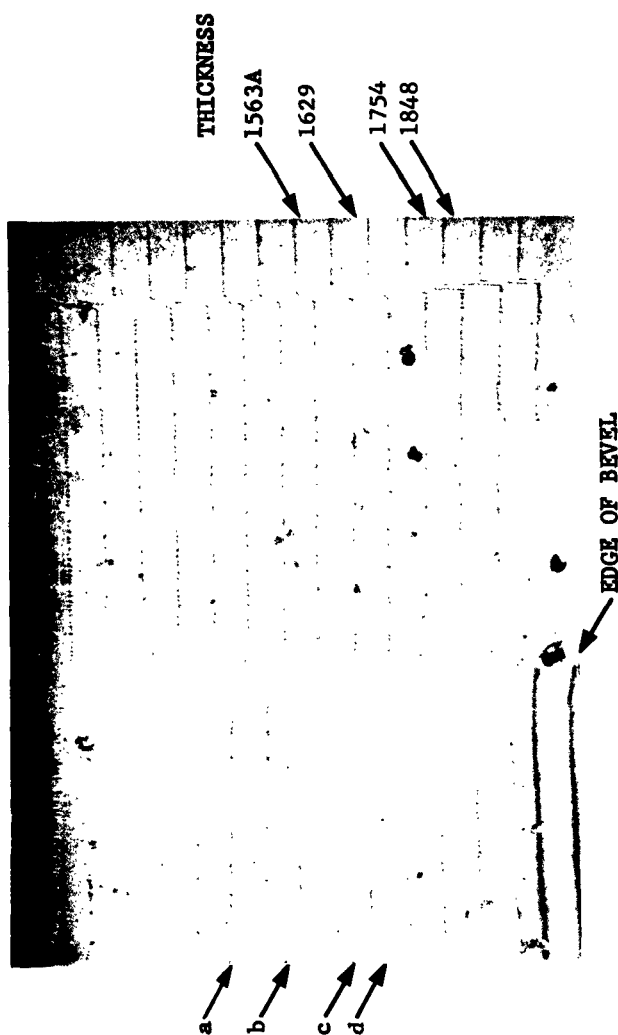


FIGURE 30. Interferometric Profile of Beveled Interface.
(63X, = 5460 Å, fringe density of 120 per cm.)

Note:

The beveling angle is determined to be $0^{\circ}0'20''$ from the interferometric profile. Thickness measurements were taken at lines a, b, c, d by measuring line spacings directly with a traveling-cross hair Filar Micrometer attachment. The step heights were calculated at different distances away from the step to average out possible substrate curvature and surface roughness.

TABLE VIII SUBSTRATE PROPERTIES			
Composition	Thermal Coef. of Expansion ($\times 10^{-6}/^{\circ}\text{C}$)	Thermal Conductivity (25 $^{\circ}\text{C}$) (cal/cm-sec- $^{\circ}\text{C}$)	Surface Structure (One microinch finish)
Corning 7059 Glass Aluminosilicate	4.5	0.003	Glass
Fused Quartz Silicon Dioxide	0.56	0.004	Glass
Glass-Ceramic (Fotoceram) Silicon Dioxide, Group I, II Additives	10.4	0.0056	Polycrystal
Glazed Alumina (94% Alumina) Aluminosilicate Glaze with Group I, II Additives	6.8	0.045	Glass
Sapphire Aluminum Oxide	6.58 \parallel C axis 5.43 \perp C axis	0.065	Single Crystal
Microscope Slide Soda-Lime	9.0	0.003	Glass
Unglazed Alumina 94% Alumina	6.8	0.045	Polycrystal (16 microinch)

Hall-effect measurements were undertaken to attempt a more quantitative analysis of the electrical behavior of resistors under stress. The results of these Hall-effect measurements initiated during the third quarter and completed in the fourth quarter will be described in detail in Paragraph 4.4.2

4.4.2 Experimental Work in Fourth Quarter

4.4.2.1 Hall-Effect Measurements

It was recognized that the interpretation of the Hall-effect data defining the changes in the basic conduction mechanism as functions of applied stress, nature of the substrate, and the chemical and physical nature of the film would offer the most quantitative analysis of failure mechanism in the resistor films.

The experimental approach was as follows. A test group of tin oxide films deposited on the selected substrates (Table VIII) were stressed by successive thermal cycling from room temperature to 200 $^{\circ}\text{C}$ in an inert atmosphere (see Third Quarterly Report). Hall-effect measurements were taken on the initial units and after successive periods of cycling. A second group of test units were put under thermal-electrical stress of 0.5 watts per square inch for 168 hours, followed by an additional stress of 1.0 watts per square inch for 168 and 504 hour intervals (see Third Quarterly Report). Hall data was obtained on the initial units and after successive periods of stress.

A tabulation of the Hall data including the room temperature Hall mobility, and its temperature dependence, room temperature conductivity, and concentration of charge

TABLE IX TABULATED DATA GROUP 15
THERMAL-ELECTRICAL STRESS
ROOM TEMPERATURE VALUES

SUBSTRATE	Initial μ $\mu \sim T^x$ (x)	1st Stress (1) μ $\mu \sim T^x$ (x)	% Change With Stress $\Delta\mu$ $\Delta N^{(3)}$ $\Delta\sigma$	2nd Stress (2) μ $\mu \sim T^x$ (x)	Additional % Change With Stress $\Delta\mu$ ΔN $\Delta\sigma$
Corning 7059 Glass	17.6 .15 110	17.7 .12 109	<1 <1 <1		
Fused Quartz	21.2 .05 111	20.5 .05 106	-3.3 -0.9 -.45		
Sapphire	16.4 .27 68.6	15.2 .29 70.0	-7.3 10 2.1	15.0 0.30 67.0	-1.3 -3.1 -4.3
Fotoceram	15.5 .21 82.6	14.4 .25 76.4	-7.1 <1 -7.5	14.2 0.30 75.5	-1.4 <1 -1.2
Glazed Alumina	15.0 .17 89.5				
Unglazed Alumina	12.2 .18 28.3	11.2 .22 25.6	-8.2 -1.3 -9.5		
Microscope Slide	~2.0 .86 ~6	2.0 *~7.4			

* See Figure 44

(1) 1st. Stress: Combined stress of 0.5 watts per sq. inch for 168 hours, plus 1.0 watts per sq. inch for 168 hrs.

(2) 2nd. Stress: Combined stress of 0.5 watts per sq. inch for 168 hours, plus 1.0 watts per sq. inch for 672 hrs.

(3) Calculated from data in Table XI

Units: μ in $\text{cm}^2/\text{volt sec} : \sigma$ in $(\text{ohm cm})^{-1}$

TABLE X
TABULATED DATA GROUP 16
THERMAL STRESS
ROOM TEMPERATURE VALUES

SUBSTRATE	Initial			1st Stress(1)			%Change With Stress(2)		
	μ	$\mu \sim T^x$ (x)	σ	μ	$\mu \sim T^x$ (x)	σ	$\Delta\mu$	ΔN	$\Delta\sigma$
Corning 7059 Glass	24.6	0.08	170	23.8	0.03	164	-3.2	0	-3.5
Fused Quartz	19.8	~ 0	228	21.6	~ 0	254	9.1	2.2	11.4
Sapphire	16.5	0.11	152	20.4	0.06	186	24.6	-1.4	22.4
Fotoceram	14.7	0.16	134	16.0	0.12	147	8.8	1.2	9.6
Glazed Alumina	17.8	0.11	155	21.3	0.06	174	19.6	-6.4	12.2
Unglazed Alumina	11.0	0.16	54.8	11.4	0.18	54.3	3.6	-4.5	-1.0
Microscope Slide	3.4	0.55	6.30	5.0	0.68	10.8	47.0	16.4	71.5
(1) 1st Stress: 10 cycles from room temperature to 200 C (2) Calculated from data in Table XII Units: μ in $\text{cm}^2/\text{volt sec}$ σ in $(\text{ohm cm})^{-1}$									

carriers at various temperatures are given in Tables IX through XII. The variation of these quantities with different stress levels is also tabulated. Log-log plots of the Hall mobility and conductivity as a function of temperature for the various test units are given in Figures 31 to 44. (The experimental techniques and calculations are described in detail in the Second Quarterly Report). The room temperature Hall mobilities tabulated in Tables IX and X vary in some instances from a similar tabulation presented in the Third Quarterly Report. In particular, the change in mobility with stress for the sapphire unit, Group 15, and the unglazed alumina unit, Group 16, the Corning 7059 glass unit, Group 16, is less than previously recorded; the change noted for the Fotoceram unit, Group 16, is similar in magnitude, but in an opposite direction. A more concise analysis of the experimental data carried out during the fourth quarter led to these revisions.

The plots of the temperature dependence of the Hall mobility represent the most accurate characterization of the conduction process, since a knowledge of film thickness is not required. The small scatter in the mobility plots is due to the small hysteresis observed as the test units were cycled from room temperature down to liquid nitrogen temperature and up to 125 C and back to room temperature. The hysteresis was probably due to thermal lag in the system. The mobility versus temperature data was empirically fitted to a straight line log-log plot, with emphasis placed on the higher temperature data. The room temperature mobility values were taken off the straight line fit of the data. The mobility versus temperature plot for the stressed microscope slide test unit, Group 15, which exhibits a completely different functionality, will be discussed in Paragraph 4.4.2.3.

TABLE XI TABULATED DATA-CHARGE CARRIER CONCENTRATION: GROUP 15
N X 10¹⁹

Substrate	Initial Temperature (°K)				1st Stress (2) Temperature (°K)				2nd Stress (3) Temperature (°K)			
	<200 ⁽¹⁾	250	400	AVE	<200	250	400	AVE	<200	250	400	AVE
Corning 7059 Glass	3.89	3.93	3.91	3.91	3.96	3.86	3.86	3.89				
Fused Quartz	3.21	3.29	3.35	3.28	3.24	3.22	3.29	3.25				
Sapphire	2.64	2.64	2.59	2.62	2.90	2.80	2.94	2.88	2.90	2.74	2.73	2.79
Fotoceram	3.37	3.32	3.29	3.33	3.38	3.30	3.25	3.31	3.40	3.32	3.29	3.33
Glazed Alumina	3.78	3.67	3.74	3.73								
Unglazed Alumina	1.46	1.43	1.46	1.45	1.41	1.41	1.46	1.43				
Microscope Slide	1.94	1.95	1.98	1.96	0.48	2.18	2.10					
(1) < 200: from 140 to 160												
(2) see Table IX												
(3) see Table X												

TABLE XII TABULATED DATA-CHARGE CARRIER CONCENTRATION, GROUP 16 N X 10 ¹⁹								
Substrate	Initial Temperature (°K)				1st Stress ⁽²⁾ Temperature (°K)			
	<200 ⁽¹⁾	250	400	AVE	<200	250	400	AVE
Corning 7059 Glass	4.35	4.32	4.27	4.31	4.30	4.30	4.33	4.31
Fused Quartz	7.29	7.25	7.05	7.19	7.33	7.33	7.40	7.35
Sapphire	5.84	5.78	5.68	5.76	5.62	5.62	5.80	5.68
Fotoceram	5.62	5.71	5.66	5.66	5.77	5.70	5.73	5.73
Glazed Alumina	5.48	5.44	5.48	5.46	5.07	5.07	5.19	5.11
Unglazed Alumina	3.15	3.12	3.09	3.12	3.01	2.96	2.96	2.98
Microscope Slide	1.16	1.16	1.15	1.16	1.43	1.34	1.27	1.35
(1) < 200: from 140 to 160								
(2) see Table XI								

The concentration of charge carriers (N) calculated from the Hall constant, which is directly proportional to the measured Hall voltage *, exhibited a small scatter similar to the mobility data. However, in all cases except the stressed microscope slide test unit, Group 15, the value of N and hence, the Hall constant, were essentially constant and temperature independent over the temperature range investigated. Values of N tabulated in Tables XI and XII were calculated from the average measured Hall voltage at that temperature.

The conductivity values tabulated in Tables IX and X are the product of the average value of N times the room temperature value of the mobility

$$\text{i.e., } \sigma = N \cdot e \cdot \mu = \frac{1}{R_H} \cdot \mu = \left[\frac{V_H}{1} \cdot \frac{1}{B} \cdot t \cdot 10^8 \right]^{-1} \cdot \frac{V_H}{1} \cdot \frac{1}{B} \cdot 10^8 \text{ } (\Omega/\square)^{-1}$$

$$(\Omega/\square)^{-1} \cdot t^{-1} *$$

*N = 1/R_He where R_H = Hall constant in cm³/coulomb, e = 1.60 x 10⁻¹⁹ coulomb

R_H = μ/σ = $\frac{V_H}{I} \cdot \frac{I}{B} \cdot t \cdot 10^8$ where V_H = Hall voltage, I = current, B = magnetic field (gauss), t = thickness (cm)

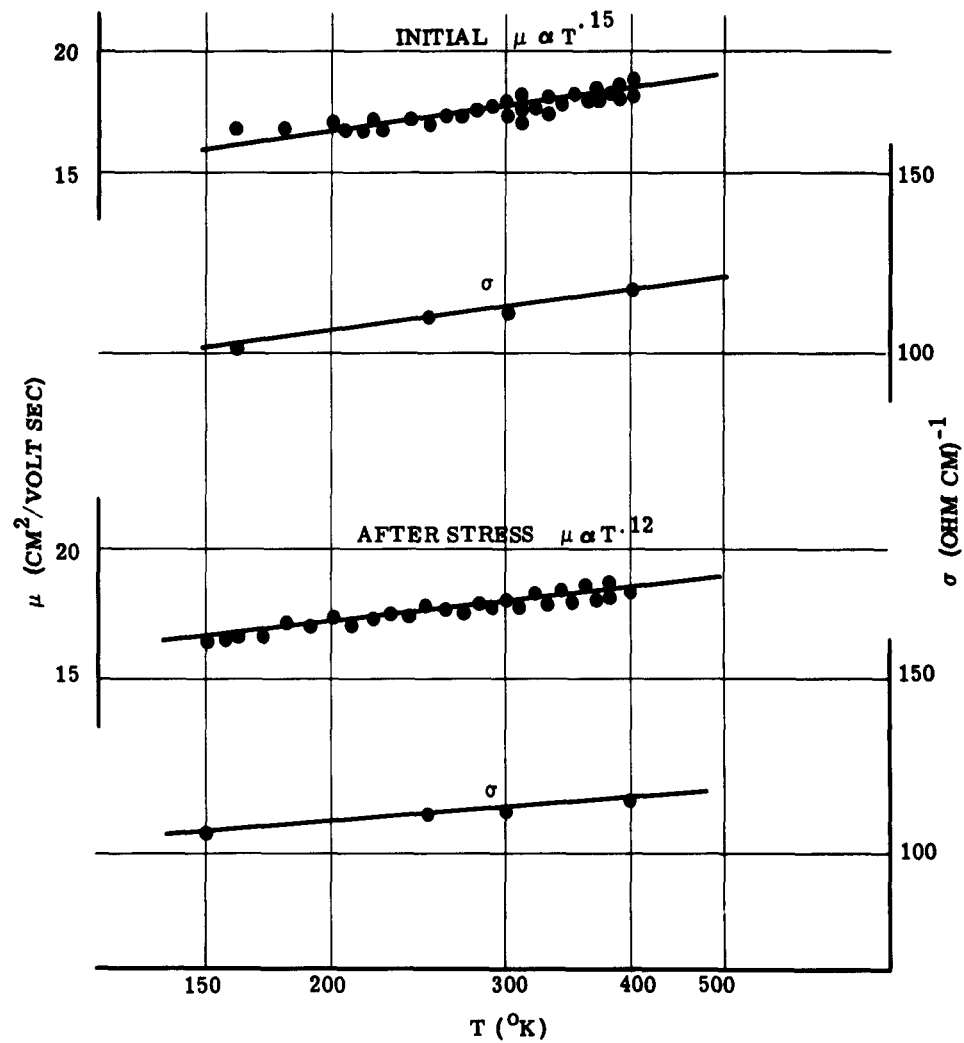


Figure 31. Corning 7059 Glass Test Unit, Group 15, Thermal-Electrical Test

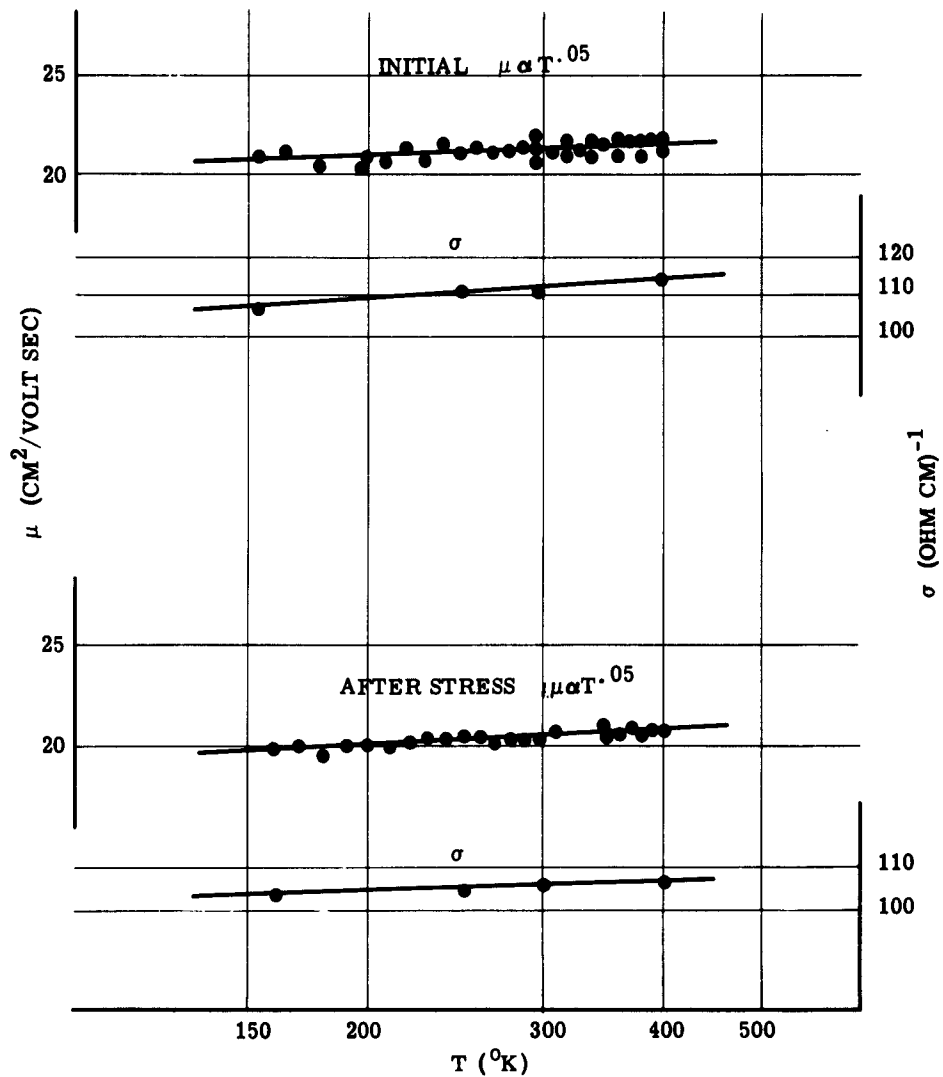


Figure 32. Fused Quartz Test Unit, Group 15, Thermal-Electrical Stress

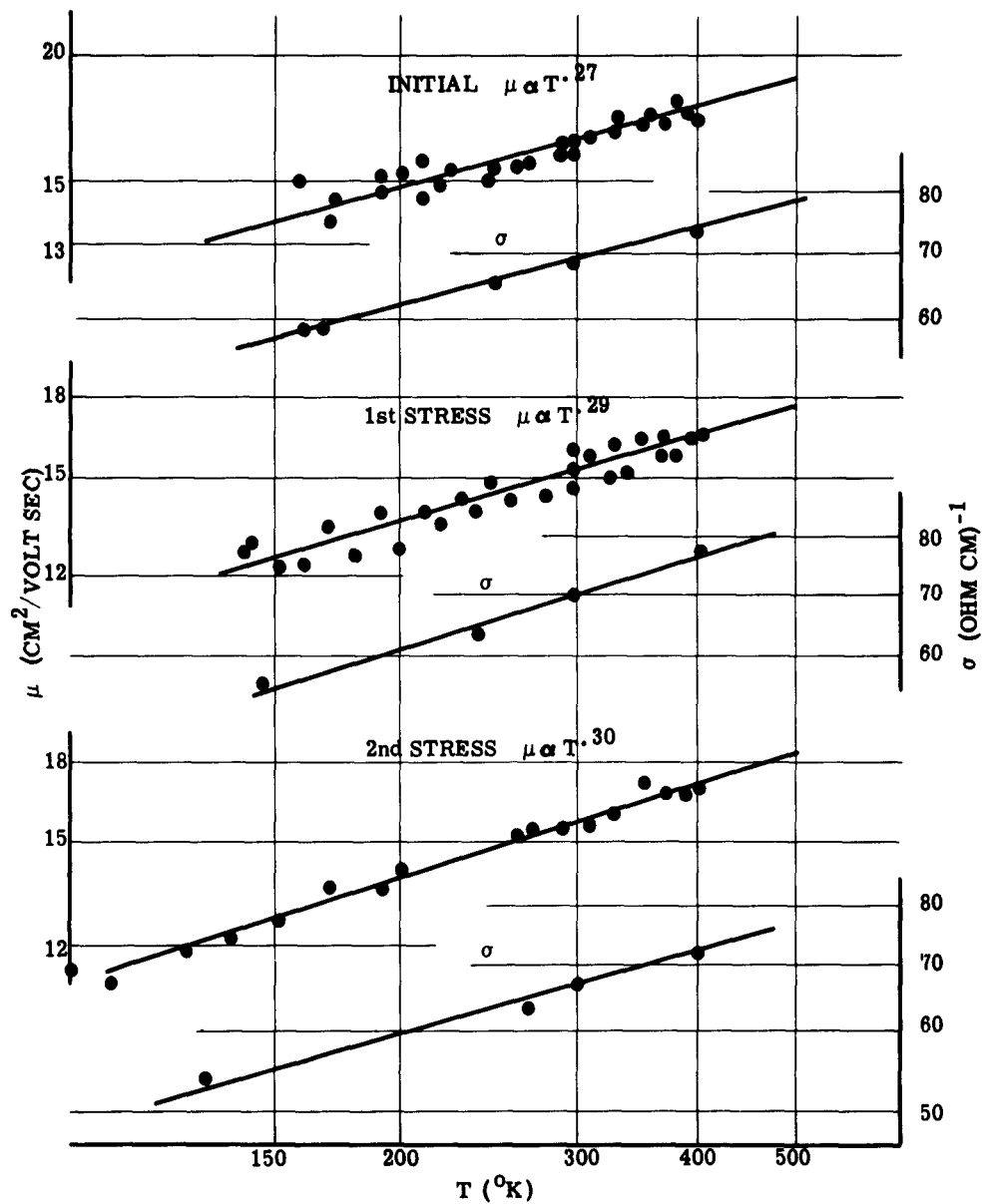


Figure 33. Sapphire Test Unit, Group 15, Thermal-Electrical Stress

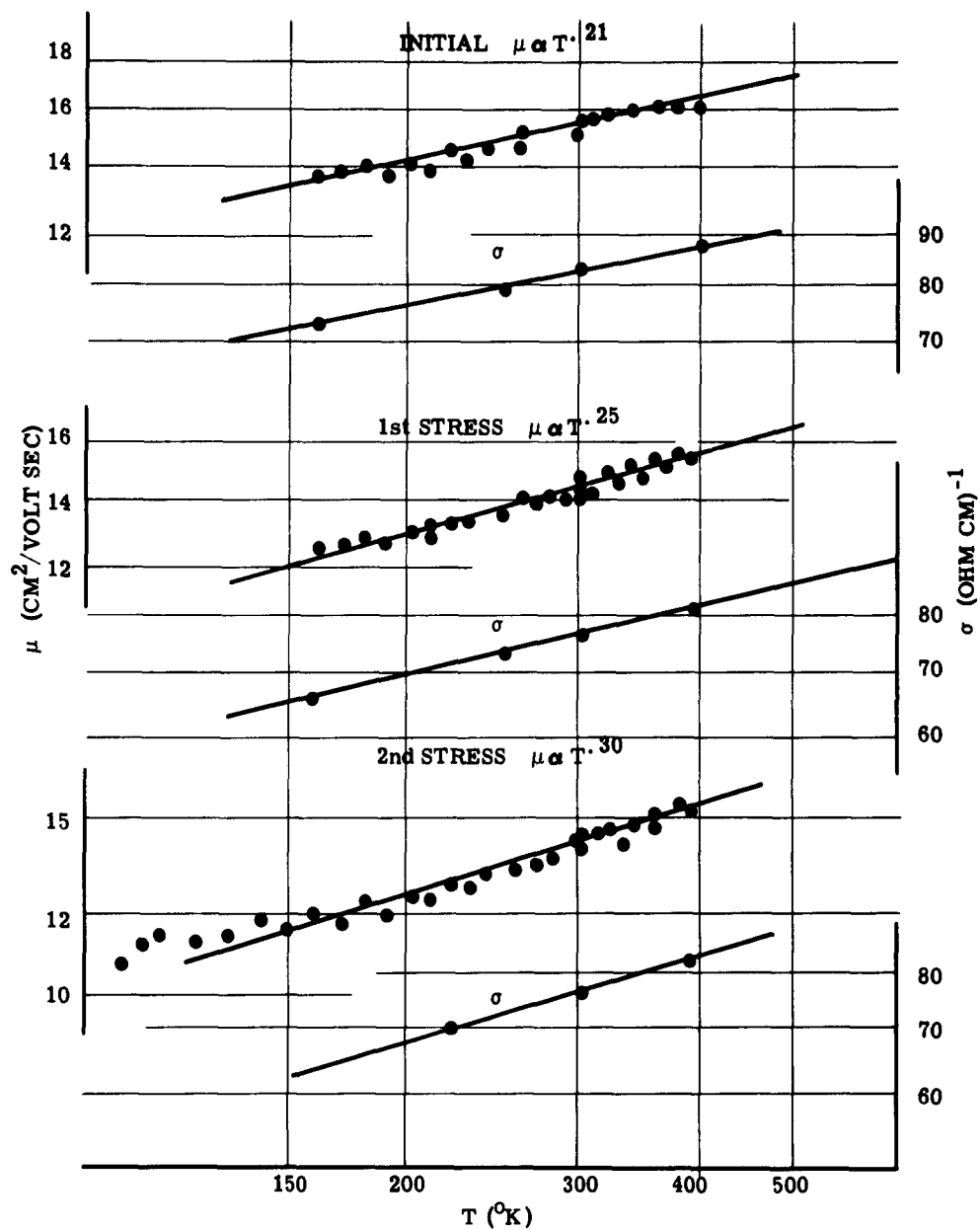


Figure 34. Fotoceram Test Unit, Group 15, Thermal-Electrical Stress

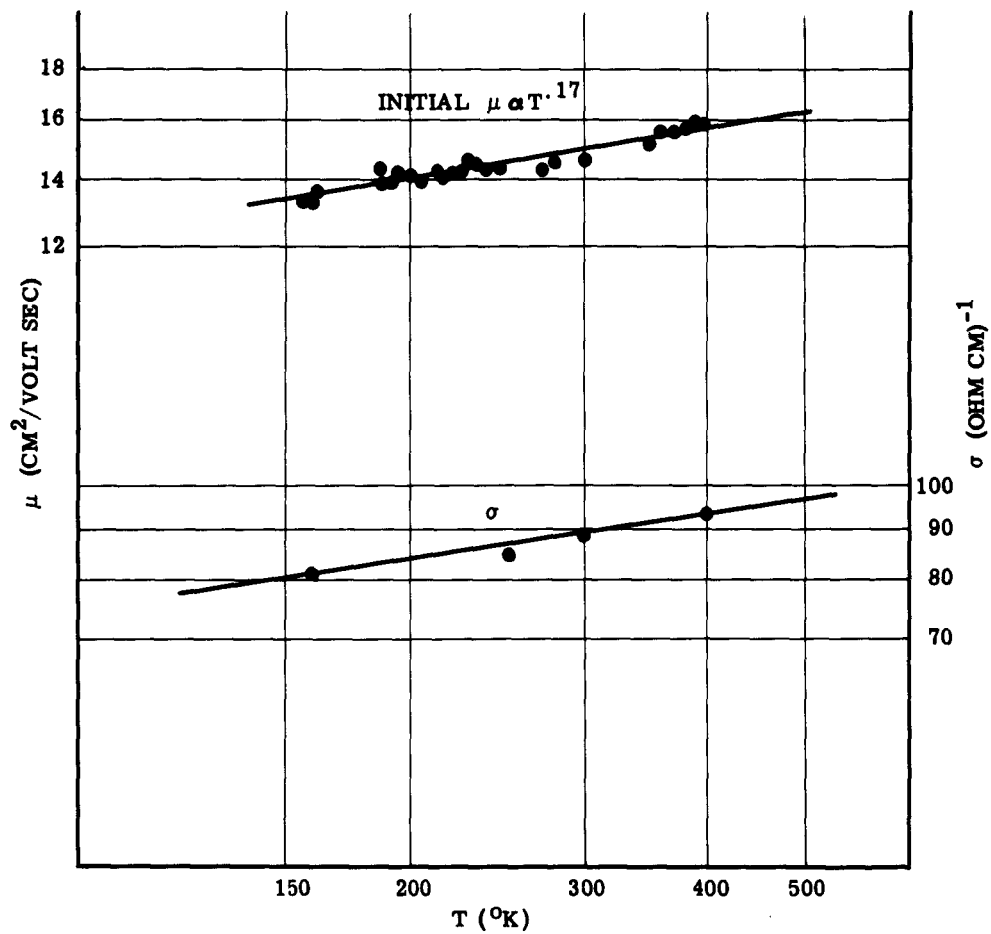


Figure 35. Glazed Alumina, Group 15, Not Stressed

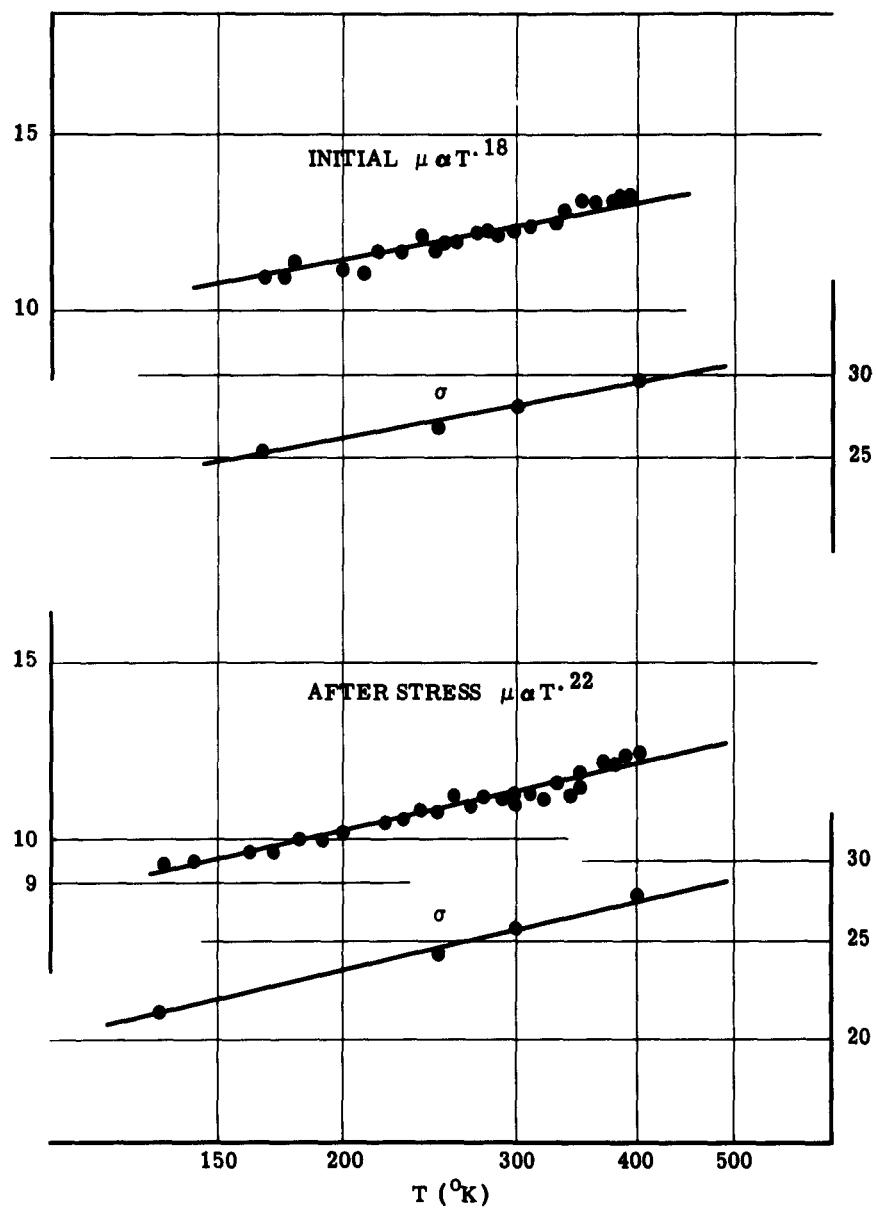


Figure 36. Unglazed Alumina, Group 15, Thermal-Electrical Stress

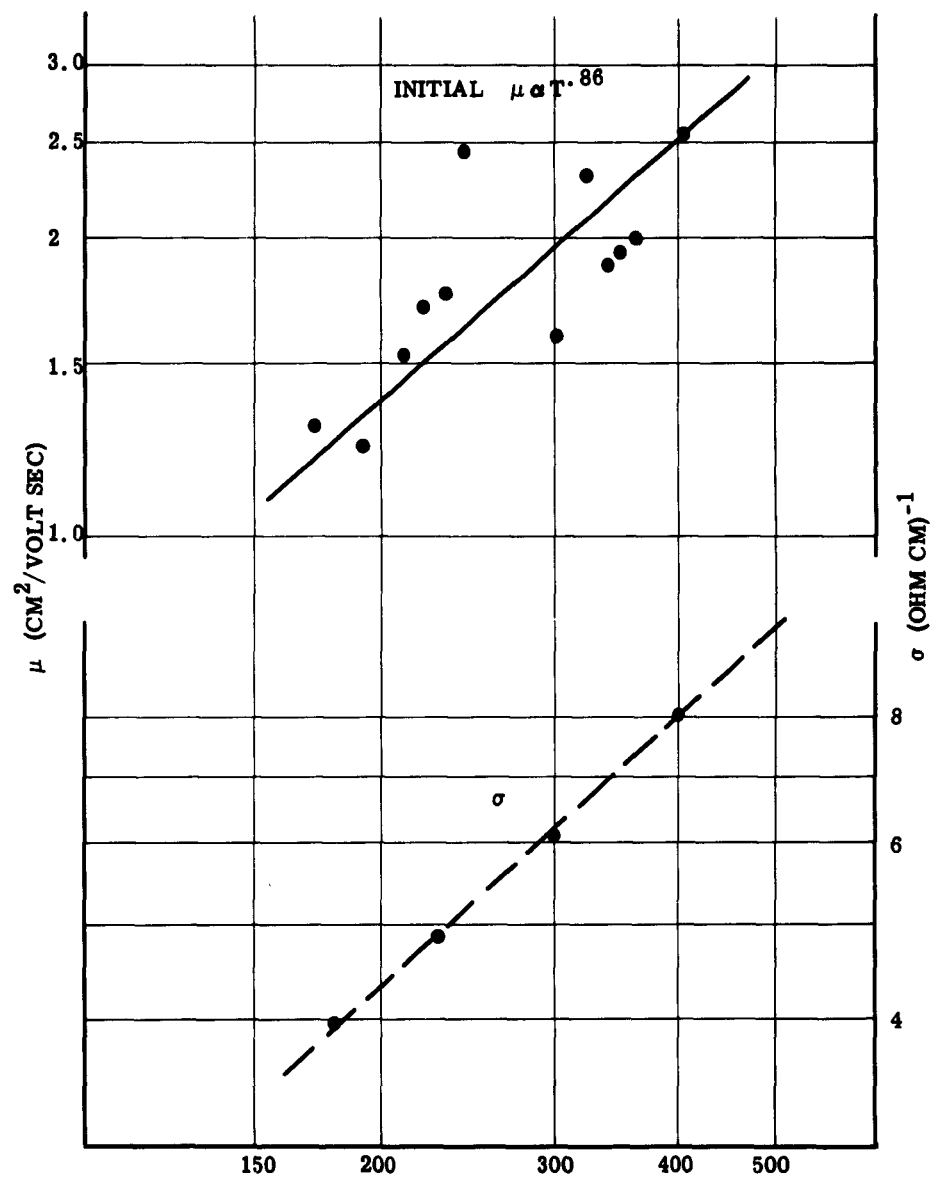


Figure 37A. Microscope Slide Test Unit, Group 15, Thermal-Electrical Stress

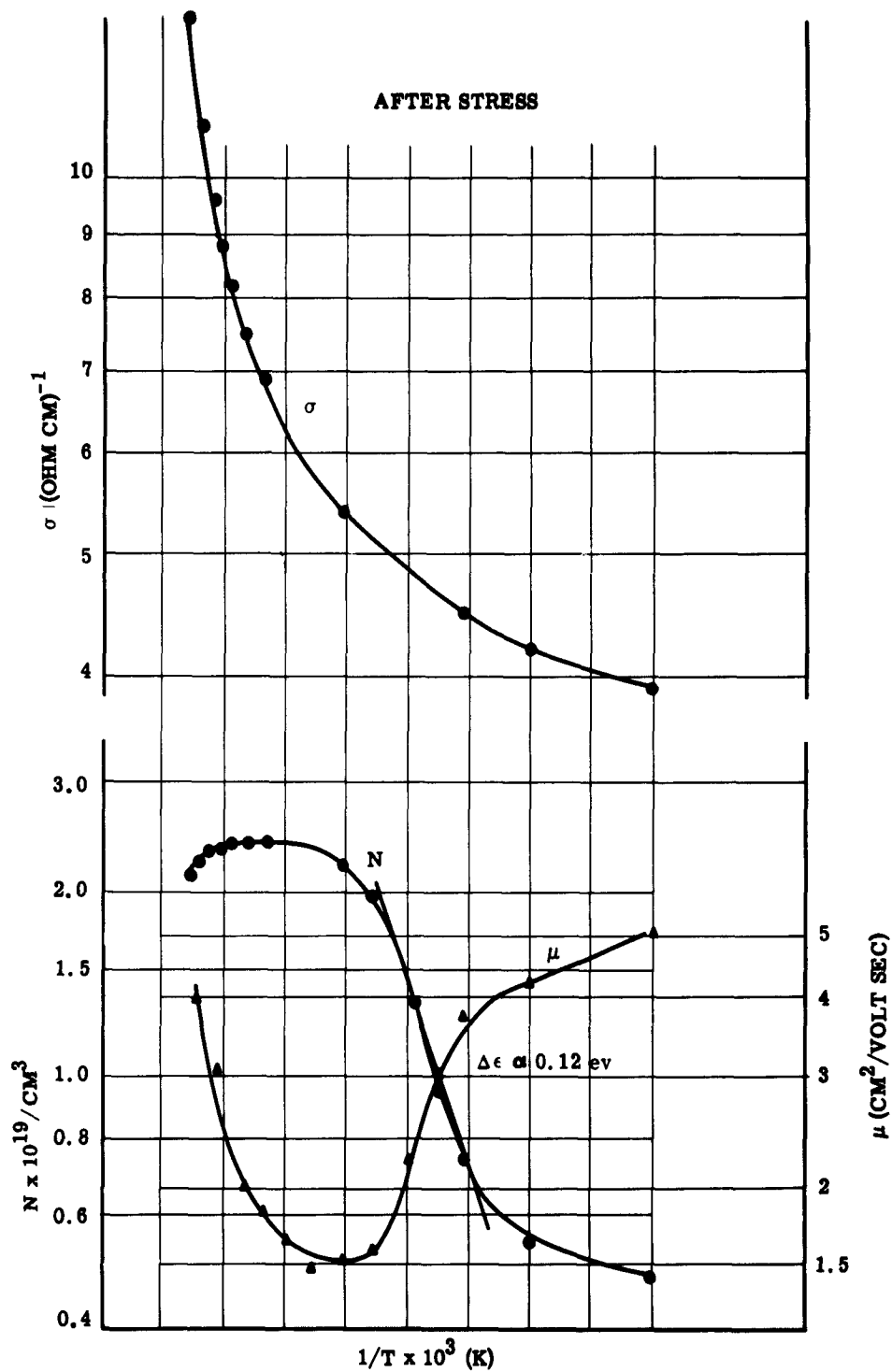


Figure 37B. Microscope Slide Test Unit, Group 15, Thermal-Electrical Stress

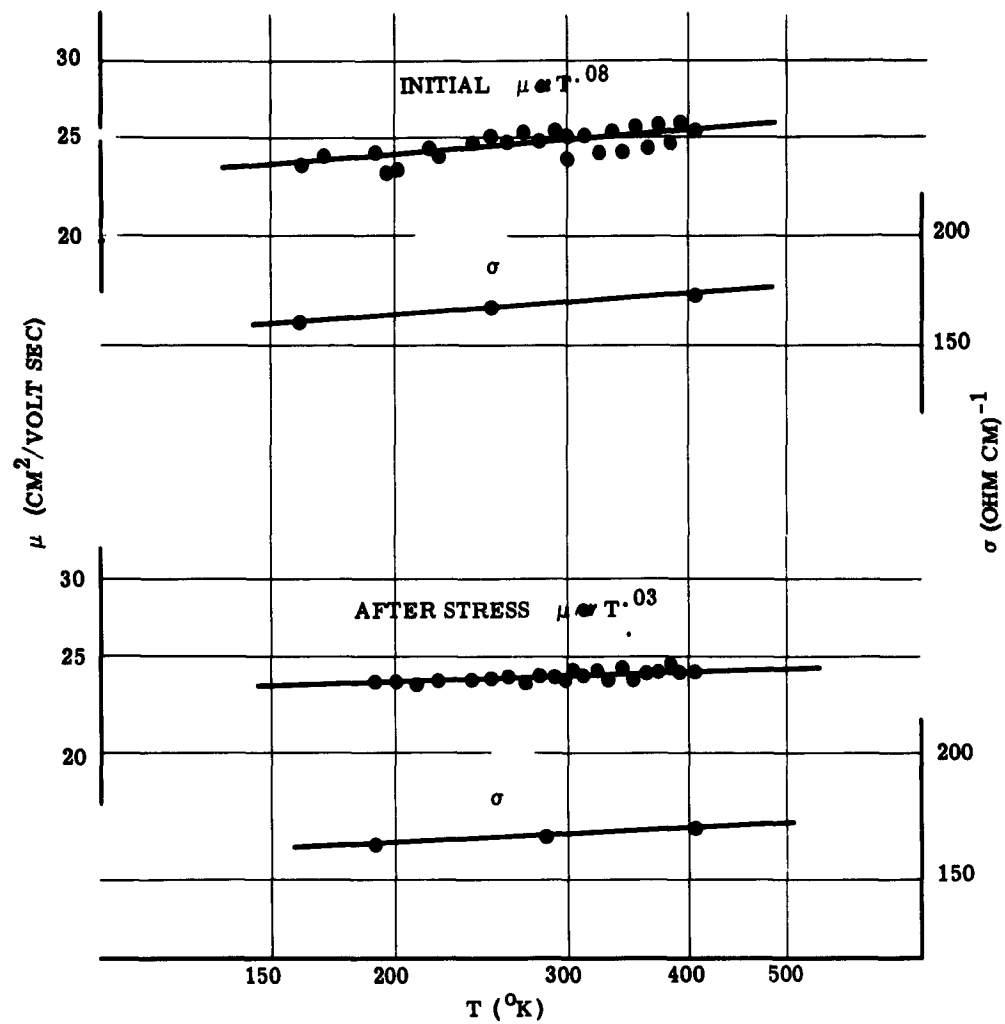


Figure 38. Corning 7059 Test Unit, Group 16, Thermal Stress

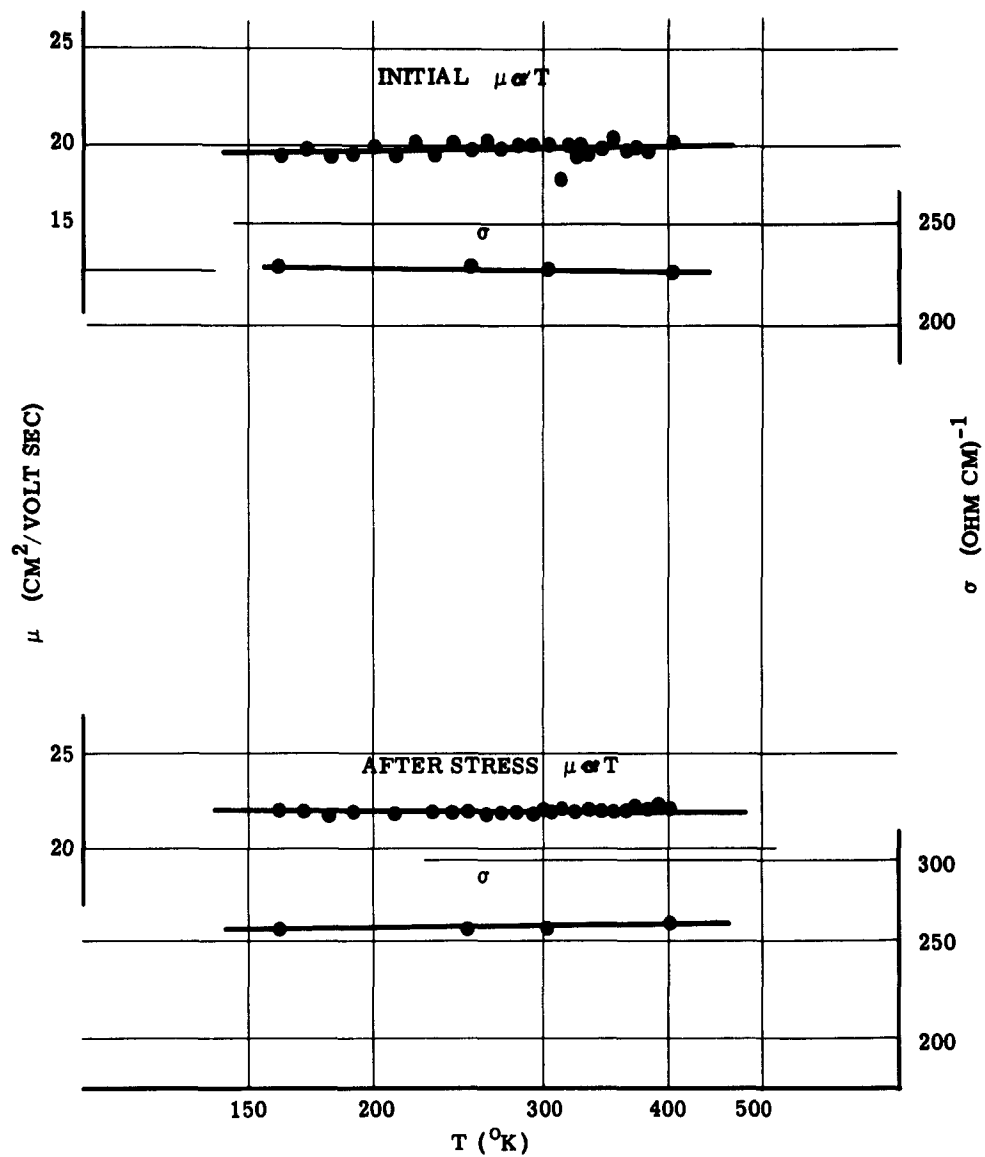


Figure 39. Fused Quartz Test Unit, Group 16, Thermal Stress

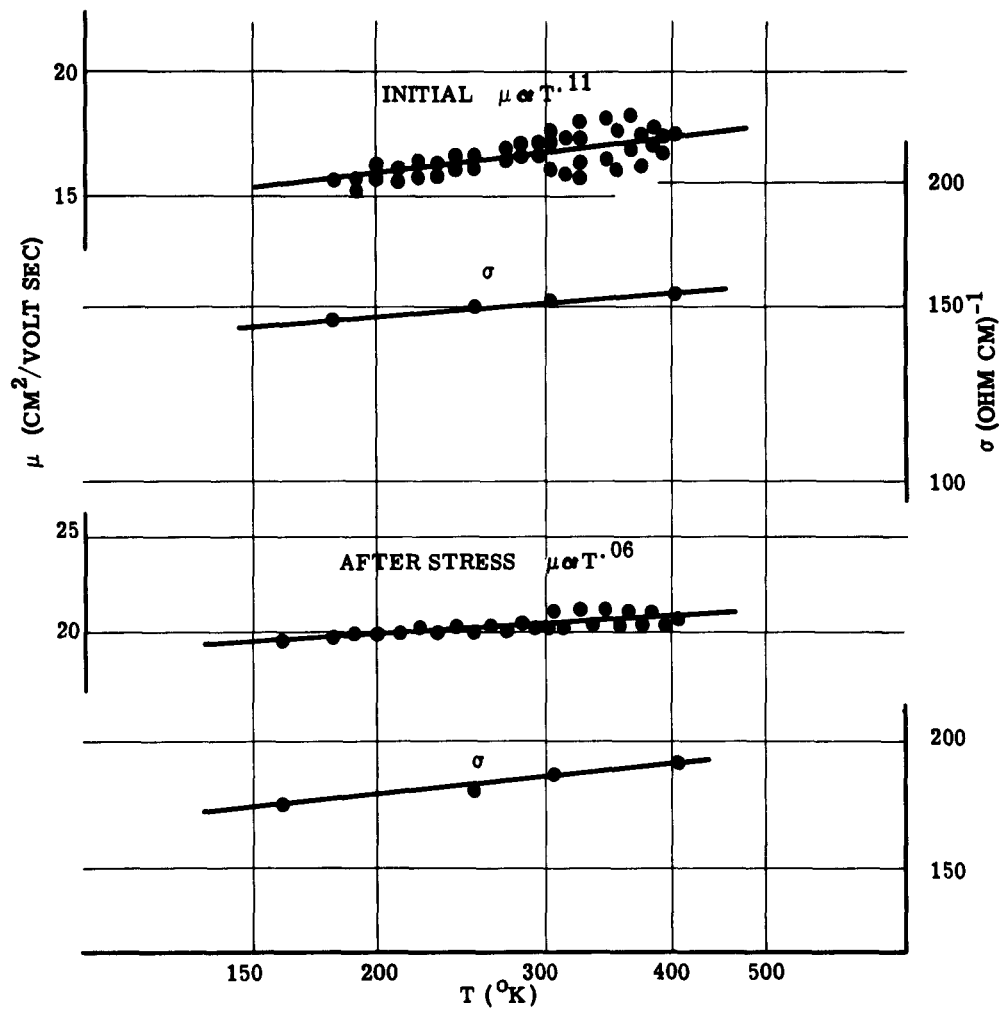


Figure 40. Sapphire Test Unit, Group 16, Thermal Stress

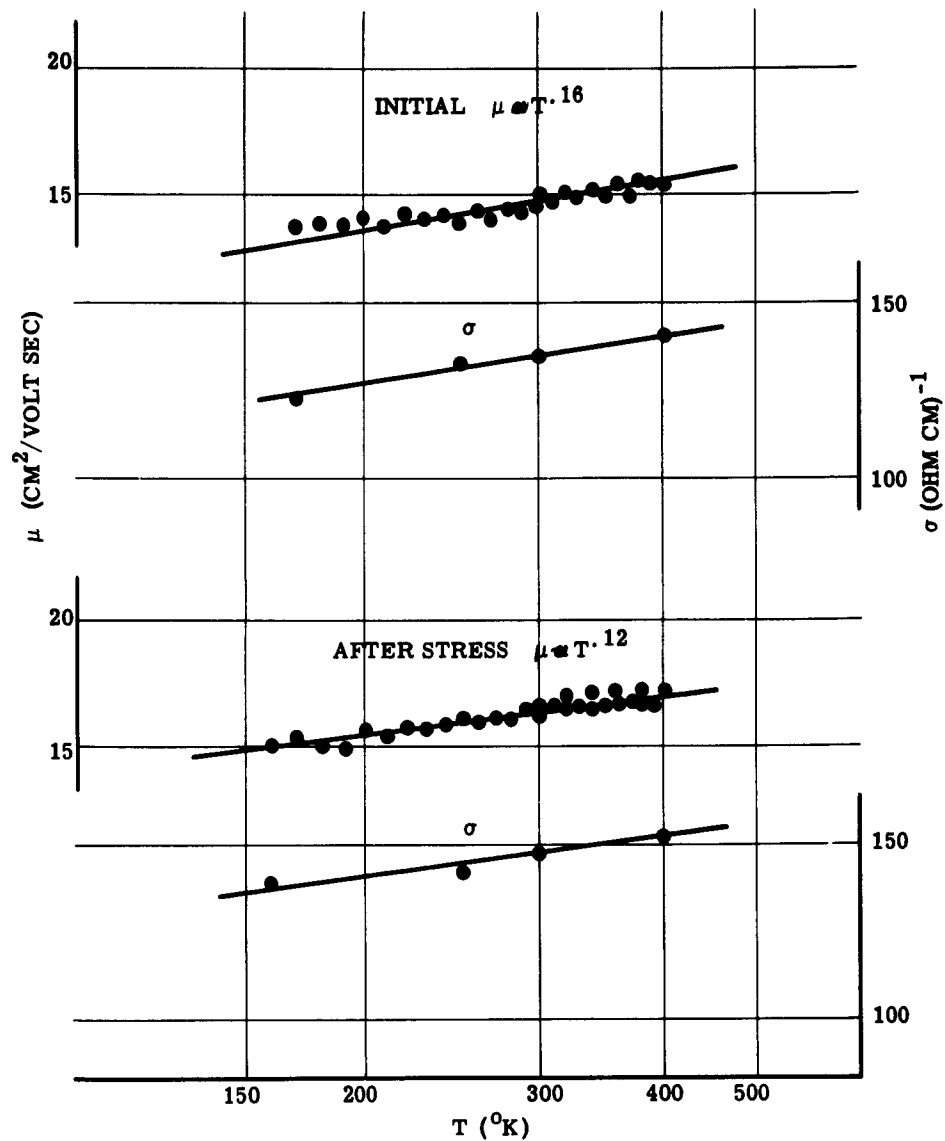


Figure 41. Fotoceram Test Unit, Group 16, Thermal Stress

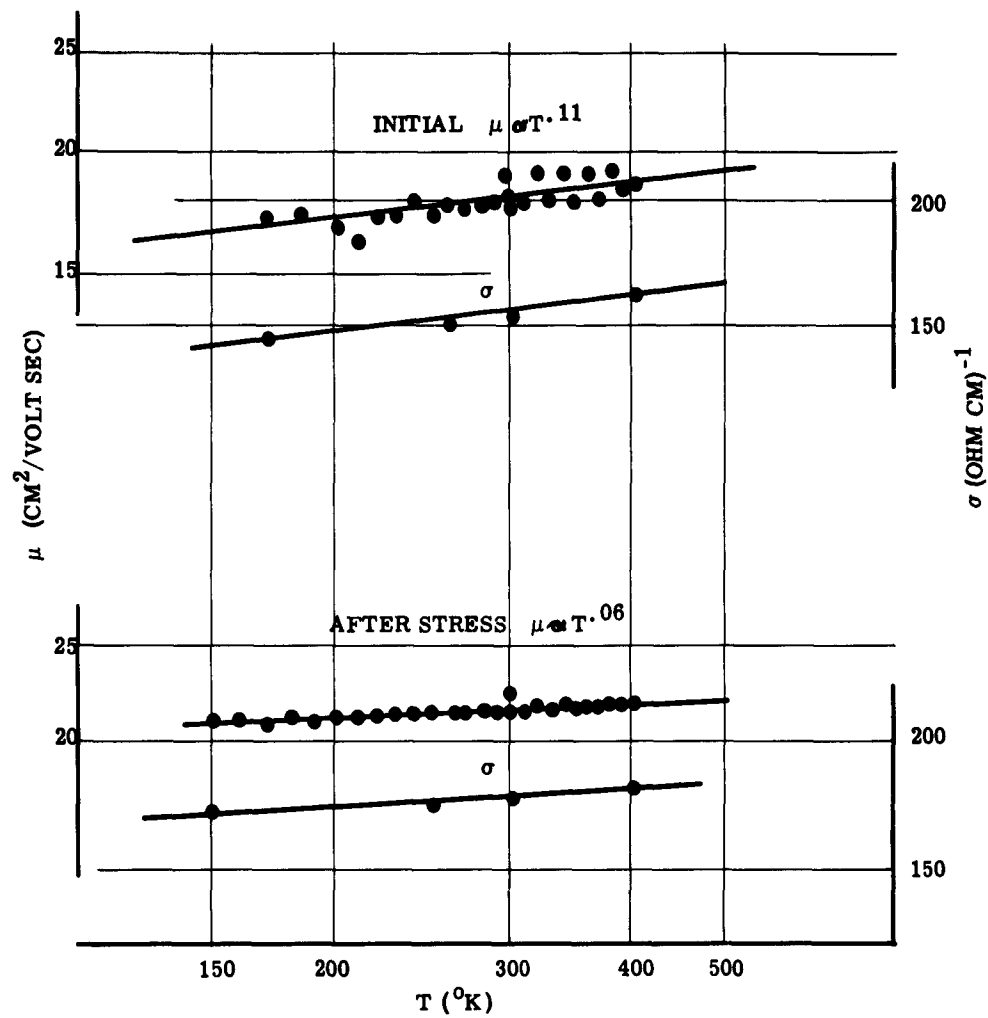


Figure 42. Glazed Alumina Test Unit, Group 16, Thermal Stress

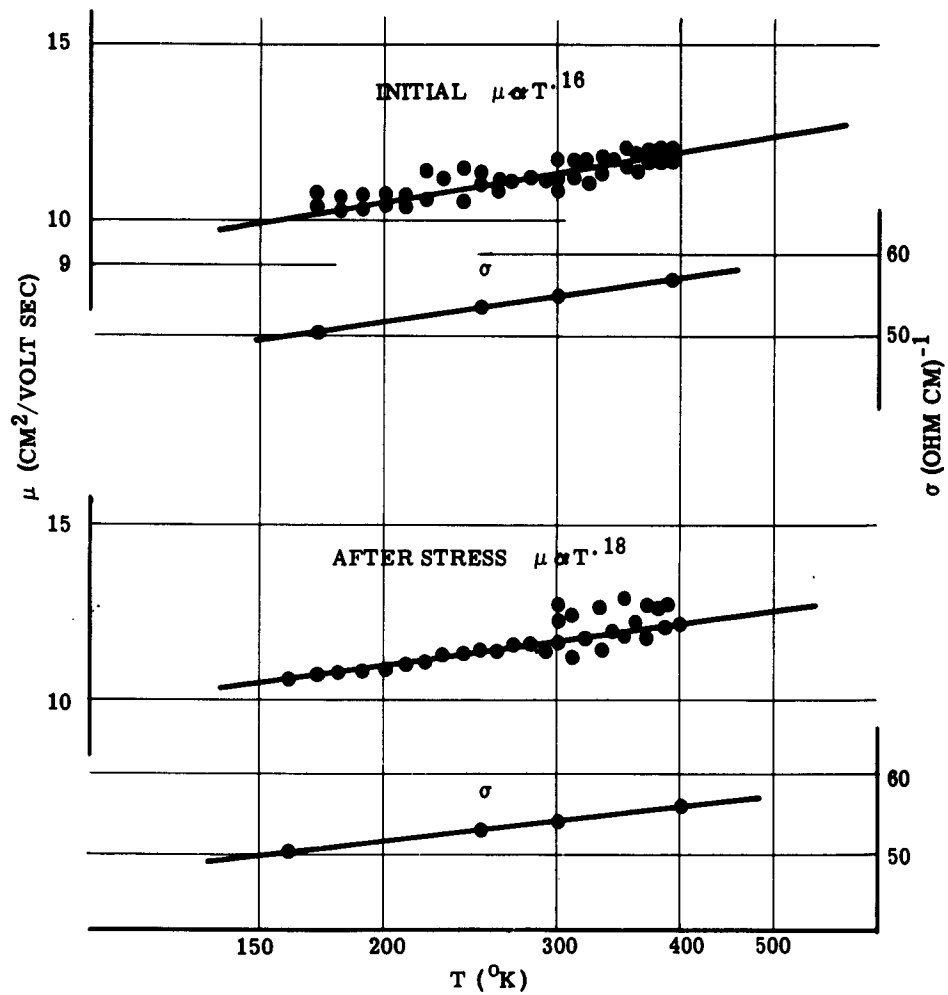


Figure 43. Unglazed Alumina, Group 15, Thermal Stress

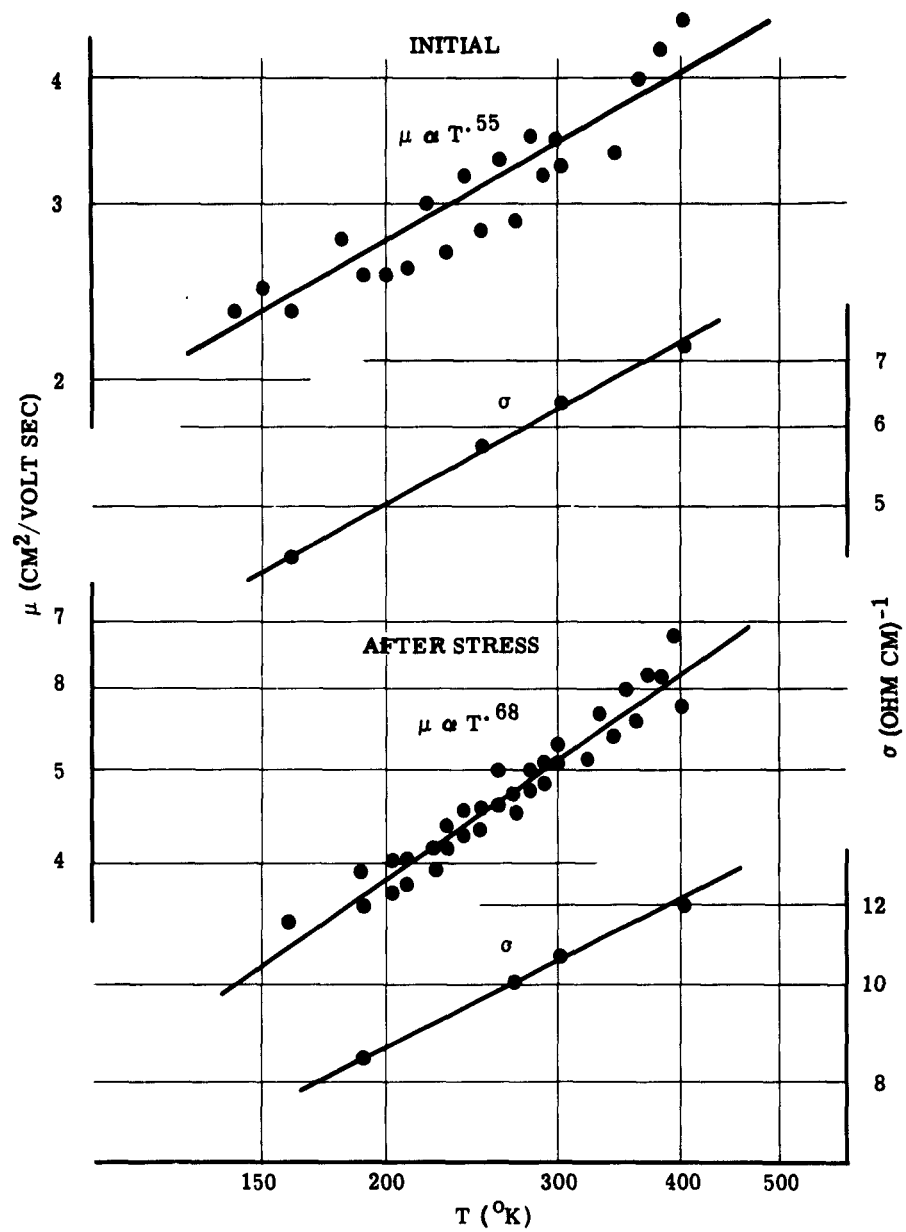


Figure 44. Microscope Slide Test Unit, Group 16, Thermal Stress

The plot of conductivity versus temperature in Figures 31 through 44 are calculated from the value of N given in Tables XI and XII and the mobility value taken off the straight line log-log plot. It is not surprising that the conductivity exhibits the same temperature dependency as the mobility since the charge carrier concentration is constant with temperature. However, the stressed microscope slide test unit, Group 15, exhibits unusual behavior and will be discussed in Paragraph 4.4.2.3

Even though all the test units were deposited under identical experimental conditions, the initial conductivities of test units of Group 15, when compared with the corresponding test units of Group 16, show a 42 to 55-per cent decrease in value for all units except the Corning 7059 glass and the microscope slide units. The decrease in conductivity of the former units can be accounted for almost completely by a comparable decrease in the charge carrier concentration. The 35-per cent difference in conductivities noted for the microscope slide test unit is due in large part to a difference in mobilities. The data for the Group 16 microscope slide test unit is too scattered for comparison. A variation in deposition parameters affecting either the state of oxidation and/or crystallite structure could account for the differences noted.

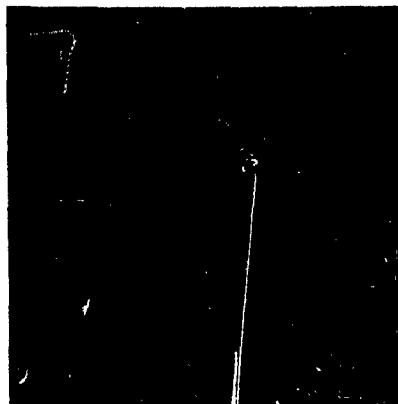
A qualitative appraisal of the data in Tables IX and X show the following general behavior. In both test groups, the relative ordering according to the substrate, of mobilities and charge carrier concentrations are similar with higher mobilities tending to be associated with higher charge carrier concentrations. In both test groups, the order of the temperature dependence of the mobility tends to be reversed from that of the mobility and charge carrier concentration. Moreover, the relative ordering of these three quantities (still with respect to the substrate) is unchanged by application of the various stress, i.e., ordering of initial values is unaffected by stress. For most test units except the sapphire, Group 15, and the unglazed alumina Group 16, the changes in conductivity with applied stress are associated with changes in mobility. The Group 15 test units exhibit decreases in conductivity with thermal-electrical stress while the Group 16 units generally increase in conductivity with thermal cycling. The 7059 Corning glass unit is the exception in this group showing a small decrease in conductivity.

4.4.2.2 Electron Microscopy

The actual polycrystalline character of the tin oxide films was elucidated by electron microscopy. Surface replicas of tin oxide films deposited on substrates of Corning 7059 glass, fused quartz, single crystal sapphire, Fotoceram, and glazed alumina were explained by Sloan Research Industries. Electron micrographs of these film surfaces are shown in Figures 45 to 47. Excerpts from the Sloan report describing these micrographs are as follows:

7059 Corning Glass: Figure 45

The micrographs illustrate that with the exception of abnormalities in the substrate surface, the tin oxide film is quite uniform and is composed of microcrystallites having an average diameter of 1000Å. Discontinuities in the film are believed to be substrate irregularities, since the deposited film covers them uniformly.

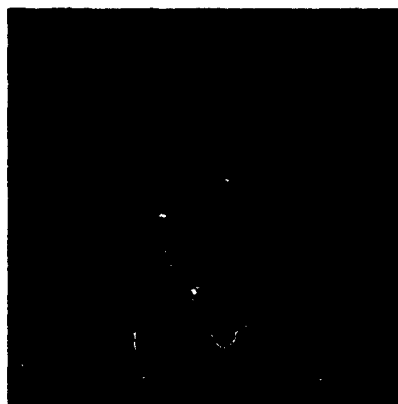


5000X



66000X

7059 Corning Glass



5000X



66500X

Fused Quartz



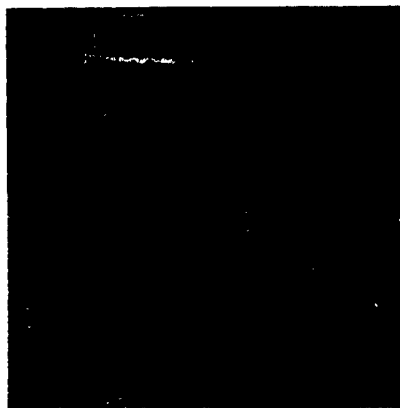
5000X



66200X

Sapphire

Figure 45. Electron Micrographs of Tin Oxide Test Units

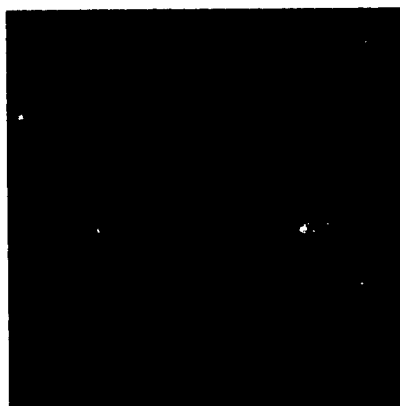


5000X



66500X

Fotoceram



4000X



58000X

Fused Quartz After 10 Thermal Cycles



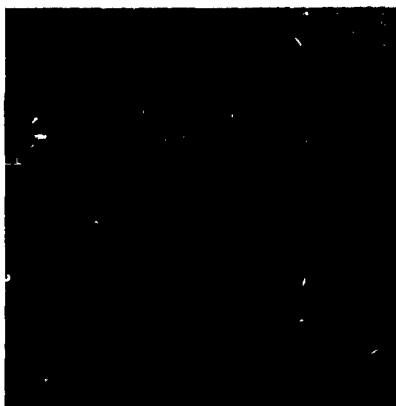
5000X



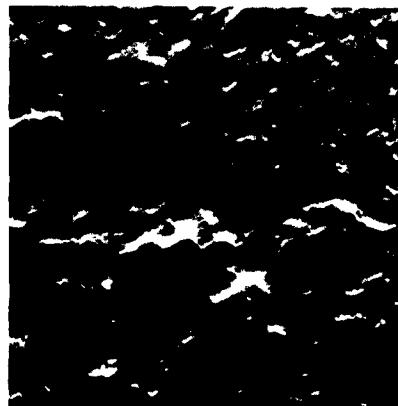
66300X

Glazed Alumina

Figure 46. Electron Micrographs of Tin Oxide Test Units

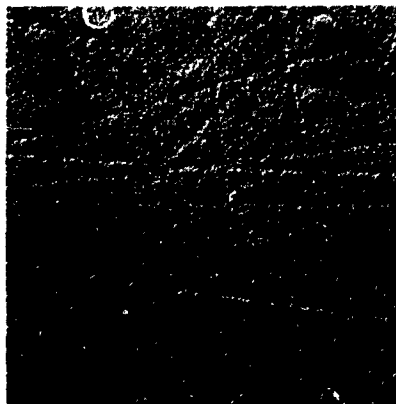


4000X



57000X

Fotoceram After Second Thermal-Electrical Stress

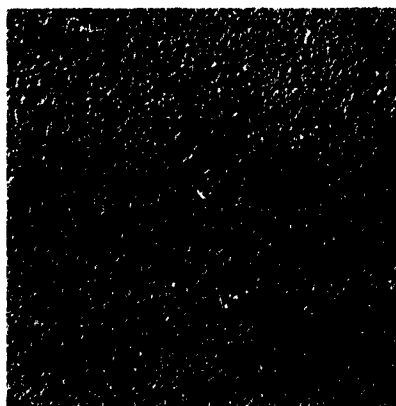


4000X

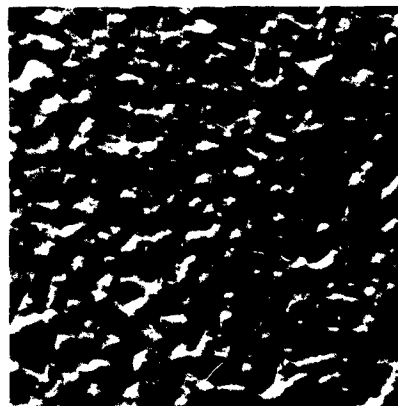


57000X

Single Crystal Sapphire After Second Thermal-Electrical Stress



4000X



57500X

Fused Quartz After 60 Thermal Cycles.

Figure 47. Electron Micrographs of Tin Oxide Test Units

Fotoceram - After Second Thermal-Electrical Stress (See Table IX): Figure 47

This sample has discontinuities that are typical of those previously observed in Fotoceram. Several large crystallites are periodically observable in the film, and seem to be concentrated in the areas of the substrate discontinuities.

Sample Preparation for Electron Microscopy

The replicas for electron microscopic viewing were prepared from the filmed surfaces of the samples in the following manner: A liquid solution of parlodian and amyl acetate was allowed to dry on the surface of the sample, and this film was stripped from the sample against a 200-mesh viewing grid. The parlodian replicas were shadowed with germanium at an angle of 45 degrees and re-replicated by the incident evaporation of carbon. The parlodian replicas were dissolved in amyl acetate and the pre-shadowed carbon replicas were viewed in a Norelco EM 100 electron microscope capable of resolving 14 angstroms.

Unfortunately, electron micrographs of all the films of interest were not obtained. It will be assumed that the film structures depicted in Figures 45 to 47 are typical of all the units prior to stressing. It is also assumed that surface replication can be used to estimate crystallite size since the crystallite boundaries are usually associated with the valleys between raised portions of the surface micrograph (the areas of light and dark contrast). It is assumed that the one surface irregularity is caused by one crystallite with its boundaries extending into the film perpendicular to the substrate. Since the film thickness is nearly the same as the average crystallite diameter, the above assumptions are probably correct.

It is surprising to note that the films deposited on a variety of substrates are composed of crystallites of the same size. The regularity of crystallite size may be due to a small constant amount of contaminate such as iron cations in the initial reactant solution. The contaminate could limit crystallite size irrespective of the nature of the substrate. Differences in the resistivity of the as-deposited films may be due to particular grain boundary effects and bulk crystallite properties, rather than crystallite size. This point will be examined in detail in Paragraph 4.4.2.2.

4.4.2.3 Interpretation of Experimental Data

It is helpful to establish a physical model of the tin oxide film to aid in the interpretation of the experimental results. The tin oxide film has been characterized by electrical and physical measurements as an "n" type, oxygen deficient polycrystalline semiconducting film. Because the film is polycrystalline, its electrical properties may be governed almost entirely by the nature of the surface layers of the individual crystallites whose electrical properties may bear little resemblance to those at the interior of the crystallite. The presence of an electrical charge on the surface creates an equal and opposite space charge just below the surface. In the case of the tin oxide film which is formed in an oxidizing ambient, a negative surface caused by absorbed oxygen charge leads to a positive space charge below the surface, resulting in a thin surface layer of higher resistivity than the interior of the crystallite. Figure 48 illustrates a situation in a polycrystalline film

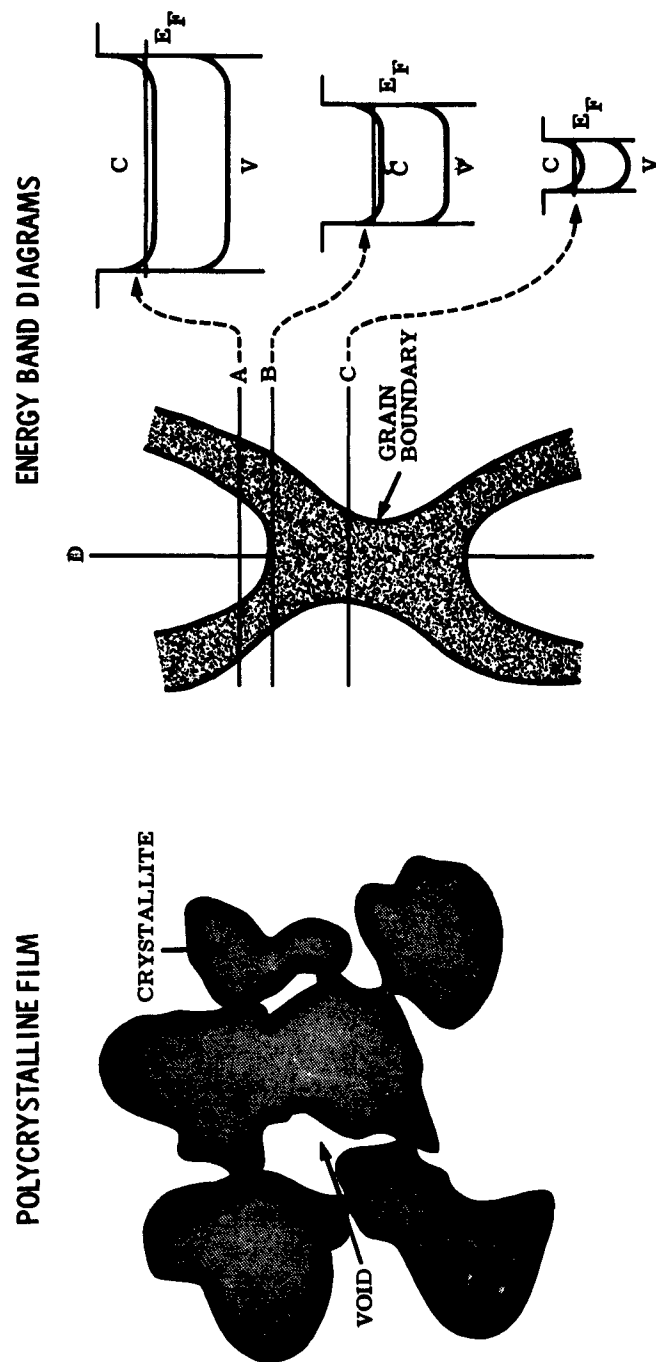


Figure 48. Schematic Structure of Polycrystalline Tin Oxide Film

where individual crystallites come together at a grain boundary⁽⁷⁾. The energy level profiles taken at different distances from the grain boundary illustrate how the space charge layers perturb the energy band levels, making the region of contact less "n" type than the interior; i. e., the electron concentration is greatly reduced in the grain boundary over its bulk value. In Figure 48, the Fermi level is shown above the conduction band, away from the grain boundary. This picture indicates that the normally degenerate crystallite may approach nondegeneracy in the region of the grain boundary. Figure 49 gives a more detailed picture of the possible band structure along a cross-section, line D, Figure 48, of the grain boundary⁽⁸⁾. Localized boundary states with discrete energy levels significantly different from those of the bulk material exist at the grain boundary. The states can act as electron traps causing a quasi-equilibrium condition to exist, in which states below the Fermi level are occupied. The resulting induced negative charge in the boundary zone, raises the potential of the conduction band, forming a potential energy barrier (V_D) with respect to the conduction electrons. The barrier does not contribute electrons to the conduction band. The position and density of barrier states and hence the value of V_D is a function of absorbed molecules, i. e., oxygen, a high density of crystal defects and impurity ion concentration at the grain boundary. In Figure 49, the Fermi level is depicted as intersecting the conduction band at X_d , to explain the observed degenerate character of the crystallites suggested by the Hall-effect measurements.

The interpretation of Hall-effect data on polycrystalline samples is complicated by the above grain boundary considerations. It is generally agreed that the values of the Hall mobility would be lower than those observed in a single crystal specimen of the same material. However, Volger⁽⁹⁾ and Miller⁽¹⁰⁾ indicate that the Hall constant obtained on samples composed of crystallites with high conductivity separated by regions of low conductivity, is a good measure of the charge carrier concentration within the crystallites, i. e., the higher Hall fields arising in the low conductivity regions (grain boundaries) are shunted out by the high conductivity crystallites. The conductivity, i. e., the product of the inverse Hall constant and the mobility, will be controlled by the low conductivity grain boundaries because of the localization of the resistance and voltage drops at these sites.

A qualitative explanation of the Hall data given in Tables VIII through XI and displaced in Figures 31 through 44 can be attempted in terms of the grain boundary model.

The samples exhibiting highest conductivities, exhibit the highest values of N and mobility. The conductivity of the film has been related to the extent of oxygen deficiency, a function of the kinetics of the oxidation process during film formation. The degree of oxidation has been shown to be less for substrates of lower thermal conductivity. (See Second Quarterly Report). Comparing substrate properties in Table VIII and initial film properties in Tables IX and X, (the relationship is evident) the highest conductivities are associated with the low thermally conducting Corning 7059 glass and fused quartz test units. The unglazed alumina and microscope slide test units exhibit anomalously low conductivities.

The electron micrographs (Figures 45, 46, 47) indicate that the average crystallite size and surface properties of the deposited films are independent of the nature of the substrate, and seemingly identical from substrate to substrate. This similarity in polycrystalline

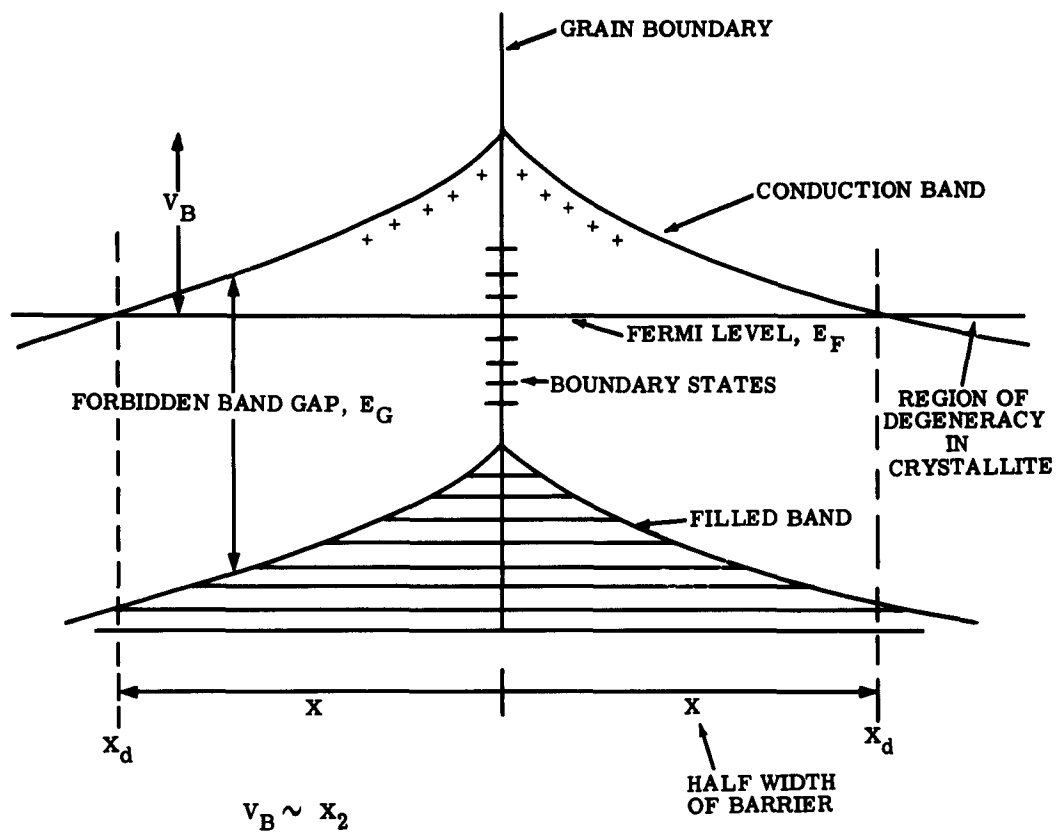


Figure 49. Energy Level Diagram at Grain Boundary

structure for films with different electrical properties indicates that the grain boundaries have a dominant role in defining the electrical properties of the film. With the exception of the microscope slide and unglazed alumina test units, it appears that the degree of degeneracy, i.e., number of charge carriers or the number of partially oxidized tin atoms, affect the nature of the grain boundary potential V_B , and the observed Hall mobility from substrate to substrate. The nature and density distribution of barrier states at the grain boundary are affected by the distribution of partially oxidized tin atoms with respect to the grain boundary and the amount of oxygen adsorbed on the outer surface of the grain boundary during film deposition. Both these effects are related to the oxidation kinetics and hence, would vary from substrate to substrate.

The strain and, hence, the defect structure built into the film on cooling from the deposition temperature ($>500^\circ\text{C}$) to room temperature should also be considered. Strains generated by contraction of the substrate would be localized at the crystallite grain boundaries, producing defect boundary states and high grain boundary potential energy barriers. From a comparison of data in Tables VIII, IX, and X, a plausible correlation between the magnitude of the thermal expansion coefficient and the conductivity is noted. The fused quartz and Corning 7059 glass substrates with the smallest expansion coefficients exhibit the largest conductivities. Strain due to film-substrate expansion mismatch is more difficult to evaluate.

The anomalously low conductivity of the microscope slide test unit is probably due to a large impurity concentration of Group I and II cations from the substrate in the grain boundary barrier region, altering the charge density and value of V_B at the barrier. The rough, unpolished surface of the unglazed alumina undoubtedly alters the polycrystalline character of the film, creating a high density of grain boundaries and defect barriers, lower effective film thickness and consequently, low conductivity. Electron micrographs of this test unit were not obtained.

The temperature dependency of the mobility for a particular test unit may also be indicative of the relative heights of the grain boundary barrier V_B from substrate to substrate. Grain boundary scattering mechanisms would be expected to show a positive temperature dependency if the mechanism depended on the ease in which a charge carrier could pass over a potential energy barrier. This situation is analogous to the positive temperature dependency of coulomb scattering by ionized impurities. Such a mechanism would also be expected at grain boundaries which act as collection sites for ionized impurities. The strong temperature dependency observed for the film on the microscope slide substrate illustrates the point. One other interesting correlation can be made between the temperature dependency of the mobilities and substrate properties. That is, the ordering of the magnitude of the temperature dependency of the mobility from substrate to substrate is nearly identical to the corresponding order of thermal expansion coefficients. Whether this indicates a change in grain boundary potential because of relative displacement of crystallites with substrate expansion or is merely a reflection of the grain boundary strain-induced defect structure previously mentioned, is unknown. It has been observed, however, that the conductivity of tin oxide films increases when the films are put under tensile stress.

A similar situation may be occurring when the test units are heated; i.e., the films, if tightly adhering to the substrate surface, may be put under tensile stress as the substrate expands. In this case, the tensile stress would increase with an increase in expansion coefficient of the substrate, and the observed ordering between the temperature dependency of the mobility and the substrate expansion coefficient would follow. Again, strains due to film-substrate expansion mismatch would also need to be considered.

In general, thermal stressing by cycling from room temperature to 200 C in a nitrogen atmosphere brings about an increase in conductivity for all units except the Corning 7059 glass, and unglazed alumina test units (see Table X). These units exhibit small decreases in conductivity. The increase in conductivity is reflected by a similar increase in mobilities. Similarly, the temperature dependency of the mobility tends to diminish with stressing. Examination of the two electron micrographs, (Figure 46, 47) of fused quartz units which exhibited an increase in conductivity with thermal stress shows little correlation between structural changes and increases in conductivity. In both cases, voids appear in the film structure and a range of crystallite sizes is observed. Neither observation was made on an initially deposited film, (Figure 45). Both effects suggest that strain release and agglomeration phenomena occur with thermal stress. The relatively small change noted after stress for the Corning 7059 test units may be attributed to a good match between expansion properties of the film and substrate. The relatively rough surface finish of the unglazed alumina test unit apparently "fixes" the as-deposited film structure in a state of disorder which is relatively insensitive to subsequent thermal stress. The large increase in conductivity observed after stress in the microscope slide test unit is not easily explained since both N and the mobility show significant increases. The increase in the positive temperature dependence of the mobility after stress may indicate that the effect of ionized impurities on the conduction mechanism becomes more pronounced. The lack of knowledge about the effects of stress on the structure of this film prevents making an assessment of the extent of impurity dominance in the conduction mechanism.

Decreases in conductivity observed in test units under thermal-electrical stress (Table IX) are reflected in similar decreases in mobilities for all test units measured with the exception of the sapphire microscope slide test units. The sapphire unit exhibits an anomalous behavior showing an increase in N after the first stress period followed by a decrease in N after the second stress period. The electron micrograph of the stressed sapphire test unit, Figure 47, does not exhibit any pronounced structural changes which correlate directly with an increase in N , although the crystalline structure is not as well defined.

The scratches in the substrate are too coarse with respect to crystallite size to perturb the conduction mechanism. The origin of the surface burnishing is unknown. The sapphire test unit is the only unit whose change in properties are dominated by a change in intrinsic properties of the crystallite as reflected by changes in N , i.e., the Hall constant which is not a function of grain boundary effects. The Fotoceram test unit shows an increasing temperature dependency of the mobility with stress. This suggests that

impurities from the substrate are accumulating in the grain boundaries with continued stress. Electron micrographs of this test unit indicate that the crystalline structure is not as well defined as in unstressed films. The stability of the Corning 7059 glass test unit is typical of this compatible substrate material. The small changes noted in the temperature dependency of the mobility for the stressed fused quartz, unglazed alumina, and sapphire test units suggests that the thermal-electrical stress affects grain boundary properties in a different manner than thermal cycling. Compositional changes such as oxidation or impurity diffusion at the grain boundaries could be induced by localized Joule heating in the high resistivity grain boundaries, with the largest changes noted for the films of lowest conductivity.

The temperature coefficient of conductivity for the microscope slide test unit before stress is roughly defined by the temperature dependency of the mobility. However, after stress, the temperature coefficient of conductivity is a function of both N and mobility, both of which exhibit a pronounced temperature dependency. The curve of N versus $1/T$ exhibits an increase in charge carrier concentration at lower temperatures, and a leveling off above 200 K (Figure 37B). An apparent activation energy of 0.12 eV is calculated for the linear portion of the curve. This activation energy may correspond to an impurity ionization energy. The $1/T$ dependence of the mobility is unusual in that the mobility decreases with an increase of temperature in the lower temperature range. The strong positive temperature dependency above 200 K may be attributed to ionizing impurity scattering. The process giving rise to an increase in the value of N must also affect the low temperature dependency of the mobility. If the impurity atoms are localized in the grain boundaries, then as a consequence of the ionization process, the grain boundary potential energy barrier would be increased, possibly limiting the mobility in the manner observed.

The effect of surface scattering-mean-free-path considerations on the conduction mechanism is negligible since the mean free path calculated from the effective Hall mobility is only one per cent or less of the total film thickness. However, the concept of mean free path has little meaning in these films since the mobility is not a true measure of intrinsic crystallite properties, but appears to be grain boundary limited.

Thickness measurements taken on the films indicate that the values fall between 1200 to 1500 angstroms and that there is no correlation of electrical characteristics with thickness over this small range.

4.5 CONCLUSIONS

The results of the Hall-effect measurements on the various tin oxide test units can be qualitatively interpreted in terms of a grain boundary potential energy barrier model. The effective mobility and its temperature dependency serve as an indicator of the role of the grain boundary in the conduction mechanism; the measured Hall constant is related to bulk crystallite properties. There have been attempts to explain the electrical behavior of polycrystalline semiconducting materials in terms of impurity band conduction schemes. This approach suggests that increases in conductivity with temperature can be related to electron transitions from an impurity band to the conduction band, with no apparent change in the value of N . However, the electronically degenerate nature and the high degree of polycrystallinity of the tin oxide films renders an analytical treatment intractable.

4.6 OTHER EFFORT

The origin of current noise in the tin oxide test unit was investigated during the last quarter, using a variety of evaporated metal and metal alloy contacts. Lead bonding schemes including soldering, ultrasonic, and thermal compression bonded leads were also investigated. The noise measurements on these systems did not contribute any information which could be correlated with the different noise levels observed in tin oxide films on different substrates.

In addition, several changes were made in the deposition process, i.e., enriched oxygen environments, higher substrate temperatures, in an attempt to deposit higher resistivity, less degenerate films. Various Group III and VI dopants were also added in an attempt to alter the electrical properties of the film. No significant improvement in Hall-effect properties over those previously observed for the original tin oxide films were realized. Hence, these new films offered no advantage in the failure mechanisms analysis.

LIST OF REFERENCES

- ¹Rose, A., Phys. Rev. 97 1538 (1955)
- ²Lampert, M.A. Phys. Rev. 103 1648 (1956)
- ³Mark, P., J. Applied Phys. 33 2988 (1962)
- ⁴Smith, R.W., Rose, A., Phys. Rev. 97 1531 (1955)
- ⁵Young, L., "Anodic Oxide Films," Chapter 7, Academic Press, New York, 1961
- ⁶Vermilyea, D.A., J. Electrochem Soc., 102, 207 (1955)
- ⁷Hannay, N.B., "Semiconductors," Chap. 13, Reinhold Publishing Corp., New York, 1959
- ⁸Gray, T.J., "The Defect Solid State," Section VII, Interscience Publishers, Inc., New York, 1957
- ⁹Volger, J., Phys. Rev., 79, page 1023 (1950)
- ¹⁰Miller, P.H., "Semiconducting Materials" page 173, H.K. Henisch, Ed., Butterworths, London 1951

DISTRIBUTION LIST

	Nr.of Copies
**RADC (RAS6P) Griffiss AFB ATTN: D.J. Nicholson New York	10
*RADC (RAAPT) Griffiss AFB New York	1
*RADC (RAALD) Griffiss AFB New York	1
*GEEIA (ROZMCAT) Griffiss AFB New York	1
*RADC (RAIS) Griffiss AFB ATTN: Mr. Malloy New York	1
*US Army Electronics R&D Labs Liaison Officer RADC Griffiss AFB New York	1
*AUL (3T) Maxwell AFB, Alabama	1
ASD (ASAPRD) Wright-Patterson AFB, Ohio	1
Chief, Naval Research Lab ATTN: Code 2027 Washington 25, D. C.	1
Air Force Field Representative Naval Research Lab ATTN: Code 1010 Washington 25, D. C.	1
Commanding Officer US Army Electronics R&D Labs ATTN: SELRA/SL-ADT Ft. Monmouth, N. F.	1
National Aeronautics & Space Adm in. Langley Research Center Langely Station Hampton, Virginia ATTN: Librarian	1
RTD (RTH) Bolling AFB Washington 25, D. C.	1
Central Intelligence Agency ATTN: OCR Mail Room 2430 E Street NW Washington 25, D. C.	1

****Project Engineer will enter his office symbol and name in space provided.**
*Mandatory

DISTRIBUTION LIST (continued)

	Nr. of Copies
US Strike Command ATTN: STRJ5-OR Mac Dill AFB, Florida	1
AFSC (SCSE) Andrews AFB Washington 25, D. C.	1
Commanding General US Army Electronics Proving Ground ATTN: Technical Documents Library Ft. Huachuca, Arizona	1
*DDC Arlington Hall Station Arlington 12, Virginia	(If not releasable to DDC, IAW AFR 205-43, send the 10 copies to RADC (RAAPP-2) for secondary distribution) Minimum of 10 copies
AFSC (SCFRE) Andrews AFB Washington 25, D. C.	1
Hq. USAF (AFCOA) Washington 25, D. C.	1
AFOSR (SRAS/Dr. G. R. Eber) Holloman AFB, New Mexico	1
Office of Chief of Naval Operations (Op-724) Navy Dept. Washington 25, D. C.	1
Commander US Naval Air Dev. Cen. (NADC Lib) Johnsville, Pa.	1
Commander Naval Missile Center Tech. Library (Code No. 3022) Pt. Mugu, California	1
Bureau of Naval Weapons Main Navy Bldg. Washington 25, D. C. ATTN: Technical Librarian, DLI-3	1
NAFEC Library Bldg. 3 Atlantic City, New Jersey	1
Redstone Scientific Information Center US Army Missile Command Redstone Arsenal, Alabama	1
Commandant Armed Forces Staff College (Library) Norfolk 11, Va.	1
ADC (ADOAC-DL) Ent. AFB, Colorado	1
AFFTC (FTOOT) Edwards AFB, California	1
Commander US Naval Ordnance Lab (Tech. Lib.) White Oak, Silver Springs, Md.	1

DISTRIBUTION LIST (continued)

	Nr. of Copies
Commanding General White Sands Missile Range New Mexico ATTN: Technical Library	1
Director US Army Engineer R&D Labs Technical Documents Center Ft. Belvoir, Va.	1
ESD (ESRL) L. G. Hanscom Field Bedford, Massachusetts	1
Commanding Officer & Director US Navy Electronics Lab (LIB) San Diego 52, California	1
ESD (ESAT) L. G. Hanscom Field Bedford, Mass.	1
Commandant US Army War College (Library) Carlisle Barracks, Pa.	1
APGC (PGAPI) Eglin AFB, Florida	1
AFSWC (SWOI) Kirtland AFB, New Mexico	1
AFMTC (Tech Library MU-135)	1
Patrick AFB, Florida	
Texas Instruments Inc. P. O. Box 5012 Dallas 22, Texas ATTN: Semiconductor Components Library	1 (Per Letter Request)
ESD (ESGT) L. G. Hanscom Field Bedford, Massachusetts	2
ESD (ESRDE, Major James W. Van Horn) L. G. Hanscom Field Bedford, Massachusetts	1
ASD (ASRCTE, Mr. E. Miller) Wright-Patterson AFB, Ohio	1
Commanding General US Army Electronic Proving Ground ATTN: Technical Documents Library Fort Huachuca, Arizona	1
Westinghouse Electric Corporation Air Arm Division (Dr. John Dzimianski) Friendship International Airport P. O. Box 1897 Baltimore 3, Maryland	2
Hughes Aircraft Company Ground Systems Division ATTN: Mr. F. M. LaFleur Fullerton, California	2

DISTRIBUTION LIST (continued)

	Nr. of Copies
Cleveland Clevite Corporation Electronic Research Division ATTN: Mr. Robert Gerson Cleveland, Ohio	2
Armour Research Foundation of Illinois Institute of Technology Technology Center ATTN: Dr. G. T. Jacobi Chicago 16, Illinois	2
Raytheon Company Research Division ATTN: Dr. P. Nutter Waltham 54, Massachusetts	2
General Telephone and Electric Bayside Laboratories ATTN: Dr. Thomas Polanyi Bayside, New York	2
Syracuse University ATTN: Dr. Glen Glasford Syracuse, New York	2
Clevite Corporation Shockley Transistor Division ATTN: Dr. Hans Queisser Stanford Industrial Park Palo Alto, California	2
Sprague Electric Company ATTN: Dr. Preston Robinson Director, Consultant N. Adams, Massachusetts	1
Frank Brand Chief Microwave Quantum Electronics Br. SIGRA/SL-PFM Fort Monmouth, N.J.	1
Wm. Spurgeon Bendix Corp. Research Lab. Div. Southfield, Michigan	1
Autonetics Div. North American ATTN: Dr. West 9150 E. Imperial Highway Downey, California	1
John G. Landers 307 The Great Road Bedford, Massachusetts	1
International Resistance Co. ATTN: Jack Iskind Proj. Mgr. XTL Resistors 401 No. Broad Street Philadelphia, Pa.	1
Delco Radio ATTN: Mr. K. Doversberger Kokomo, Indiana	1

DISTRIBUTION LIST (continued)

	Nr. of Copies
Avco, RAD ATTN: Mr. D. Earles 201 Lowell Street Wilmington, Massachusetts	1
Commanding Officer Diamond Ordnance Fuse Laboratories ATTN: Mr. Asaf A. Benderly Washington 25, D. C.	1
Corning Glass Works Electronic Components Division ATTN: Mr. Richard O'Brien Bradford, Pennsylvania	1
Fairchild Semiconductor Corporation ATTN: Mr. Jack Gorry 545 Whisman Road Mountainview, California	1
General Electric Company Semiconductor Products Department ATTN: Mr. Conrad Zierat Electronics Park Syracuse, New York	1
Pacific Semiconductor, Inc. ATTN: Mr. R. A. Campbell Culver City, California	1
Minneapolis Honeywell ATTN: Mr. J. M. Bedrick 1400 Soldiers Field Road Boston, Massachusetts	1
ARINC ATTN: Dr. H. Jervis 1700 K Street, N. W. Washington, D. C.	1
Commanding Officer US Army Electronics R&D Laboratories ATTN: SELRA/PEE, Mr. J. Gruol Fort Monmouth, New Jersey	1
General Telephone and Electronics Laboratories ATTN: Dr. Daniel George Bayside, New York	2
USASRD (SIGRA/SL-PFS, Mr. N. Korolkoff) Evans Area, Fort Monmouth, New Jersey	2
AGED Secretariat Working Group on Low Power Devices 346 Broadway New York 13, New York	3
Texas Instruments, Inc. ATTN: Semiconductor Components Library P. O. Box 5012 Dallas 22, Texas	1
Microwave Associates, Inc. ATTN: Dr. Arthur Uhlir, Jr. Burlington, Massachusetts	1

DISTRIBUTION LIST (continued)

	Nr. of Copies
Motorola, Inc. Semiconductor Products Division ATTN: Dr. Steward S. Flaschen 5005 E. McDowell Road Phoenix, Arizona	2
General Electric Company Valley Forge Technology Center ATTN: Mr. T.G. Nicoforo P.O. Box 8555 Philadelphia 1, Pennsylvania	1
Battelle Memorial Institute ATTN: Mr. T. Shilladay Columbus, Ohio	1
Hughes Aircraft Company Semiconductor Division ATTN: Library Post Office Box 1278 Newport Beach, California	1
International Telephone and Telegraph Corporation Components Division ATTN: Mr. G.G. Perry Post Office Box 412 Clifton, New Jersey	1
NASA Hq. ATTN: Mr. Fred Redler Washington, D.C.	1
General Electric Company MSD-VFSTC ATTN: Mr. G.E. Best P.O. Box 8555 Philadelphia 1, Pennsylvania	3
Dallows Laboratory, Inc. ATTN: Mr. J.T. Cataldo 120 Kansas Street El Segundo, California	1
Sprague Electric Company ATTN: Mr. C.G. Killen North Adams, Massachusetts	1
Commanding Officer, USAERDL ATTN: SIGRA/SL-PEP, Mr. T.S. Gore, Jr. Fort Monmouth, New Jersey	1
Chief, Bureau of Ships ATTN: Mr. J.M. Kerr, Jr. Room 3327, Dept. of the Navy Code 681A2A Washington 25, D.C.	1
Melpar, Inc. ATTN: Dr. Charles Feldman 3000 Arlington Blvd. Falls Church, Virginia	1

<p>Rome Air Development Center, Griffiss AF Base, N. Y. Rpt No. RADC-TDR-43-152. STUDY OF FAILURE MECHANISMS AT SURFACES AND INTERFACES. Final Rpt, July 63, 104 p. Incl. illus., tables, 10 refs.</p> <p>Unclassified Report</p> <p>The frequency dispersion of capacitance and dissipation factor for the tantalum-tantalum oxide interface system fits a curve predicted by a mathematical model of the interface based on an exponentially varying resistivity across the interface. The slopes of the dispersion curves which exhibit an inverse relationship to dielectric thickness, and, changes in the shapes of these curves brought about by thermal and humidity stressing, can also be correlated with the interface model.</p> <p>Radioactive diffusion studies have revealed that irreversible changes in stoichiometry occur across the interface of the metal-thermally, thermal-electrically stressed, tantalum-tantalum oxide interfaces. No correlation between changes in electrical properties and the observed irreversible diffusion of tantalum across the stressed interface have been made to date.</p> <p>Selective beveling and etching techniques for revealing interfacial properties have been developed and their feasibility has been demonstrated in the evaluation of the tantalum-tantalum oxide interfaces.</p> <p>Preliminary investigations of the characteristics of leakage current vs applied voltage curves for various metal-glass dielectric interfaces indicate that the</p>	<ol style="list-style-type: none"> 1. Failure Mechanisms at Surfaces and Interfaces, Study of. 1. AFRC Project 5519, Task 551906 2. Contract AF 30(602)-2593 3. Motorola Inc. 4. Solid State Systems Div. 3103 N. 56th St. Phoenix, Arizona 5. Greenough, E. Reed, F. Johnson, N. 6. Final Rpt. No. 85F-2710
<p>Rome Air Development Center, Griffiss AF Base, N. Y. Rpt No. RADC-TDR-43-152. STUDY OF FAILURE MECHANISMS AT SURFACES AND INTERFACES. Final Rpt, July 63, 104 p. Incl. illus., tables, 10 refs.</p> <p>Unclassified Report</p> <p>The frequency dispersion of capacitance and dissipation factor for the tantalum-tantalum oxide interface system fits a curve predicted by a mathematical model of the interface based on an exponentially varying resistivity across the interface. The slopes of the dispersion curves which exhibit an inverse relationship to dielectric thickness, and, changes in the shapes of these curves brought about by thermal and humidity stressing, can also be correlated with the interface model.</p> <p>Radioactive diffusion studies have revealed that irreversible changes in stoichiometry occur across the interface of the metal-thermally, thermal-electrically stressed, tantalum-tantalum oxide interfaces. No correlation between changes in electrical properties and the observed irreversible diffusion of tantalum across the stressed interface have been made to date.</p> <p>Selective beveling and etching techniques for revealing interfacial properties have been developed and their feasibility has been demonstrated in the evaluation of the tantalum-tantalum oxide interfaces.</p> <p>Preliminary investigations of the characteristics of leakage current vs applied voltage curves for various metal-glass dielectric interfaces indicate that the</p>	<ol style="list-style-type: none"> 1. Failure Mechanisms at Surfaces and Interfaces, Study of. 1. AFRC Project 5519, Task 551906 2. Contract AF 30(602)-2593 3. Motorola Inc. 4. Solid State Systems Div. 3103 N. 56th St. Phoenix, Arizona 5. Greenough, E. Reed, F. Johnson, N. 6. Final Rpt. No. 85F-2710
<p>Rome Air Development Center, Griffiss AF Base, N. Y. Rpt No. RADC-TDR-43-152. STUDY OF FAILURE MECHANISMS AT SURFACES AND INTERFACES. Final Rpt, July 63, 104 p. Incl. illus., tables, 10 refs.</p> <p>Unclassified Report</p> <p>The frequency dispersion of capacitance and dissipation factor for the tantalum-tantalum oxide interface system fits a curve predicted by a mathematical model of the interface based on an exponentially varying resistivity across the interface. The slopes of the dispersion curves which exhibit an inverse relationship to dielectric thickness, and, changes in the shapes of these curves brought about by thermal and humidity stressing, can also be correlated with the interface model.</p> <p>Radioactive diffusion studies have revealed that irreversible changes in stoichiometry occur across the interface of the metal-thermally, thermal-electrically stressed, tantalum-tantalum oxide interfaces. No correlation between changes in electrical properties and the observed irreversible diffusion of tantalum across the stressed interface have been made to date.</p> <p>Selective beveling and etching techniques for revealing interfacial properties have been developed and their feasibility has been demonstrated in the evaluation of the tantalum-tantalum oxide interfaces.</p> <p>Preliminary investigations of the characteristics of leakage current vs applied voltage curves for various metal-glass dielectric interfaces indicate that the</p>	<ol style="list-style-type: none"> 1. Failure Mechanisms at Surfaces and Interfaces, Study of. 1. AFRC Project 5519, Task 551906 2. Contract AF 30(602)-2593 3. Motorola Inc. 4. Solid State Systems Div. 3103 N. 56th St. Phoenix, Arizona 5. Greenough, E. Reed, F. Johnson, N. 6. Final Rpt. No. 85F-2710
<p>Rome Air Development Center, Griffiss AF Base, N. Y. Rpt No. RADC-TDR-43-152. STUDY OF FAILURE MECHANISMS AT SURFACES AND INTERFACES. Final Rpt, July 63, 104 p. Incl. illus., tables, 10 refs.</p> <p>Unclassified Report</p> <p>The frequency dispersion of capacitance and dissipation factor for the tantalum-tantalum oxide interface system fits a curve predicted by a mathematical model of the interface based on an exponentially varying resistivity across the interface. The slopes of the dispersion curves which exhibit an inverse relationship to dielectric thickness, and, changes in the shapes of these curves brought about by thermal and humidity stressing, can also be correlated with the interface model.</p> <p>Radioactive diffusion studies have revealed that irreversible changes in stoichiometry occur across the interface of the metal-thermally, thermal-electrically stressed, tantalum-tantalum oxide interfaces. No correlation between changes in electrical properties and the observed irreversible diffusion of tantalum across the stressed interface have been made to date.</p> <p>Selective beveling and etching techniques for revealing interfacial properties have been developed and their feasibility has been demonstrated in the evaluation of the tantalum-tantalum oxide interfaces.</p> <p>Preliminary investigations of the characteristics of leakage current vs applied voltage curves for various metal-glass dielectric interfaces indicate that the</p>	<ol style="list-style-type: none"> 1. Failure Mechanisms at Surfaces and Interfaces, Study of. 1. AFRC Project 5519, Task 551906 2. Contract AF 30(602)-2593 3. Motorola Inc. 4. Solid State Systems Div. 3103 N. 56th St. Phoenix, Arizona 5. Greenough, E. Reed, F. Johnson, N. 6. Final Rpt. No. 85F-2710

<p>observed trap-lin tied, space-charge limited currents are a function of the nature of the metal electrode interface and applied thermal stress.</p> <p>Results of the investigations on the various semiconducting tin oxide film-substrate interface systems have shown that changes in the basic conduction mechanism as a function of applied thermal and electrical stress are revealed by measurement of changes in the Hall mobility and its temperature dependence, and the Hall constant. Stressed-induced changes in the conduction mechanism of the electronically degenerate film are qualitatively described in terms of high resistivity crystallite grain boundary regions of the polycrystalline film, and in terms of the physical and chemical properties of the substrate.</p>	<p>Failure Mechanisms at Surfaces and Interfaces, Study of.</p> <p>I. AFSC Project 5519, Task 551906</p> <p>II. Contract AF 30(602)-2585</p> <p>III. Motorola Inc.</p> <p>Solid State Systems Div.</p> <p>3102 N. 56th St.</p> <p>Phoenix, Arizona</p> <p>IV. Greenough, K. Reed, F. Johnson, N.</p> <p>V. Final Rpt. No. SSF-2710</p>	<p>observed trap-limited, space-charge limited currents are a function of the nature of the metal electrode interface and applied thermal stress.</p> <p>Results of the investigations on the various semiconducting tin oxide film-substrate interface systems have shown that changes in the basic conduction mechanism as a function of applied thermal and electrical stress are revealed by measurement of changes in the Hall mobility and its temperature dependence, and the Hall constant. Stressed-induced changes in the conduction mechanism of the electronically degenerate film are qualitatively described in terms of high resistivity crystallite grain boundary regions of the polycrystalline film, and in terms of the physical and chemical properties of the substrate.</p>	<p>I. AFSC Project 5519, Task 551906</p> <p>II. Contract AF 30(602)-2585</p> <p>III. Motorola Inc.</p> <p>Solid State Systems Div.</p> <p>3102 N. 56th St.</p> <p>Phoenix, Arizona</p> <p>IV. Greenough, K. Reed, F. Johnson, N.</p> <p>V. Final Rpt. No. SSF-2710</p>
<p>observed trap-lin tied, space-charge limited currents are a function of the nature of the metal electrode interface and applied thermal stress.</p> <p>Results of the investigations on the various semiconducting tin oxide film-substrate interface systems have shown that changes in the basic conduction mechanism as a function of applied thermal and electrical stress are revealed by measurement of changes in the Hall mobility and its temperature dependence, and the Hall constant. Stressed-induced changes in the conduction mechanism of the electronically degenerate film are qualitatively described in terms of high resistivity crystallite grain boundary regions of the polycrystalline film, and in terms of the physical and chemical properties of the substrate.</p>	<p>Failure Mechanisms at Surfaces and Interfaces, Study of.</p> <p>I. AFSC Project 5519, Task 551906</p> <p>II. Contract AF 30(602)-2585</p> <p>III. Motorola Inc.</p> <p>Solid State Systems Div.</p> <p>3102 N. 56th St.</p> <p>Phoenix, Arizona</p> <p>IV. Greenough, K. Reed, F. Johnson, N.</p> <p>V. Final Rpt. No. SSF-2710</p>	<p>observed trap-limited, space-charge limited currents are a function of the nature of the metal electrode interface and applied thermal stress.</p> <p>Results of the investigations on the various semiconducting tin oxide film-substrate interface systems have shown that changes in the basic conduction mechanism as a function of applied thermal and electrical stress are revealed by measurement of changes in the Hall mobility and its temperature dependence, and the Hall constant. Stressed-induced changes in the conduction mechanism of the electronically degenerate film are qualitatively described in terms of high resistivity crystallite grain boundary regions of the polycrystalline film, and in terms of the physical and chemical properties of the substrate.</p>	<p>I. AFSC Project 5519, Task 551906</p> <p>II. Contract AF 30(602)-2585</p> <p>III. Motorola Inc.</p> <p>Solid State Systems Div.</p> <p>3102 N. 56th St.</p> <p>Phoenix, Arizona</p> <p>IV. Greenough, K. Reed, F. Johnson, N.</p> <p>V. Final Rpt. No. SSF-2710</p>